Supplementary Information

In-Situ Nanoscale Heterostructure Engineering for Additive Manufacturing of Dynamic Adaptive Alloys

Junchao Yi [1], *Gary J. Cheng* [1,2*]

[1] The Institute of Technological Sciences, Wuhan University, Wuhan 430072, PR China
[2] School of Industrial Engineering, Purdue University, West Lafayette, IN 47906, United States
*Corresponding author: G.J. Cheng (gjcheng@purdue.edu).

The PDF file includes:

Materials and Methods
Supplementary Notes
Figs. S1 to S47
Tables S1 to S10
Supplementary References

Other Supplementary Information for this manuscript include the following:

Movies S1 to S6

Materials and Methods

1. Materials

The pre-alloyed $Ni_{50.8}Ti_{49.2}$ (in atomic %) shape memory alloy (SMA) micropowder used in this work was provided by Avimetal Inc. and produced by electrode induction melting gas atomization (EIGA) technology, with the particle size distribution range of 15−55 μm and a D_{50} of 35 μm (Fig. S31). The chemical composition of the as-received (AR) SMA powder was determined with inductively coupled plasma-optical emission spectrometry (ICP-OES) carried out on an Agilent 5110, and its flowability was measured through a Hall flowmeter, as specified in Tables S4 and S5. High purity (99.9%) boron carbide nanoparticles (nano-B_4C) with the average size of 35 nm were purchased from MACKLIN and used as the additive (Fig. S31). Isopropanol reagent (IPA, > 98%) was purchased from Sigma-Aldrich. All chemicals were directly used as received without further purification.

2. Powder preparation

The nano-B_4C functionalized SMA powder for laser nanometallurgy-assisted alloy design was fabricated by a hydrostatic adsorption method and low-energy ball-milling. In a typical powder preparation procedure, the nano-B_4C was dispersed in IPA by sonication bath to make an in-situ nanoreactant suspension with a specific volume. Then, it was added to the SMA micropowder for infiltration in 10 min increments for a total of 60 min under continuous mechanical stirring. IPA acts as an efficient volatile solvent, which enables hydrostatic adsorption from capillarity of the liquid film present between the nanoparticles and the micropowder surface. These in-situ nanoreactant dispersoids were further coated onto the SMA matrix powder by low-energy ball-milling. Last, the obtained powder was sieved using a 260 mesh (pore size, 55 μm) screen to remove any large agglomerates or metallic powder particles. A detailed description of controlling the in-situ nanoreactant loading can be found in the Supplementary Note 1. Scanning electron microscopy (SEM) images and elemental SEM-energy-dispersive x-ray spectroscopy (SEM-EDX) maps show the highly spherical morphology of as-prepared in-situ nanometallurgical SMA (INSMA hereafter) powder with strongly adsorbed in-situ nanoreactants well-dispersed on the surface (Fig. S32). All powders were dried in a vacuum oven at 343 K for 10 h to dehydrate before their use in laser trials.

3. Laser powder bed fusion additive manufacturing (LPBF-AM) fabrication

LPBF-AM was performed using an AmPro SP100 system equipped with a 200 W IPG continuous-wave Yb-fiber laser (λ = 1064 nm, infrared) and a high-quality Gaussian beam (M^2 < 1.1). The laser-matter interaction process was completed under a flowing high-purity (≥ 99.99%) inert argon gas atmosphere with an oxygen content below 200 ppm to minimize oxidation of the active elements. No additional heat was applied to the customized SMA build plate throughout the LPBF-AM process. The laser printing parameters used in our work include a laser power of 170 W, a scanning speed of 170 $mm \cdot s^{-1}$, a hatching space of 90 μm, a layer thickness of 30 μm, a laser spot diameter of 60 μm, a laser energy density of 370.4 $J \cdot mm^{-3}$, a rotation angle between consecutive layers maintained at 67°, and an island scanning strategy. A detailed description of

optimizing the laser printing parameters can be found in the Supplementary Note 2. In the present study, the cubic samples, tensile dog-bone samples, millimeter-scaled pillar (milli-pillar) compression samples, and four lattice structure types of mechanical metamaterial samples were directly printed for microstructure characterization and mechanical testing. The macroscopic images and geometric dimensions of the as-printed parts are schematically demonstrated in Fig. S36. Meanwhile, pure SMA without nanoreactant addition was fabricated for a comprehensive comparison with the designed INSMA.

4. Microstructure characterization

SEM images were collected from a TESCAN MIRA 3 SEM equipped with a Schottky thermal-field emission gun (FEG) operated at 20 kV, with built-in EDAX Octane Elite EDX and eFlash FS electron backscatter diffraction (EBSD) detectors. A step size of 0.2 μm was used for the EBSD scan, and the acquired data points with low confidence indices (CI) were precleared using Oxford AZtecCrystal software before establishing the grain structure figures. The EBSD samples were prepared in a Fischione Model 1061 SEM Mill by dual argon ion gun milling at 6 kV and 5.8 mA for 1 h. The X-ray diffraction (XRD) patterns were collected via a Rigaku SmartLab SE X-ray diffractometer under Bragg-Brentano mode using Cu Kα (λ = 1.54178 Å) radiation source, operated at 40 kV and 50 mA. Data were collected between 20° and 100° in 2θ using the SmartLab Studio II software package. Information on spatial structures within LPBF-AM printed shape-memory mechanical metamaterials was examined by high-resolution 3D X-ray transmission (XRT) technique using a Zeiss Xradia Context microfocus computed tomography (micro-CT) system. Beam power during micro-CT scanning was 10 W and the acceleration voltage was 130 kV. A total of 1,501 projections were recorded when the sample was rotated through 360°, with an exposure time of 1.2 s for each projection and an approximate voxel size of 8.1 μm. Acquired 2D projection data were reconstructed and visualized using Dragonfly Pro workstation. Transmission electron microscopy (TEM) images, selected area electron diffraction (SAED) patterns, and elemental TEM-EDX maps under scanning TEM (STEM) mode were analyzed by using a JEOL JEM-F200 TEM equipped with a high-angle annular dark-field (HAADF) detector and a Super-X Quad windowless EDX system based on silicon drift technology, operated at 200 kV. The STEM-HAADF images were obtained with the probe size was set to 0.1 nm, a convergence semi-angle of 22.5 mrad, and collection semi-angles of 80−150 mrad. The atomic resolution analytical STEM images were captured from JEOL JEM-ARM300F2 GRAND ARM™2 double Cs-corrected TEM equipped with a Schottky cold-FEG and a DCOR probe Cs-corrector (CEOS GmbH) operated at 300 kV. The raw spectrum image data were denoised by applying a principal component analysis (PCA) with a built-in multivariate statistical analysis (MSA) plugin in Gatan Digital Micrograph.

5. Transmission Kikuchi diffraction (TKD)

By using an electron-transparent and nanometre-thick thin-foil instead of a bulk sample, the lateral resolution of TKD can be improved to less than 10 nm, making this technique particularly suitable for the study of the phase distribution and crystallography of complex nano-scale

materials.[S1] High-precision, on-axis TKD characterization was carried out on a Bruker OPTIMUS™ TKD detector operated at an acceleration voltage of 30 kV and a probe current of 1.5 nA. The TKD lamella was mounted with the TKD head positioned immediately beneath the sample. Kikuchi patterns were acquired with 233 × 233 pixels using a scan step of 3 nm and exposure time of 6 ms per point to generate high-spatial resolution results on phases and their orientations of the dual-nanoprecipitates. All the TKD maps were further cleaned to remove isolated pixels that were incorrectly indexed or not solved. The crystallographic information used in identifying the phase distribution in the samples is summarized in Table S6.

6. Focused ion beam (FIB) site-specific sampling

The TEM and TKD lamellas from longitudinal sections (along the build direction) were prepared by in site FIB in a TESCAN AMBER DualBeam SEM. For reducing surface damage induced by the high energy gallium ions, a protective platinum layer was deposited at 30 kV and 200 pA prior to FIB milling. Starting from 30 kV down to 5 kV, the sample was tilted 52 ± 1.1° and the gallium ions strike perpendicular to the sample surface. After lifting out the sample and welding it to a 3 mm Cu TEM grid, and fine ion polished using a low current of 30 pA multiple times as the final steps. For the obtained elementary TKD lamella sample, the angles of gallium ions striking the sample will be lowered to ± 2°, thereby achieving the uniform sample thinning with a thickness of ~50 nm. It is important to achieve samples as thin as this to obtain resolvable Kikuchi patterns from TKD analysis of nanocrystalline materials.[S2] An example of site-specific sampling for the postmortem microstructure characterization of the micropillar after compression following above procedures, as shown in Fig. S37. This sample preparation methodology enables improved geometry stability of the lamella, allows a single sample to be transported without risk of damage, and avoids bending at severe FIB milling levels.

7. Powder characteristics

The laser reflectivity of the powder samples was determined by diffuse reflectance spectroscopy (DRS) using a SHIMADZU UV-3600 UV-Visible-NIR spectrophotometer and converted to Kubelka-Munk (K-M) absorption factors. Then, the particle size distribution of the SMA powder was measured with a Malvern Panalytical Mastersizer 3000 laser granulometer.

8. Differential scanning calorimetry (DSC) measurement

DSC characterization was used to investigate the phase transformation temperatures (TTs) by Mettler-Toledo DSC3 in a temperature ranged from 193 K to 393 K with a heating/cooling rate of 10 $K \cdot min^{-1}$ under nitrogen environment per ASTM F2004-05 standard. The sample was placed in an alumina crucible covered by a lid with a pinhole to prevent pressure build-up.

9. Mechanical testing at the macroscale

The flat tensile dog-bone specimens (35 mm in gauge length and 3 × 2 mm^2 in cross-section) and milli-pillar compression specimens (4 mm in diameter and 6 mm in height) were cut using electro-discharge machining (EDM). The mechanical grinding and polishing procedures were

subsequently conducted using sandpaper and colloidal silica to get rid of surface damage. Uniaxial tensile and compression tests were performed on an MTS C43 universal test frame at a constant strain rate of 1×10^{-3} s^{-1} under room temperature. For four lattice structure types of mechanical metamaterial samples, ten loading-unloading-reloading (LUR) cyclic compression tests with a constant strain value of 0.10, as well as gradient strain compression tests with strain values set sequentially at 0.02, 0.04, 0.06, 0.08, and 0.10, were performed to examine the superelastic response. An Epsilon axial extensometer was used to precisely measure the strain across the gauge regions during tensile tests. At least three samples were tested for each condition to ensure the reproducibility of the macro-mechanical test results. It should be emphasized that even for cyclic compression tests or gradient compression tests, the tested specimens inevitably retain residual strain after loading, which renders them effectively one-time-use and irreversible, thereby limiting the number of available samples.

10. Micropillar compression with in-situ SEM observation

The micropillars (2 μm in diameter, 4 μm in height and aspect ratio of 2:1) were fabricated by FIB at the top edge of the printed sample after ion surface polishing, so that the top and front views of the micropillar could be exposed to the SEM visual field. Taper angles of the pillars were kept to less than 5° to minimize errors in stress estimation from ideal strain-gradient free cylindrical samples. The micropillar was situated in a 30 μm-diameter circular cavity, leaving sufficient margin for the indenter tip. It should be noted that the locations of micropillars were chosen randomly within the B2 austenite grains. All micropillars were aligned to have the top surface perpendicular to the build direction. In-situ micropillar compression tests at room temperature were conducted on a Hysitron PI 85E PicoIndenter equipped with a 10 μm-diameter flat-end diamond tip inside a Zeiss Gemini 300 SEM chamber. The micropillars were compressed until failure at a nominal strain rate of 1.25×10^{-3} s^{-1} in displacement-controlled mode, and the real time load-displacement data and in-situ deformation videos of micropillars were recorded. For the microfatigue tests, 10^4 cycles of compression were conducted in load-controlled mode with a frequency of 5 Hz (Fig. S38). It should be noted that the choice of 5 Hz loading frequency follows established practice in microscale mechanical testing,[S3] and higher frequencies (e.g., 100 Hz) have also been reported.[S4] While loading frequency may affect the absolute kinetics of dislocation motion, the identical testing conditions adopted here for both pristine SMA and INSMA ensure that their relative mechanical behaviors can be reliably compared. Each displacement signal was recalibrated after 10^3 loading cycles (~180 s) to minimize the effect of mechanical drifting. The yield strengths of all samples were identified using the stress corresponding to 0.2% offset strain. At least three samples were tested for each condition to ensure the reproducibility of the micro-mechanical test results.

11. Nanoindentation measurement

High-speed nanoindentation mappings were carried out on transverse sections with a KLA iNano nanomechanical test system. Square grids of 400 (20 × 20 arrays) indents with an area of 300×300 μm^2 were created via a diamond Berkovich indenter to obtain hardness and modulus

mappings. An applied maximum load of 50 mN was selected on the basis of continuous stiffness measurement (CSM) method to maintain that the maximum indentation depth ranged from 800−1100 nm. The inter-indent spacing was set to 10 μm, resulting in a ratio close to 1:10 between depth and spacing of the indents, to provide the optimum spatial resolution, while preventing significant interaction between the plastic deformation zones of adjacent indents.[S5] Gradient load nanoindentation measurements were used to evaluate the indentation size effect with applied maximum loads sequentially of 2 mN, 4 mN, 10 mN, 20 mN, 30 mN, 40 mN, and 50 mN, a target indentation strain rate of 0.2 s^{-1}, a hold maximum load time of 1 s, and were tested ten times for each condition.

12. Tribological, 3D surface topography and contact angle testing

Tribological performance tests were conducted using a CETR UMT-2 ball-on-disc tribometer under a normal load of 20 N and a linear reciprocating frequency of 1 Hz at ambient temperature. Silicon nitride (Si_3N_4, 60 HRC) ceramic balls with a diameter of 4 mm were used as the counterparts, and the friction duration was 30 min and the stroke length was 4 mm, for each time. Finally, the worn surfaces were observed by SEM to determine the operative wear mechanisms. A KLA MicroXAM-800 optical interferometric profiler was used to examine the 3D surface topographies, cross-sectional profiles, and manufacturing accuracy. A Data-physics OCA25 goniometry instrument was used to measure the contact angle of the sample at room temperature (25 ± 2 °C) with a 4-μL distilled water droplet.

13. Damping experiments

The damping capacity (internal friction, IF) of all samples with dimensions of 30 mm × 3 mm × 1 mm were characterized by a TA Q800 dynamic mechanical analyzer (DMA) in a single cantilever mode. Specifically, the strain sweep was measured with a constant frequency of 1 Hz and a strain amplitude ranged from 0 to 900 × 10^{-6} at ambient temperature (298 K). Stress relaxation was measured at a strain level of 0.02% using the time-temperature superposition (TTS) principle. The complex modulus ($G = G' + iG''$) was further deduced from the measurements, where G' represents the storage modulus and G'' refers to the loss modulus. The loss factor $\tan \delta = G''/G'$ could then be calculated.

14. Shape memory experiments

The shape memory response was determined on a DMA in a single cantilever mode with a specimen geometry of 35 mm × 3 mm × 0.5 mm. The specimen was equilibrated within the gripper for 10 min before starting the shape memory experiment to prevent specimen from buckling after stress equilibration. The procedure for the shape memory experiment was run in the following steps. First, the specimen was held at 298 K for 10 min with a 0 N force applied. Next, the temperature was ramped down from 298 K to 203 K at a cooling rate of 10 $K \cdot min^{-1}$ and held for 10 min. At this point, a specified stress (180 MPa) or strain (1.4%) was applied to each specimen. The specimen was held at a maximum load for 30 s before the force was released with a loading/unloading rate of 0.5 N min^{-1}. After 10 min, the temperature was then ramped up to 383

K at a heating rate of 10 $K \cdot min^{-1}$ while holding an IsoForce of 0 N to allow the specimen to recover its original shape.

15. Electrochemical corrosion performance tests

Electrochemical measurements were performed using a CHI660e electrochemical workstation to evaluate the electrochemical corrosion performances. The as-built sample surfaces were mechanically abraded up to 7000-grit by SiC paper and then polished with water-based diamond suspensions. All corrosion experiments were conducted in 3.5 wt.% NaCl solution at room temperature using a sealed conventional three-electrode cell system, with the sample (exposed area: 1 cm^2) as the working electrode, a platinum sheet as the counter electrode, and a saturated calomel electrode (SCE) with a salt bridge as the reference electrode. Open circuit potential (OCP), potentiodynamic polarization, and electrochemical impedance spectroscopy (EIS) tests were carried out. Before EIS and polarization tests, the working electrode was immersed in the electrolyte for 1 h to stabilize the OCP. EIS tests were conducted at the stabilized potential over a frequency range of 10^{-2} to 10^5 Hz with an amplitude of 10 mV. The potentiodynamic polarization curves were tested from -0.4 V to -1.7 V under a scanning rate of 2 mV/s. Each electrochemical test was repeated three times on separate flat surfaces to ensure reproducibility, and the averaged curves are reported.

Supplementary Notes

1. Control of in-situ nanoreactant loading

To accurately control the in-situ nanoreactant loading in the INSMA powders, we tuned the mass ratio of the nano-B_4C particles to the SMA micropowder. According to bulk density and mechanical testing results, we found that 0.05 wt.% addition was optimal. Nanoparticles are highly susceptible to agglomeration due to attractive van der Waals forces at excessive addition levels, leading to a reduction in the strength and plasticity, such as at 0.5 wt.% (Fig. S32). Optical image presents that the SMA powder functionalized with nanoreactant particles at the macroscale exhibits a significantly deeper color (Fig. S33A). The phase identification results of the powder XRD (PXRD) patterns show that the functionalized powder is consistent with the raw powder, and both have solely B2 austenite phase (Fig. S33B). This indicates that the INSMA powder prepared in the present study can maintain a stable phase structure at both hydrostatic adsorption and mechanical ball-milling conditions. The detailed low-energy ball-milling parameters involved are as follows. The mixing process was performed at a fixed rotational speed of 150 rpm under the protection of an argon atmosphere to avoid oxidation. Specifically, stainless steel balls with a diameter of 5 mm were used as the grinding media, and the ball-to-powder ratio was 5:1. Every 30 min of milling was followed by a 10 min pause to avoid temperature rise, and the total duration is 8 h.

On the other hand, the uniformly coated nano-B_4C particles on the surface of INSMA powder can enhance laser absorption efficiency because of the low laser reflectivity of non-oxide ceramic nanoparticles. As shown in Fig. S33, C and D, the laser reflectivity of the SMA can be reduced by ~46% with 0.05 wt.% addition of nano-B_4C, whereas the K-M absorption factor was raised by ~157%. It could be attributed to the multiple reflection and absorption that is effective on the irregular surface formed.[S6] As a result, the INSMA powder per unit surface area has a higher average laser energy density, which can ameliorate the laser printing process.

2. Optimization of LPBF-AM processing parameters

Using the equivalent volumetric laser energy density method,[S7-S9] we constructed normalized processing diagram to determine an effective LPBF-AM processing window, which allows to print fully dense (relative density of ~99.97%) SMA parts (Fig. S34). By adjusting the laser power and scan speed, the relative densities of the LPBF-AM as-printed samples were measured through Archimedes' method to characterize the significant impact of the processing parameters on the densification behavior. We observed that the parameter map can be subdivided into four types of as-printed states based on the relative density and defect features (Fig. S35). A large number of pores and lack of fusion defects with an irregular shape appeared in the bottom right corn of the parameter map, i.e., high laser powers combined with high scan speed (marked with blue boxes). The parts printed at low laser powers and relatively high scan speeds or at high laser powers and low scan speeds failed to be printed due to the serious warping (marked with red boxes). Green boxes marked off a relatively wide processing window for printing high-quality samples with very low porosity and near fully dense (> 99.9%). In addition, the remaining parameter combinations were considered as unsuitable as the corresponding samples featured with intolerably high porosity

or cracks (marked with yellow boxes). On this basis, the refined LPBF-AM processing parameters were used to produce SMA parts and further understand the relationship between their microstructures and mechanical properties.

3. Conversion of Kubelka-Munk (K-M) absorption factor

For the LPBF-AM process, the laser absorption efficiency plays a crucial role in determining the energy coupling effect between the laser and the metallic powders. To analyze this phenomenon, we converted the acquired laser reflectivity spectra by diffuse reflectance spectroscopy (DRS) to K-M absorption factor curve through the following equation to evaluate the laser adsorption capacity of the powder.[S10]

$$f(R) = \frac{(1-R)^2}{2R} \tag{1}$$

Here, $f(R)$ represents the K-M absorption factor, and R refers to the measured laser reflectivity of the powders in the wavelength range of 600 nm to 1600 nm.

4. Analysis of nanoindentation test data

To assess the distribution and stability of nanoindentation properties, we conducted further calculations on the nanoindentation measurement data. Each nanoindentation measurement consists of three steps: (i) load, (ii) hold, and (iii) unload. A load-displacement (h-P) curve was recorded by monitoring the displacement of the indenter versus the applied load associated with material deformation (Fig. S39). Several parameters can be obtained from one representative h-P curve, such as S, P_{max}, h_{max}, h_c, h_p, and h_f, where S is the contact initial unloading stiffness, P_{max} is the maximum applied load, h_{max} is the maximum depth, h_c is the contact depth, h_p is the plastic depth, and h_f is the residual depth. S and h_c are calculated using the equations below.[S11,S12]

$$S = \left(\frac{dP}{dh}\right)_{P_{max}} \tag{2}$$

$$h_c = h_{max} - 0.75\frac{P_{max}}{S} \tag{3}$$

From these obtained parameters, the hardness (H) and reduced Young's modulus (E_r) of the material can be determined.

$$H = \frac{P_{max}}{A(h_c)} \tag{4}$$

$$E_r = \frac{\sqrt{\pi}}{2\sqrt{A(h_c)}} S \tag{5}$$

Here, $A(h_c)$ represents the indentation tip area function related to h_c. For the diamond Berkovich indenter tip with a face angle of 65.27° used in this work, the tip area function is given as $A = 24.5h_c^2$.

5. Calculation of thermodynamic properties in the thermochemical reaction system

Thermochemical reactions play a key role for the laser nanometallurgy-assisted alloy design process proposed in the present study. To verify the thermodynamic feasibility of reaction paths, and understand the underlying reaction mechanisms, it is necessary to calculate the relevant thermodynamic properties of the reaction system. In the B_4C−NiTi reaction system, the probability and priority of all possible reaction paths are related to their enthalpy change (ΔH), entropy change (ΔS), and Gibbs free energy change (ΔG). On the basis of known thermodynamic data, the changes in thermodynamic properties induced per mole of reactants at a given temperature can be calculated by following equations.[S13]

$$\Delta_f H_{298}^0 = \sum \left(n_i H_{298}^0\right)_{products} - \sum \left(m_i H_{298}^0\right)_{reactants} \tag{6}$$

$$\Delta_f S_{298}^0 = \sum \left(n_i S_{298}^0\right)_{products} - \sum \left(m_i S_{298}^0\right)_{reactants} \tag{7}$$

$$\Delta_f G_{298}^0 = \Delta_f H_{298}^0 - T\Delta_f S_{298}^0 \tag{8}$$

Here, $\Delta_f H0\ 298$, $\Delta_f S0\ 298$, and $\Delta_f G0\ 298$ represent the standard enthalpy change, standard entropy change, and standard Gibbs free energy change, respectively. n_i and m_i denote the mole coefficient of products and reactants, respectively. T refers to the thermodynamic temperature. The $\Delta_f G0\ 298$-value of each reaction was estimated via the first-order function, and the curves depicting the temperature dependence of $\Delta_f G0\ 298$ for the thermochemical reactions are shown in Fig. S1. Theoretically calculated values for the thermodynamic properties of all possible thermochemical reactions are summarized in Tables S1 and S2.

Notably, Fig. S1 reveals that within the synthesis temperature range from room temperature

to 3,560 K, the standard Gibbs free energy changes for some of the listed reactions, including the reaction $B_4C \rightarrow 4B + C$, are all positive. They are characterized by their endothermic nature (i.e., positive reaction enthalpy), with the vast majority being decomposition reactions (Table S2). This unequivocally demonstrates that these chemical reactions cannot proceed spontaneously within this melt pool temperature range, and that a continuous external supply of activation energy is required to overcome the reaction energy barriers. It is important to clarify that our proposed target reaction, $3Ti + B_4C \rightarrow 2TiB_2 + TiC$, should not be simplistically regarded as occurring through the sequential steps of the following reactions: $B_4C \rightarrow 4B + C$, $Ti + C \rightarrow TiC$, and $Ti + 2B \rightarrow TiB_2$. Moreover, the products associated with the aforementioned sequential reactions are not the macroscopic forms of B and C substances that can be directly observed; rather, they exist indirectly in the liquid melt pool as free states of [B] and [C] atoms. Indeed, the calculations presented in Fig. S1 reflect the relative priorities of all possible reactions between the B_4C−NiTi system under laser irradiation, which are determined by the standard Gibbs free energy change of each reaction. For the L-PBF process, the laser melt pool generated by the combined effects of the rapid heating of thin layers of functionalized powder by a high-energy-density laser beam and the exothermic in-situ chemical reactions among particles can be approximated as an isolated adiabatic system. As a result, the more pronounced the negative trend in the standard Gibbs free energy change of a reaction, the higher its priority for occurring first. It can be observed that the standard Gibbs free energy changes for the reactions $3Ti + B_4C \rightarrow 2TiB_2 + TiC$ and $5Ti + B_4C \rightarrow 4TiB + TiC$ are significantly lower than those of other reactions, with the latter being even lower. Interestingly, because of the competitive nature of these two reactions, the capacity to achieve lattice-matching with the primarily nucleated TiC nanophase for the preferential formation of an ultrafine heterostructure—coupled with a reduced titanium source requirement—leads to the exclusive formation of TiB_2 rather than TiB in the countless tiny molten pools continuously accumulated under high cooling rates of the LPBF process (Fig. 1, A and F, and Fig. S4). This resulted in the effective suppression of the latter reaction that would otherwise have occurred, which is in stark contrast to the findings have been reported in other literatures.[S14-S16] Thus, from a thermodynamic perspective, the tailored target reaction holds the highest priority in the current system, and the heat released is sufficient to sustain it via self-propagating combustion.

6. Mechanical properties and deformation mechanisms of bulk materials

Figure S40A compares the representative tensile engineering stress-strain curves of these two materials. We found that after implementing the INSHE strategy, the tensile mechanical properties of INSMA improved to a certain extent compared to that of the pristine SMA. Specifically, the ultimate tensile strength (σ_{UTS}) increased from 545.2 MPa to 629.6 MPa, the yield strength (σ_{YS}) reached 250.8 MPa, and the elongation-to-failure (ε) improved to 8.6%. Despite the σ_{YS} value of INSMA is already higher than that of the pristine SMA, it still exhibits a pronounced strain hardening ability, which enables it to achieve enhanced σ_{UTS} during the final plastic deformation stage (Fig. S40B). In addition, the modest improvement in ductility examined is attributed to the fact that, following yielding, the strain hardening rate continues to increase monotonically over an extended true strain range, which helps to counteract plastic instability. Postmortem micro/nano-

structural observations after deformation at the microscale provide a useful reference (Fig. S11 and Fig. S12). One noteworthy conclusion is that under extreme loading, INSMA forms a large number of nanocrystallites through the crystalline fragmentation of its internal dual-nanoprecipitates. This mechanism not only enables the material to accommodate severe deformation, but also imparts ductility through sequential torsion with ongoing deformation.

We further provide the unconfined compression test results for both materials to showcase the optimization potential of INSHE strategy in terms of compressive mechanical properties (Fig. S40C). In contrast, the mechanical performance advantages exhibited by INSMA in compression are even more pronounced. We observed that the fabricated INSMA still maintained a characteristic four-stage compression deformation behavior of the pristine SMA during loading, accompanied by a distinct strain hardening phenomenon after yielding (Fig. S40D): I. The austenitic dominant phase undergoes elastic deformation with a modulus of E_a; II. The critical stress-induced transformation from *A* to *M*, characterized by a low-slope strain plateau; III. The fully reoriented martensite is subjected to elastic deformation with a modulus of E_m and accompanied by detwinning with dislocation slip; IV. After exceeding the critical stress required to initiate plastic deformation of detwinned martensite, dislocation slip occurs within the elastic martensitic phase, leading to yielding with a distinct work-hardening phenomenon until fracture. The aforementioned distinctive deformation stages and strain hardening behavior reveal the complex interplay between the B2 austenite and B19' martensite phases. Therefore, the experimental results obtained from the macroscopic tensile and compressive tests clearly underscore the efficacy of the INSHE strategy in optimizing the mechanical properties of bulk materials, and provide valuable insights for a comprehensive understanding of the mechanical responses and deformation mechanisms in the designed INSMA.

The B2 austenite and B19' martensite phases in NiTi alloys exhibit markedly different elastic behaviors due to their distinct crystal structures and atomic bonding characteristics. The low lattice distortion of the B2 phase, owing to its cubic symmetry, results in uniform deformation under stress, with no significant anisotropy and a stiffer elastic response. The monoclinic structure of the B19' phase exhibits high lattice distortion tolerance, enabling adaptation to external forces through twin boundary slip or variant reorientation, which reduces effective stiffness. Thus, the B2 phase (70−90 GPa) has a higher elastic modulus compared to the B19' phase (30−50 GPa). In this study, DSC analysis results (Fig. S19, B to F) for phase transformation behavior indicate that the B2 phase predominates in the as-printed INSMA at room temperature, while the B19' phase is significantly present in the pristine SMA. This is also confirmed by phase identification results based on XRD patterns (Fig. S19A), which show that both the as-printed INSMA and the pristine SMA consist of B2 and B19' phases at room temperature, with the pristine SMA exhibiting intensified peak signals for the B19' phase. Based on these observations, it can be reasonably inferred that there is a higher content of the B19' phase in pristine SMA compared to INSMA. It is noteworthy that the formed dual-nanoprecipitates are present at concentrations below the characteristic detection limit of XRD, resulting in the absence of discernible diffraction peaks.

Considering the relatively higher B2 phase content in the phase composition of INSMA, thus besides the dispersed high-modulus dual-nanoprecipitates in the matrix, this circumstance also contributes to an increase in the overall elastic modulus of the alloy composed of both B2 and B19' phases.

7. Influence of transformation temperature on the mechanical properties of lattice structures

In this study, the observed differences in transformation characteristic temperatures, such as the martensitic transformation starting temperature (M_s) and austenitic transformation starting temperature (A_s), between the pristine SMA and INSMA, have a significant impact on the compressive mechanical properties of the corresponding lattice structures under low-strain cyclic/gradient loads. Due to the lower transformation characteristic temperatures, the INSMA lattices primarily exhibit a high elastic modulus response of the B2 austenite phase under low compressive strains, offering excellent resistance to deformation and structural stability. As shown in the representative cyclic and gradient engineering stress-strain curves in Fig. 4, Fig. S27, and Fig. S28, the low transformation characteristic temperatures of the INSMA lattices give rise to high stiffness, reduced tendency to plastic deformation, and linear elastic response. When the compressive strain approaches the superelastic threshold, the INSMA lattices can absorb energy through stress-induced transformation (Fig. S29 and Fig. S30), which is advantageous for their mechanical properties. In contrast, for the pristine SMA lattices with higher transformation characteristic temperatures, a larger volume fraction of the B19' martensite phase participates under the same conditions, exhibiting a lower elastic modulus and a tendency to undergo deformation through twinning, hence making it more prone to pseudoelasticity or early-stage plastic deformation.

8. Analysis of variation in transformation latent heat

It is found that the as-printed INSMA shows lower transformation latent heat than the INSMA powder in Table S3. Considering the unique in-situ thermochemical reactions and nanoscale precipitation behaviors involved in the printing process, a detailed explanation is given below.

(1) Reaction-induced compositional segregation and elemental loss. For NiTi SMAs, the exact TTs range (i.e., A_f-A_s and M_s-M_f) depends on the width of the peak in the DSC curve. The TTs range and the TTs themselves are considered to be affected by the chemical inhomogeneity of the NiTi matrix, and if the Ti-content exhibits elemental segregation, it is possible that the TTs range will end up being extended over a wider area.[S17,S18] Clearly, in the printed INSMA, Ti atoms are consumed due to their targeted participation in laser-excited in-situ thermochemical reactions, resulting in a relatively elevated Ni content in the binary Ni−Ti system. The above nanometallurgical process leads to the chemical inhomogeneity changes of Ti-content in the NiTi matrix, which broadens the final TTs range. As a result, the endothermic/exothermic peaks in the DSC curve are diluted and the corresponding apparent peak areas (latent heat integration values) are reduced.

(2) Mechanical constraints and stress shielding due to precipitates. Indeed, the presence of reinforcement particles affects the phase transformation behavior of the NiTi matrix, thereby leading to a reduction in the transformation latent heat, which has been reported in numerous literatures.[S19-S21] In the entire build volume of the printed INSMA, the extensive formation of robust dual-nanoprecipitates within the B2 austenite, along with their strong interfacial bonding with the matrix and the surrounding high-density dislocation networks (Fig. S10), restrict the transformation strain of the parent phase. It is evident that this pinning effect impedes the migration of the B19' martensite variant/B2 austenite interfaces, suppressing phase transformation in certain regions and reducing the effective transformation volume. Moreover, the disparity in thermal expansion coefficients between the thermodynamically stable, non-transformative dual-nanoprecipitates and the matrix readily creates a thermal mismatch stress field that induces localized residual stresses. This in turn diminishes the driving force for the phase transformation, necessitating additional energy to overcome the stress barrier, which manifests as a reduction in the transformation latent heat. In contrast, for the functionalized INSMA powder, the B_4C nanoprecursors adhering to the surfaces of the base alloy particles do not affect the internal phase transformation behavior, nor do any laser-matter interaction processes occur.

9. Explanation of the results of contact angle measurements

In Fig. S25, the observed decrease in the contact angle of the INSMA results from the significant reduction in its surface roughness relative to the pristine SMA. This is corroborated by the quantitative evaluation results from 3D surface profile measurements for the surface topography of as-built INSMA and pristine SMA (Fig. S23 and Fig. S24), including roughness average (S_a), root-mean-square roughness (S_q), and peak-to-valley roughness (S_z). According to the Wenzel wetting theory model,[S22,S23] the relationship between variations in a solid's surface roughness and the contact angle of a liquid droplet can be described as follows.

$$\cos\theta^{*} = \mathrm{r}_f \cos\theta \tag{9}$$

where θ^* and θ represent the apparent contact angle of a rough surface and the intrinsic contact angle of a smooth surface, respectively. r_f refers to the solid surface roughness factor, which signifies the ratio of actual surface area to apparent geometric surface area.

For the hydrophobic metallic alloys in the Wenzel regime characterized by θ values exceeding 90° in this study, their corresponding cos θ values are all negative. In this case, the surface roughness reduced by the well-fused surface states of INSMA leads to an increase in the cos θ^* value, which in turn contributes to a decrease in the θ^* value. This is considered as the direct reason for the decrease in the contact angle of INSMA, indicating that it possesses a more obvious surface wetting behavior with increased hydrophilicity level in comparison.

10. Description of micro-CT characterization results

In a typical micro-CT imaging procedure, the lattice structure sample to be examined is secured by bonding its base to an aluminum support using a strong adhesive, ensuring stability during 360° rotational scans. However, this procedure can readily induce slight misalignments in the internal topology of the lattice structure sample relative to the measurement coordinate system, and these subtle discrepancies are subsequently amplified during data acquisition with the two-dimensional flat panel detector. This phenomenon has little impact on dense bulk samples, which generally do not emphasize precise internal topological details. Furthermore, based on the three-dimensional reconstructed and visualized data (Fig. S26, A and C, and Movie S6), when performing corresponding two-dimensional projection analyses on the *XY*, *XZ*, and *YZ* planes of the lattice structure samples (Fig. S26, B and D), it is challenging to maintain perfect alignment of the vertically designated slices (upper, middle, and lower) for both INSMA and SMA materials. The aforementioned factors are the primary reasons for the observed differences in the surface topological features between the INSMA and SMA lattice structures. Given that this segment of the micro-CT results serves to substantiate the feasibility of achieving unprecedented printing fidelity and overall optimization on internal quality through the in-situ nanoscale heterostructure engineering (INSHE) strategy, we cautiously consider that the nine positions selected from the lattice structures of the two materials remain valid comparative references for revealing the limitations of manufacturing accuracy. It is additionally important to emphasize that, to maintain consistency, the same metamaterial design model was employed. Thus, the surface topographies inherent in the additively manufactured INSMA and SMA lattice structures are entirely universal and broadly representative.

11. Estimation of the thermoelastic effect

The thermoelastic effect, which describes the reversible coupling between thermal variations and mechanical responses during the stress-induced thermoelastic martensitic transformation, is one of the key characteristics of shape memory alloys. This effect enables shape memory alloys to undergo phase transformations in response to minute variations in temperature or stress, accompanied by a significant conversion between thermal energy and mechanical energy, thereby serving as the physical basis for their intelligent functionalities (e.g., shape recovery and energy harvesting). To this end, we determined the isothermal entropy change (ΔS_{iso}) of INSMA using the transformation latent heat ($\bar{Q}$) measured by DSC under stress-free conditions (Fig. S19 and Table S3), as a preliminary characterization of its thermoelastic effect. The stress-induced isothermal entropy change associated with the typical first-order martensitic transformation in shape memory alloys can be calculated using the following Clausius-Clapeyron equation.[S24]

$$\Delta S_{\mathrm{iso}\,(0 \to \sigma)} = -\Delta\varepsilon \frac{\mathrm{d}\sigma}{\mathrm{d}T} \tag{10}$$

Here, $\Delta\varepsilon$ represents the strain amplitude of phase transformation, and $\frac{\mathrm{d}\sigma}{\mathrm{d}T}$ denotes the rate of change of the critical stress with temperature. The theoretical isothermal entropy change, as determined directly from the DSC thermogram, can be approximated as follows.

$$\Delta S_{\mathrm{iso}} = \frac{\bar{Q}}{T_0} \tag{11}$$

$$T_0 = \frac{(M_{\mathrm{s}} + A_{\mathrm{f}})}{2} \tag{12}$$

where T_0 is the equilibrium temperature of the phase transformation, M_{s} is the martensitic transformation starting temperature, and A_{f} is the austenitic transformation finish temperature. Therefore, the corresponding theoretical adiabatic temperature change (ΔT_{ad}) can be expressed as follows.

$$\Delta T_{\mathrm{ad}} = -\Delta S_{\mathrm{iso}} \frac{T}{c} \tag{13}$$

where T and c refer to the ambient temperature and specific heat capacity, respectively. Our calculations indicate that the absolute adiabatic temperature change ($|\Delta T_{\mathrm{ad}}|$) used to quantify the thermoelastic effect is 15.5 K for the INSMA, compared to 32.4 K for the pristine SMA, suggesting that the thermoelastic effect in INSMA is theoretically weaker than that of the pristine SMA. It should not be ignored that the above represents merely an indirect characterization method under static condition. A comprehensive evaluation requires further direct methods, such as dense thermocouple monitoring or non-contact infrared thermography, to record the real-time, full-field temperature evolution under actual operating conditions.

12. Corrosion behavior

Figure S44A presents the evolution of open circuit potential (OCP) with time for the as-fabricated pristine SMA and surface-modified INSMA samples in 3.5 wt.% NaCl solution at room temperature (25 ± 2 °C), prior to conducting further electrochemical measurements. Both materials exhibit stable OCP curves without pronounced fluctuations or persistent shifts toward more negative values. The OCP values eventually stabilized at -901.54 mV (vs. SCE) for the pristine SMA and -988.05 mV (vs. SCE) for the INSMA. Since the OCP reflects the overall electrochemical behavior of the tested surface, with higher values generally indicative of superior corrosion resistance, these results suggest that INSMA possesses marginally enhanced corrosion resistance compared with pristine SMA. Figure S44B shows the potentiodynamic polarization

curves of both materials measured in 3.5 wt.% NaCl solution, revealing pronounced passivation regions. Notably, the surface-modified INSMA exhibits a higher breakdown potential (E_b), indicating enhanced stability of its passive film compared with the pristine SMA. Both materials display passivation ranges of comparable width. By applying least-squares fitting to the Tafel regions, the key electrochemical parameters, including corrosion current density (I_{corr}), corrosion potential (E_{corr}), anodic Tafel slope (β_a), and cathodic Tafel slope (β_c), were extracted, as summarized in Table S8. The polarization resistance (R_p) was calculated by:[S25]

$$R_p = \frac{\beta_a \beta_c}{2.3 \cdot (\beta_a + \beta_c) \times I_{corr}} \tag{14}$$

Since corrosion current density is proportional to the corrosion rate, a lower I_{corr} combined with higher polarization resistance reflects superior corrosion resistance. Consistently, the fitted results demonstrate that the INSMA possesses enhanced corrosion resistance over pristine SMA, as evidenced by its lower I_{corr} (2.509 μA·cm^{-2}), higher E_{corr} (-1374.85 mV), and higher R_p (2.998×10^4 Ω·cm^2), corroborating the OCP results.

EIS measurements were conducted to quantitatively evaluate the surface conditions and barrier properties of the two materials in 3.5 wt.% NaCl solution. As shown in the Nyquist plots (Fig. S45A), the impedance response consists of two depressed capacitive arcs, indicative of a double-layer structure at the metal-solution interface. The diameter of the capacitive arcs reflects the corrosion resistance, with larger semicircles indicating superior performance. The corresponding equivalent circuit model used for fitting the EIS data is presented in Fig. S45D, where R_s represents the solution resistance, R_f is the film resistance on the surface, CPE_1 is the capacitance of the intact anodic film, R_{ct} is the Faradaic charge-transfer resistance, and CPE_2 is the interfacial double-layer capacitance. The Bode plots (Fig. S45, B and C) further reveal two distinct peaks for both pristine SMA and INSMA: a major peak at middle frequencies (phase angles close 75-80°) and a minor peak at low frequencies (phase angles close 40-65°). The impedance moduli exhibit a broad linear region in the middle frequency range, confirming that the properties of the passive oxide film predominantly govern the impedance behavior. In this regime, the capacitance of the film can be related to its thickness (d) according to:[S26]

$$C = \frac{\varepsilon \varepsilon_0 A}{d} \tag{15}$$

where ε is the dielectric constant, ε_0 is the permittivity of vacuum, and A and d represent the surface area and thickness of the film, respectively. Moreover, the effective capacitance associated with the *CPE* element can be defined as:[S27]

$$C_{eff} = [Q \times R_f^{(1-\alpha)}]^{-\alpha} \tag{16}$$

where Q and α are the *CPE* parameters, and R_f is the film resistance on the surface. Accordingly, d is inversely proportional to $[Q \times R_f^{(1-\alpha)}]^{-\alpha}$. The fitted results of EIS data are summarized in Table S9. Based on the parameters in Table S9 and Equations (15) and (16), the INSMA exhibits a higher calculated film thickness (d). In addition, its fitted R_f value (65.54 kΩ·cm^2) is greater than that of the pristine SMA (51.58 kΩ·cm^2). These findings confirm that the surface-modified INSMA possesses superior corrosion resistance compared with the pristine SMA, fully consistent with the conclusions drawn from the OCP and potentiodynamic polarization results.

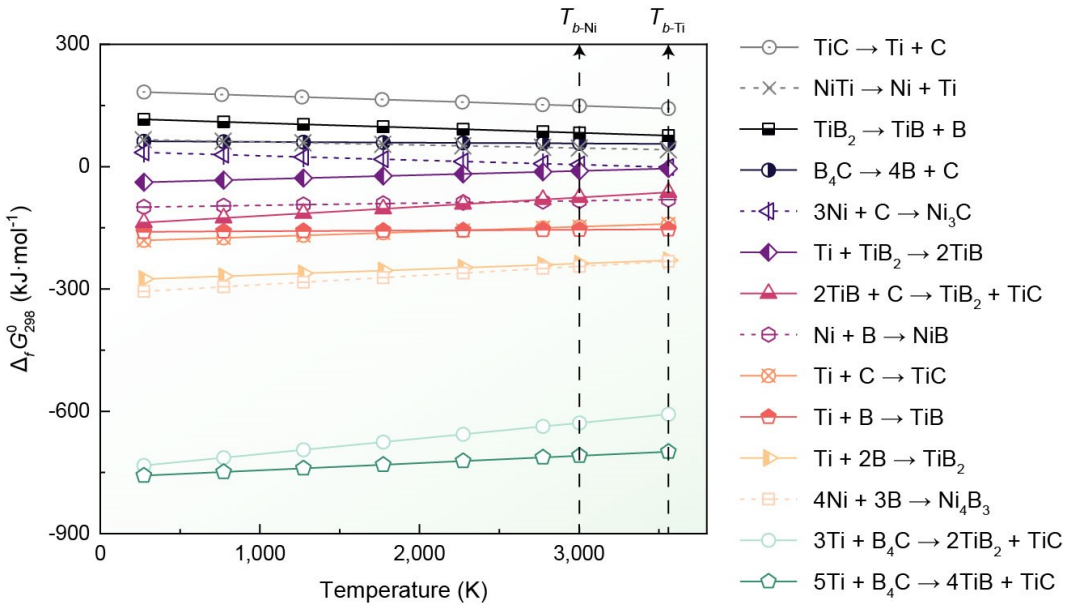

Figure S1. Temperature dependence of the standard Gibbs free energy changes ($\Delta_f G0$ 298) for all possible reactions involved in this work. Where reactions involving the Ni element are labelled as dashed lines. $T_{b\text{-Ni}}$ (~3,005 K) and $T_{b\text{-Ti}}$ (~3,560 K) represent the boiling points of the Ni and Ti elements, respectively.

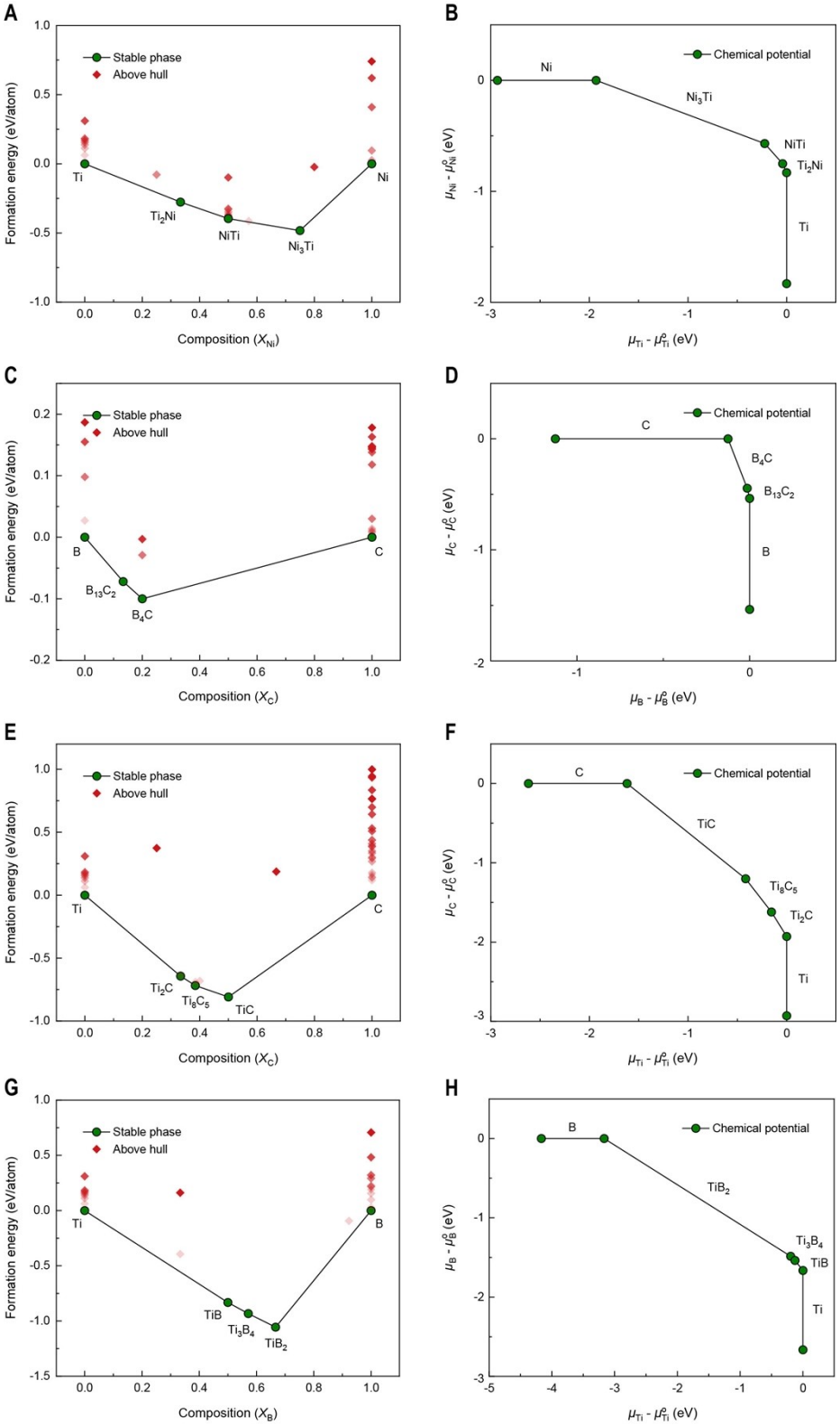

Figure S2. Convex hull diagrams and chemical potential diagrams in different binary systems. (**A** and **B**) Ni-Ti system. (**C** and **D**) B-C system. (**E** and **F**) Ti-C system. (**G** and **H**) Ti-B system.

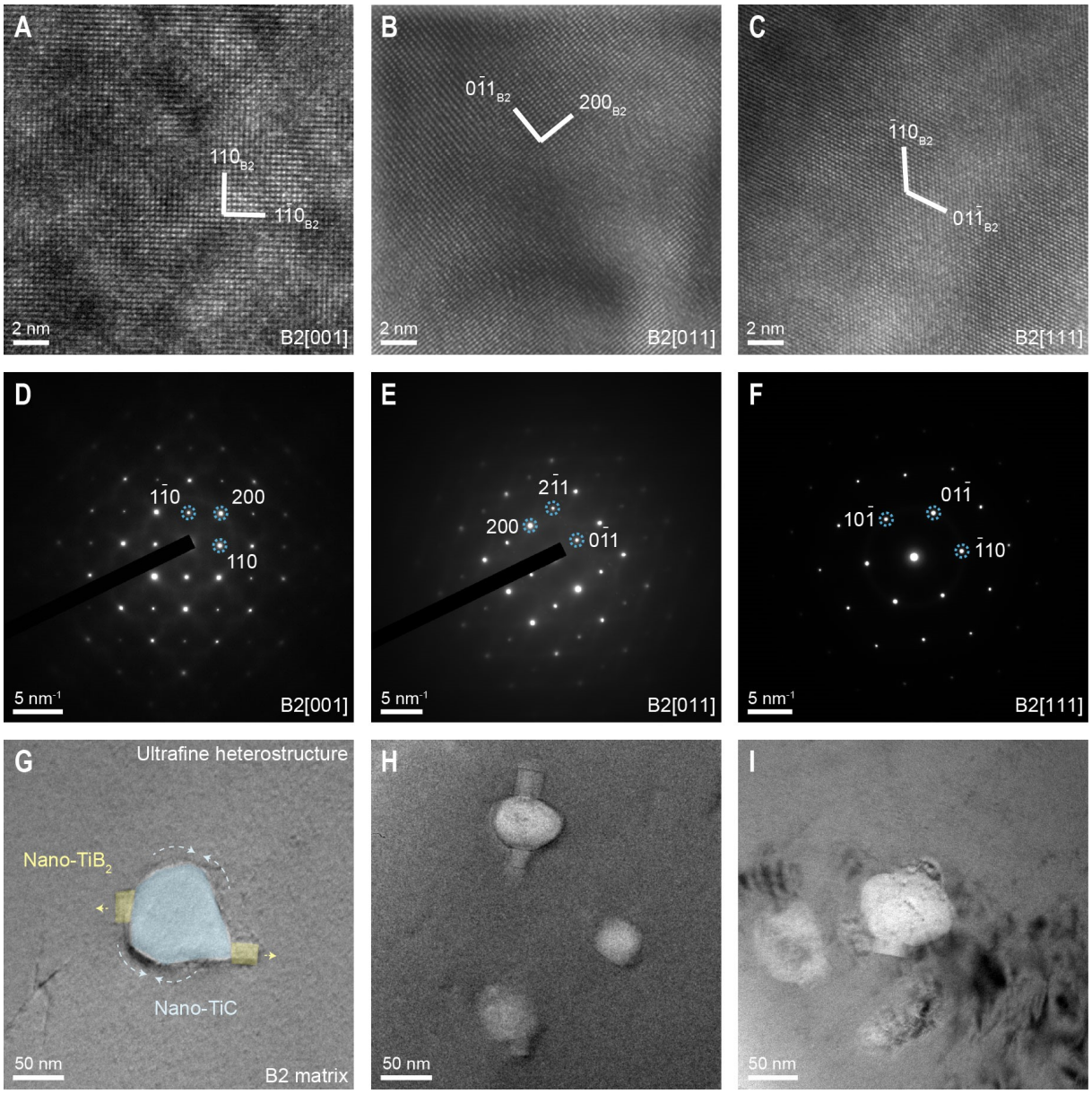

Figure S3. TEM characterization of B2 austenite matrix and other diffuse heterostructured nanoprecipitates. (**A** to **C**) High-resolution TEM (HRTEM) images and (**D** to **F**) selected area electron diffraction (SAED) patterns of the B2 austenite matrix captured in [001], [011], and [111] zone axis projections, respectively. (**G** to **I**) TEM images of ultrafine heterostructured nanoprecipitates with various morphologies in B2 austenite matrix. The nano-TiB_2 phase is marked in yellow and the nano-TiC phase is marked in blue in the dual-nanoprecipitates.

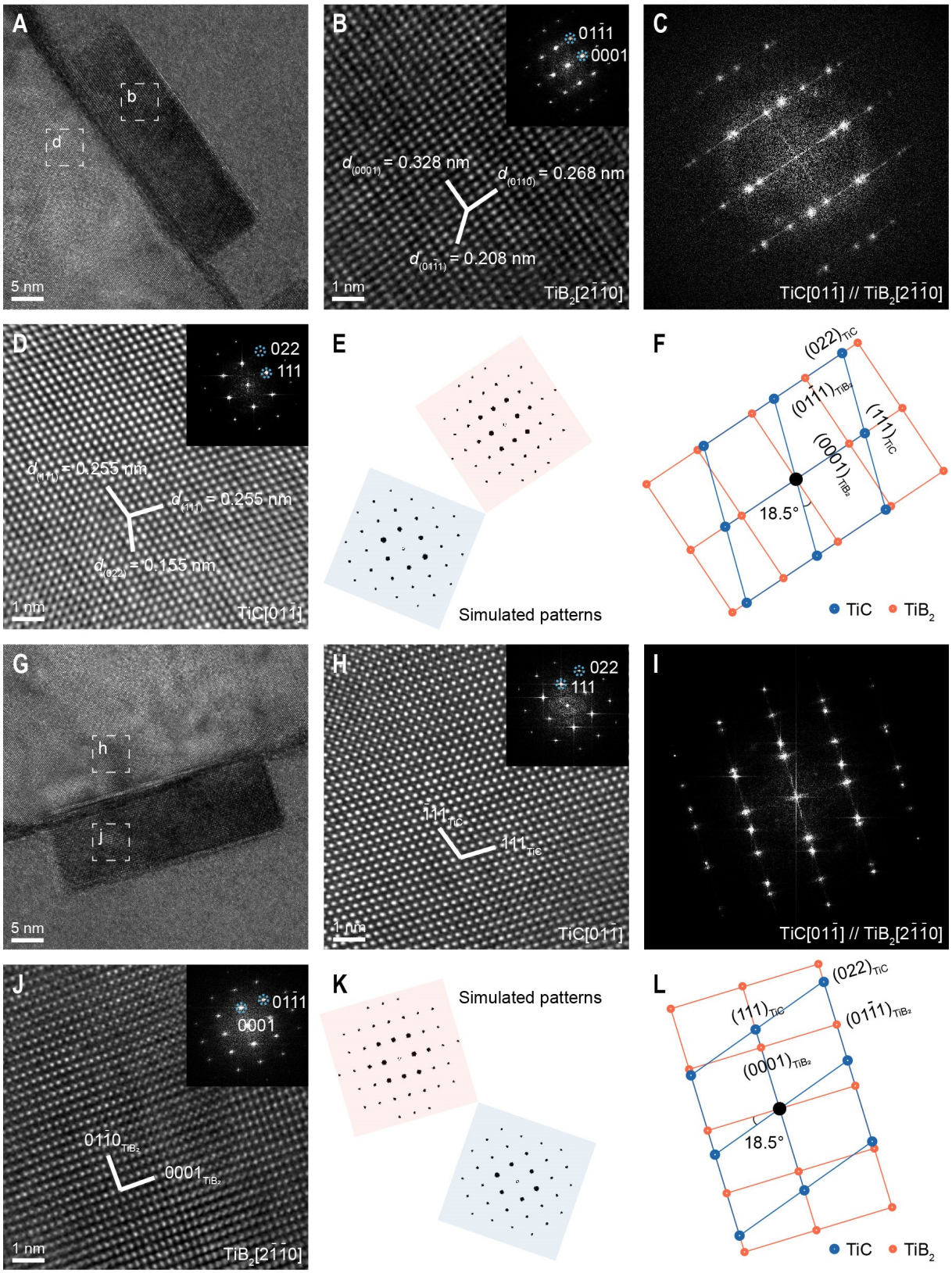

Figure S4. Partitioned ultrafine heterostructure featuring preferential crystallographic orientation relationships (ORs) for dual-nanoprecipitates in Fig. 1D. (**A** and **C**) HRTEM image and associated

fast Fourier transform (FFT) pattern of the ultrafine heterostructure located to the right of the dual-nanoprecipitates. Apparently, the two heterostructures located on the right side have exactly the same OR. (**B** and **D**) HRTEM images captured from TiB_2 side and TiC side for the boxed regions in (A), respectively. Insets show the FFT patterns from the TiB_2 and TiC phase structures. (**E** and **F**) Simulated diffraction patterns for indexation corresponding to (C), showing the coherent TiC/TiB_2 interface parallel to the close-packed $(111)_{TiC}$ and $(0001)_{TiB_2}$ planes. The projection direction is $[01\bar{1}]_{TiC//}[2\bar{1}\bar{1}0]_{TiB_2}$. (**G** and **I**) HRTEM image and associated FFT pattern of the ultrafine heterostructure located below the dual-nanoprecipitates. (**H** and **J**) HRTEM images captured from TiC side and TiB_2 side for the boxed regions in (G), respectively. Insets show the FFT patterns from the TiC and TiB_2 phase structures. (**K** and **L**) Simulated diffraction patterns corresponding to (I), showing the coherent TiC/TiB_2 interface parallel to the close-packed $(111)_{TiC}$ and $(0001)_{TiB_2}$ planes. The projection direction is $[01\bar{1}]_{TiC//}[2\bar{1}\bar{1}0]_{TiB_2}$. These results suggest that the ORs of ultrafine heterostructures at all different partitions in the same dual-nanoprecipitates are equivalent.

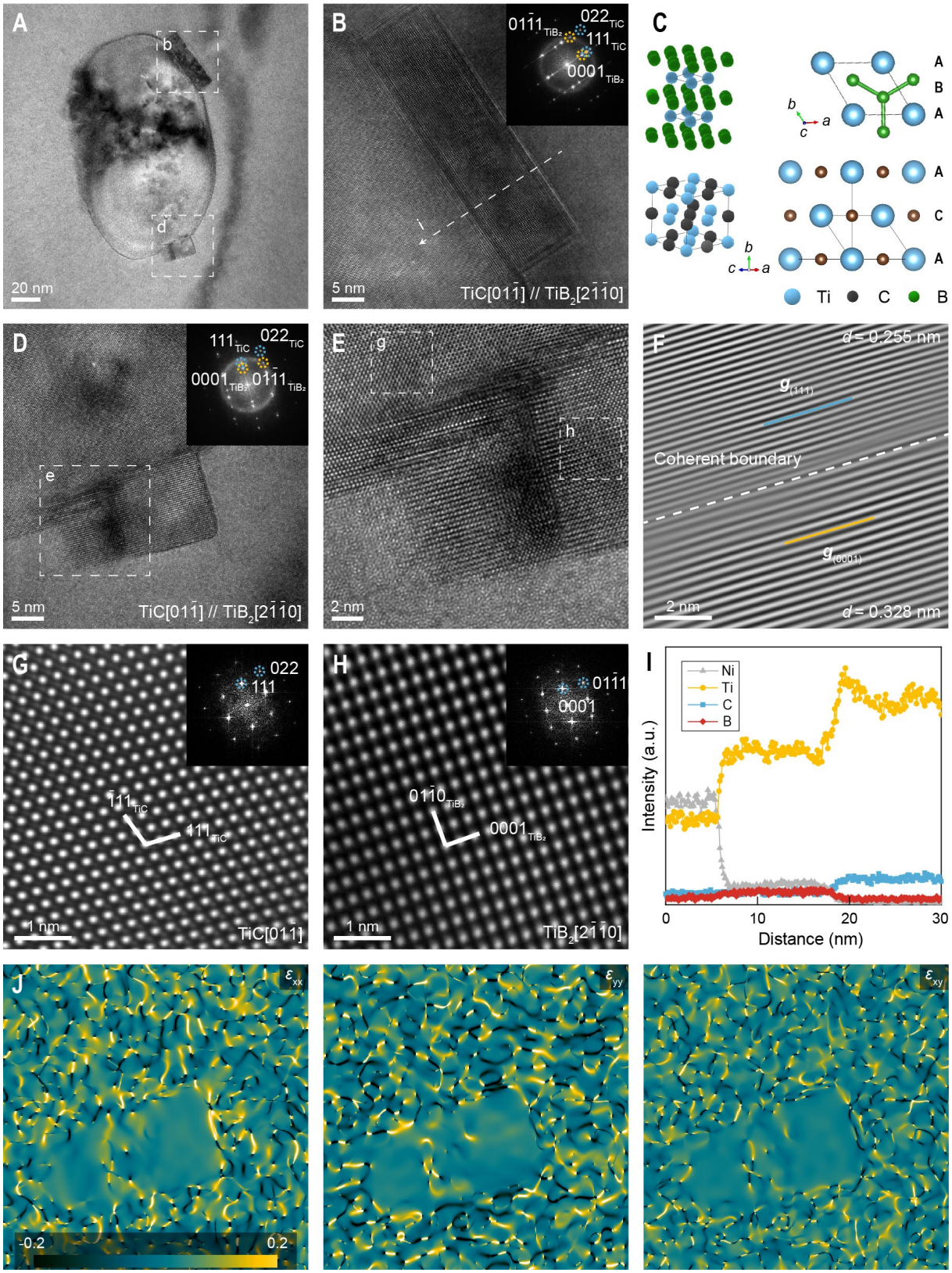

Figure S5. Structural analysis of dual-nanoprecipitates during lattice assembly. (**A**) TEM image showing a dual-nanoprecipitate undergoing lattice assembly. (**B** and **D**) HRTEM images and

associated FFT patterns (the insets) of ultrafine heterostructures for the boxed regions in (A). (**C**) Simulated atomic structure models illustrating the atomic stacking sequence at the coherent TiC/TiB_2 interface $(111)_{TiC//}{}^{(0001)_{TiB_2}}$. The projection direction is $[01\bar{1}]_{TiC//}{}^{[2\bar{1}\bar{1}0]_{TiB_2}}$. (**E**) The zoomed-in HRTEM image of the boxed region in (D), showing the lattice assembly process of the lattice-matched heterogeneous phase with nucleation and growth on the perfectly flat and clean bare surface of the primary nucleation phase. (**F**) Inverse FFT (IFFT) image recorded along the reciprocal lattice vectors $\boldsymbol{g}^{(111)}$ and $\boldsymbol{g}^{(0001)}$ at the TiC/TiB_2 interface showing parallel lattice fringes and coherent boundary without mismatch dislocations. TiC was marked in blue and TiB_2 was marked in yellow. (**G** and **H**) Atomic-resolution TEM images of the box regions in (E) showing the periodic atomic columns taken with the $[01\bar{1}]_{TiC}$ zone axis and $[2\bar{1}\bar{1}0]_{TiB_2}$ zone axis in the heterostructure. (**I**) TEM-EDX line-scanning showing the compositional profile across the interfaces of nano-TiC, nano-TiB_2, and B2 austenite matrix in (B). (**J**) Strain analysis by geometric phase analysis (GPA) of the ultrafine heterostructure in (D). ε_{xx}, ε_{yy}, and ε_{xy} are the normal strains along the *xx*, *yy*, and *xy* directions, respectively. These results suggest that the ORs of ultrafine heterostructures at all different partitions in the various dual-nanoprecipitates are also equivalent.

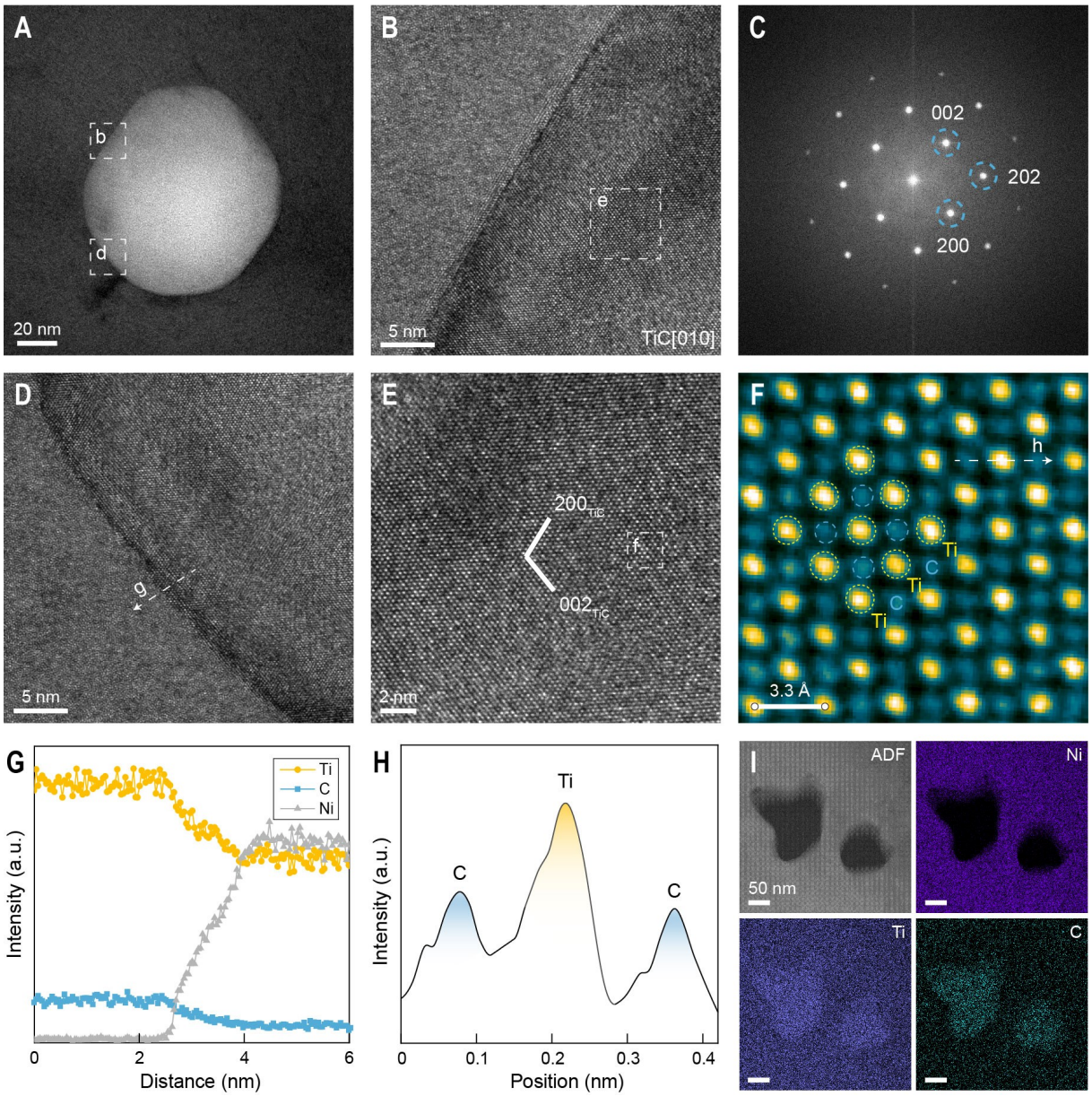

Figure S6. TEM characterization of individually primary nucleated TiC nanoprecipitates. (**A**) TEM image of TiC nanoprecipitate with granular growth morphology reveals size-dependent feature. (**B** and **D**) HRTEM images captured from the TiC nanoprecipitate boundaries for the boxed regions in (A). (**C** and **E**) HRTEM image and associated FFT pattern of the TiC nanoprecipitate. (**F**) Atomic-resolution TEM image of the box region in (E) shows the periodic atomic arrangements of TiC nanoprecipitate taken with the [010] zone axis. (**G**) TEM-EDS line-scanning showing the compositional profile across the interface of the TiC nanoprecipitate and B2 austenite matrix in (D). (**H**) Intensity line profiles of the white dashed region in (F). (**I**) ADF-STEM image and TEM-EDS elemental maps of TiC nanoprecipitates.

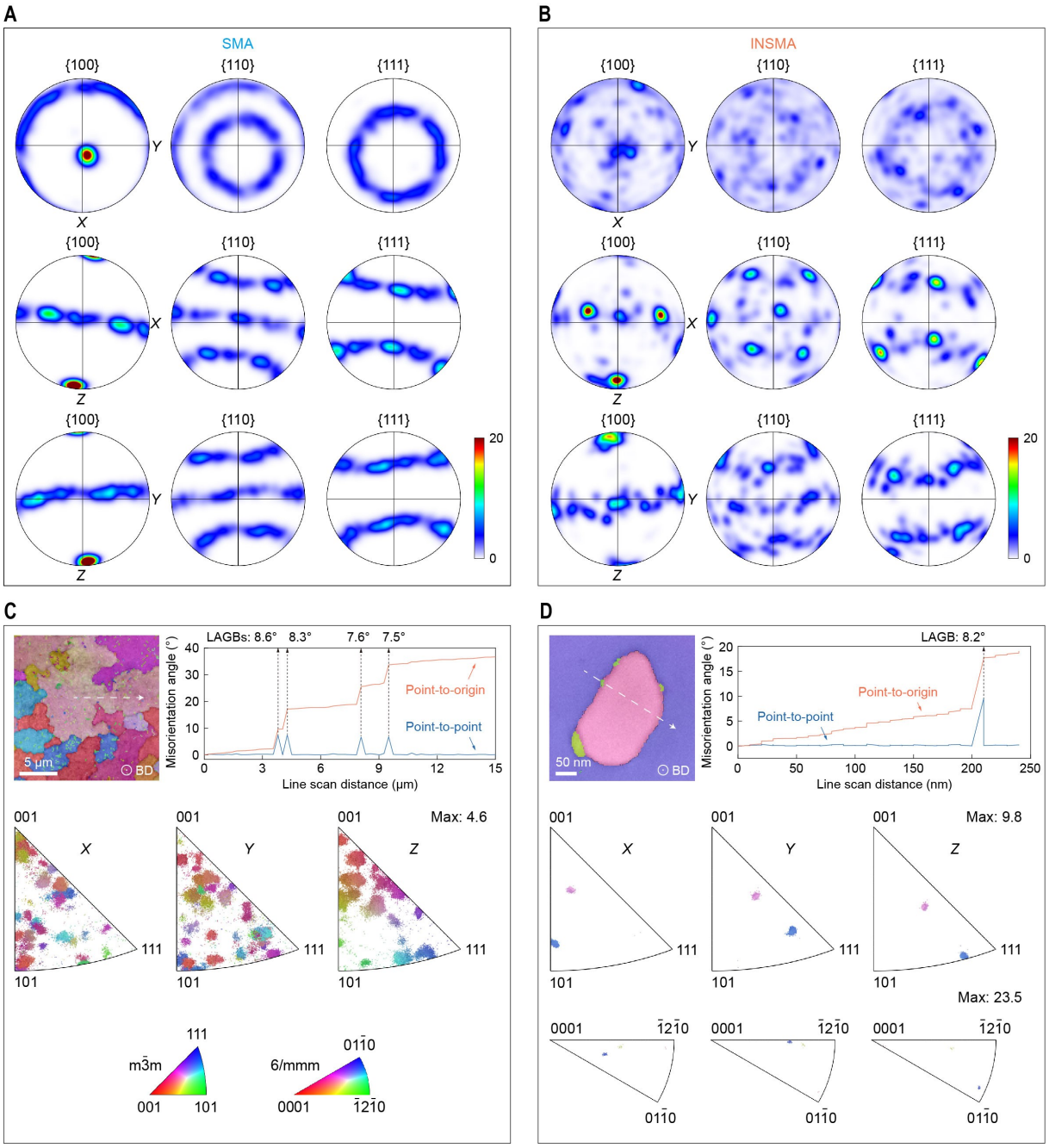

Figure S7. Texture orientation analysis. (**A** and **B**) Pole figures of pristine SMA (A) and INSMA (B) perpendicular to the build direction (BD), scan direction (SD), and transverse direction (TD), respectively. (**C** and **D**) TKD inverse pole figure (IPF) orientation color maps, point-to-point and point-to-origin misorientation angle variations along the dashed line for dual-nanoprecipitates in the INSMA sample taken perpendicular to the BD. *X*-, *Y*-, and *Z*-axis orientations from the grains coordinate system with respect to the sample's coordinate system, showing the microstructure's texture for different as-printed samples (Note: *X* is parallel to SD, *Y* is parallel to TD and *Z* is parallel to BD).

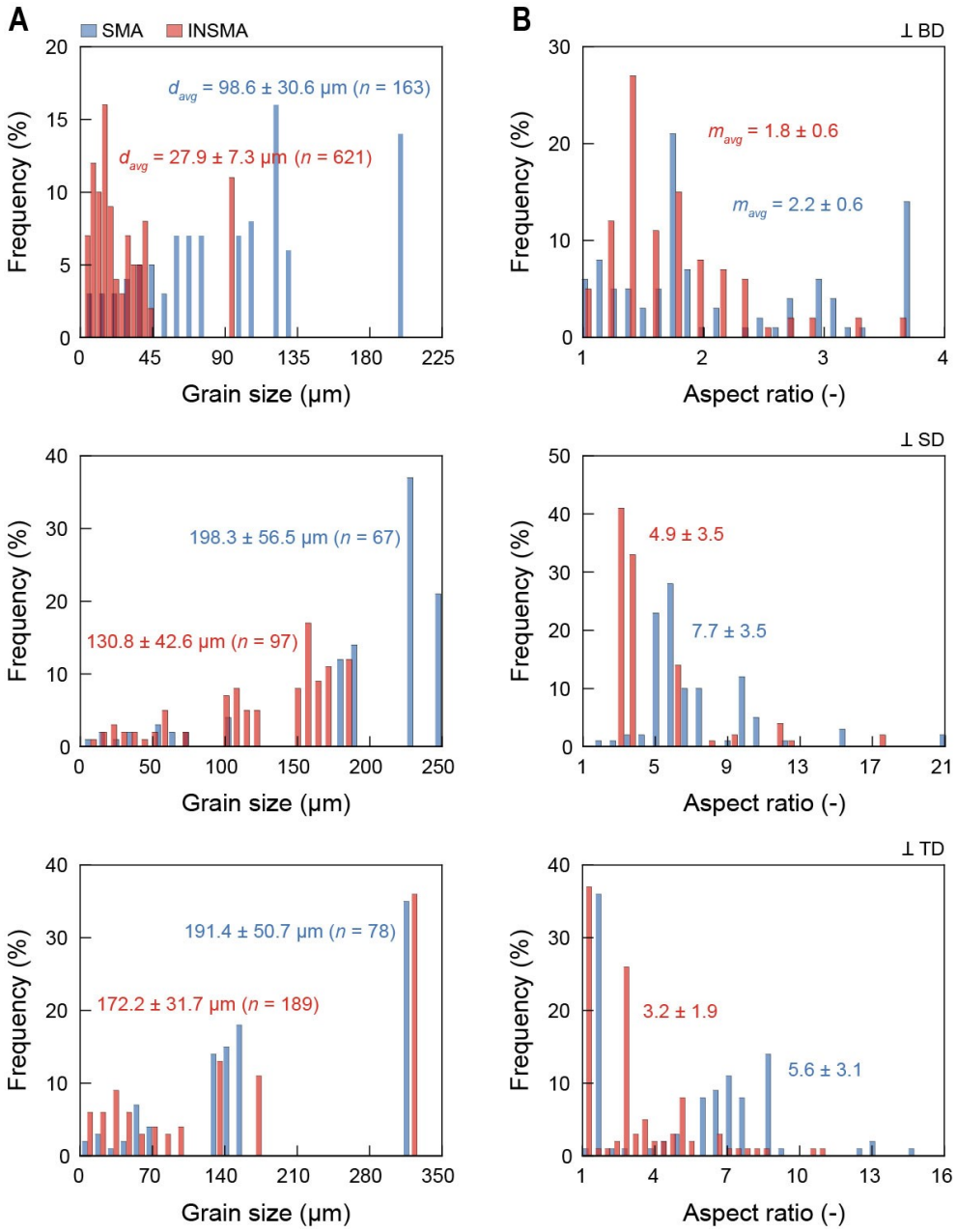

Figure S8. Grain size and grain shape analysis based on EBSD characterization. (**A** and **B**) Grain size distributions (A) and aspect ratio distributions (B) perpendicular to the BD, SD, and TD of crystallographic orientations in SMA and INSMA, respectively (Note: n is the number of grains; d_{avg} is the average value of the equivalent circle diameter in the grain size distribution; m_{avg} is the average value of the fitted ellipse aspect ratio in the aspect ratio distribution).

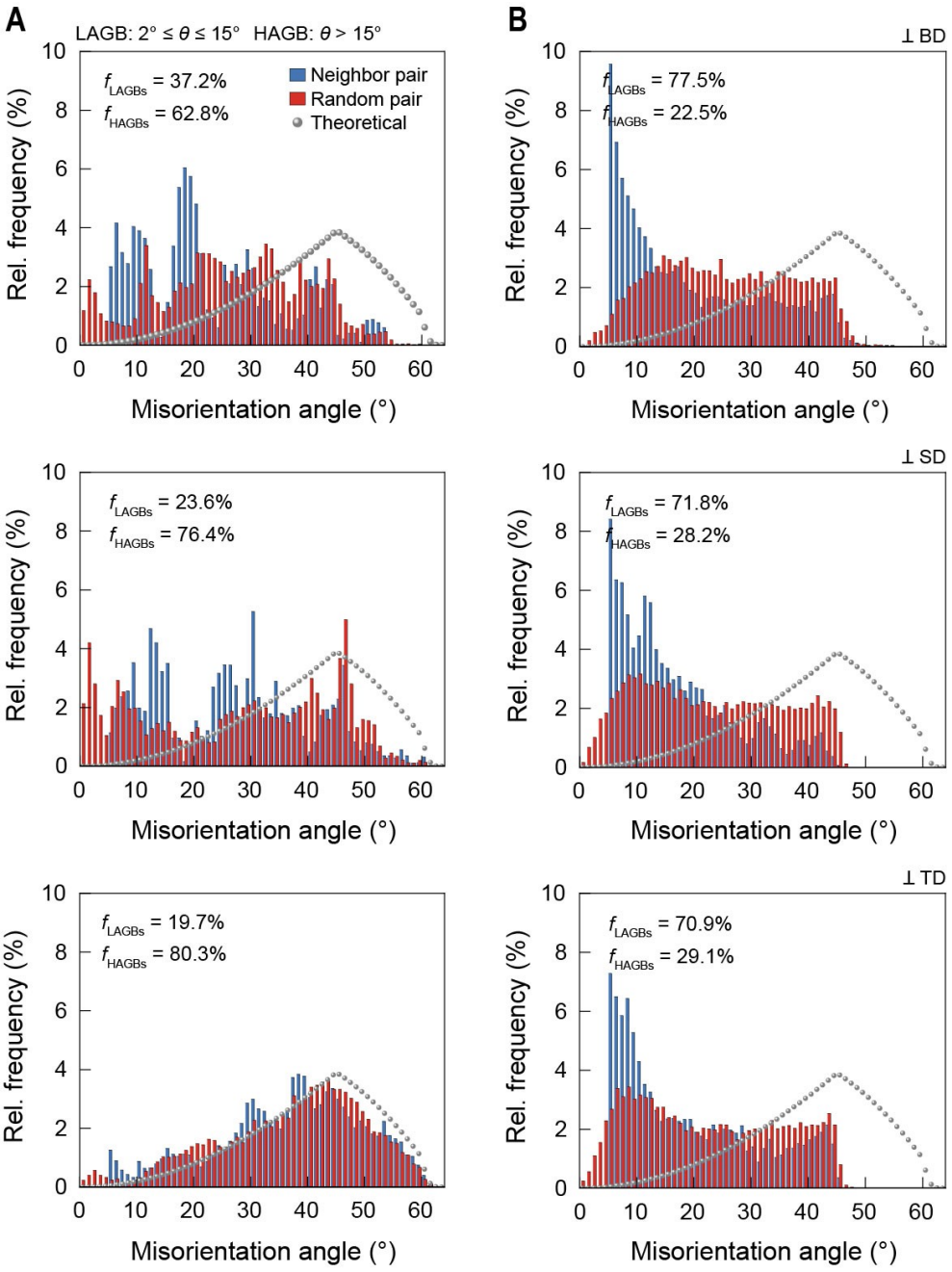

Figure S9. Grain boundary (GB) analysis based on EBSD characterization. (**A** and **B**) Misorientation angle distributions perpendicular to the BD, SD, and TD of crystallographic orientations in SMA (A) and INSMA (B), respectively.

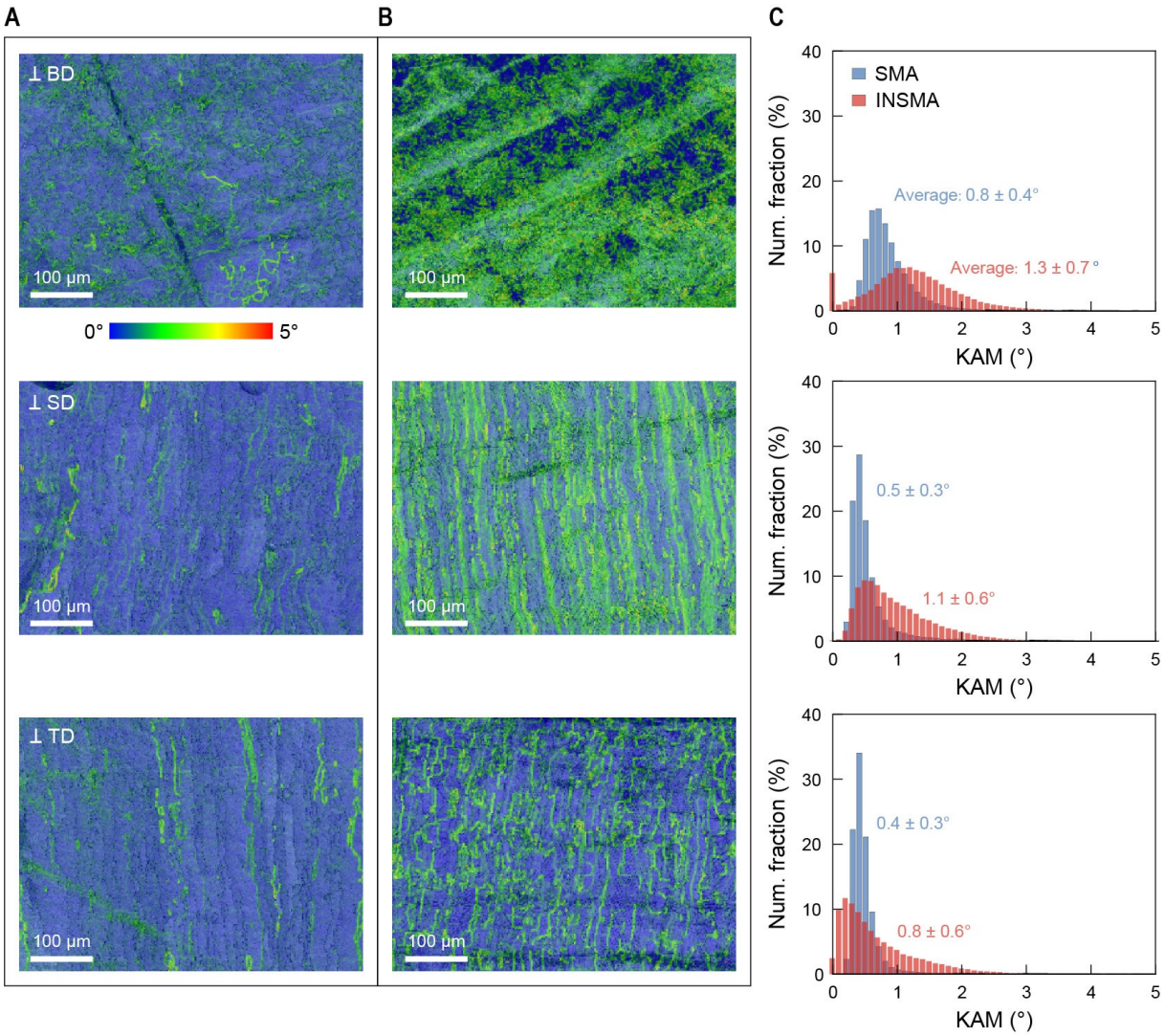

Figure S10. Local misorientation analysis. (**A** to **C**) Kernel average misorientation (KAM) maps and corresponding KAM distributions perpendicular to the BD, SD, and TD of crystallographic orientations in SMA (A) and INSMA (B), respectively.

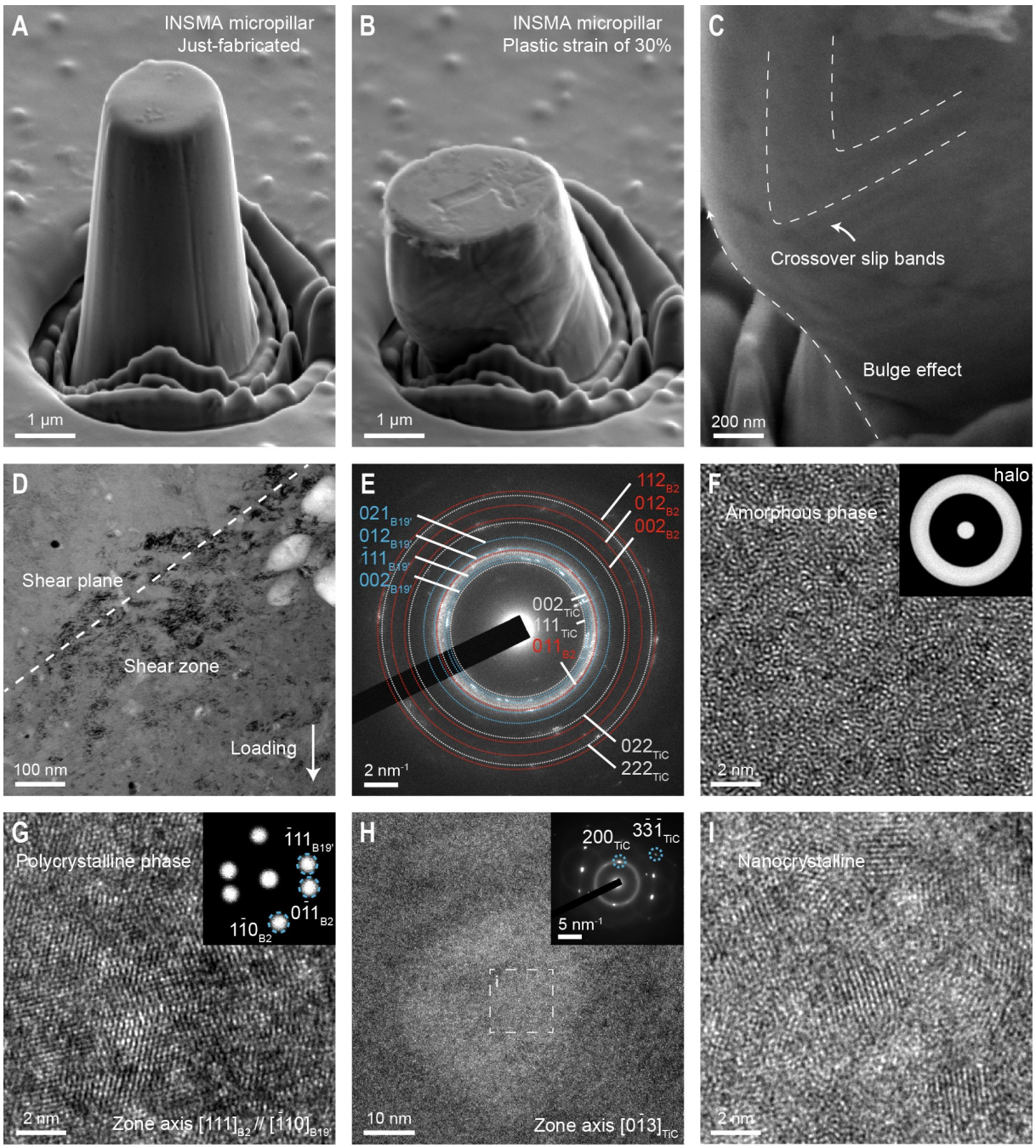

Figure S11. Morphology and nanostructure of the plastically deformed INSMA micropillar. (**A**) Just-fabricated. (**B** and **C**) Subjected to monotonic compression under the plastic strain of 30%. (**D**) Bright-field TEM image with (**E**) corresponding SAED pattern at the shear zone. (**F** and **G**) HRTEM images and masked FFT patterns (the insets) show the coexistence of amorphous and polycrystalline phases in the B2 austenite matrix. (**H** and **I**) HRTEM images and corresponding SAED pattern (inset) show nanocrystallites within the dual-nanoprecipitate.

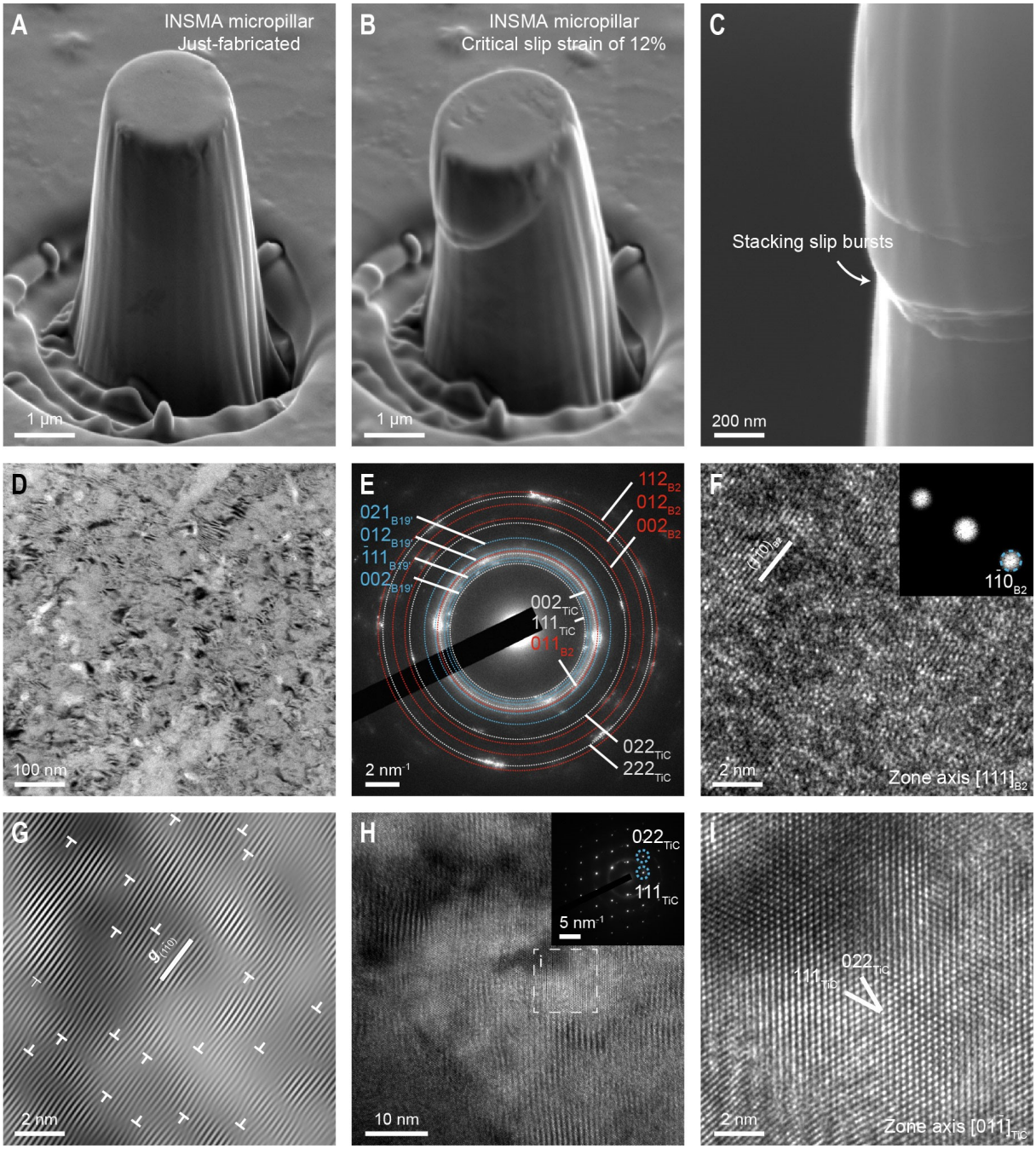

Figure S12. Morphology and nanostructure of the slip-deformed INSMA micropillar. (**A**) Just-fabricated. (**B** and **C**) Subjected to monotonic compression under the critical slip strain of 12%. (**D**) Bright-field TEM image with (**E**) corresponding SAED pattern at the shear zone. (**F**) HRTEM image, masked FFT pattern (inset), and (**G**) IFFT image recorded along the reciprocal lattice vectors $\boldsymbol{g}(\bar{1}\bar{1}0)$ showing lattice fringes and widespread dislocations. Symbol '⊥' shows location of dislocations. (**H** and **I**) HRTEM images and corresponding SAED pattern (inset) of the dual-nanoprecipitate.

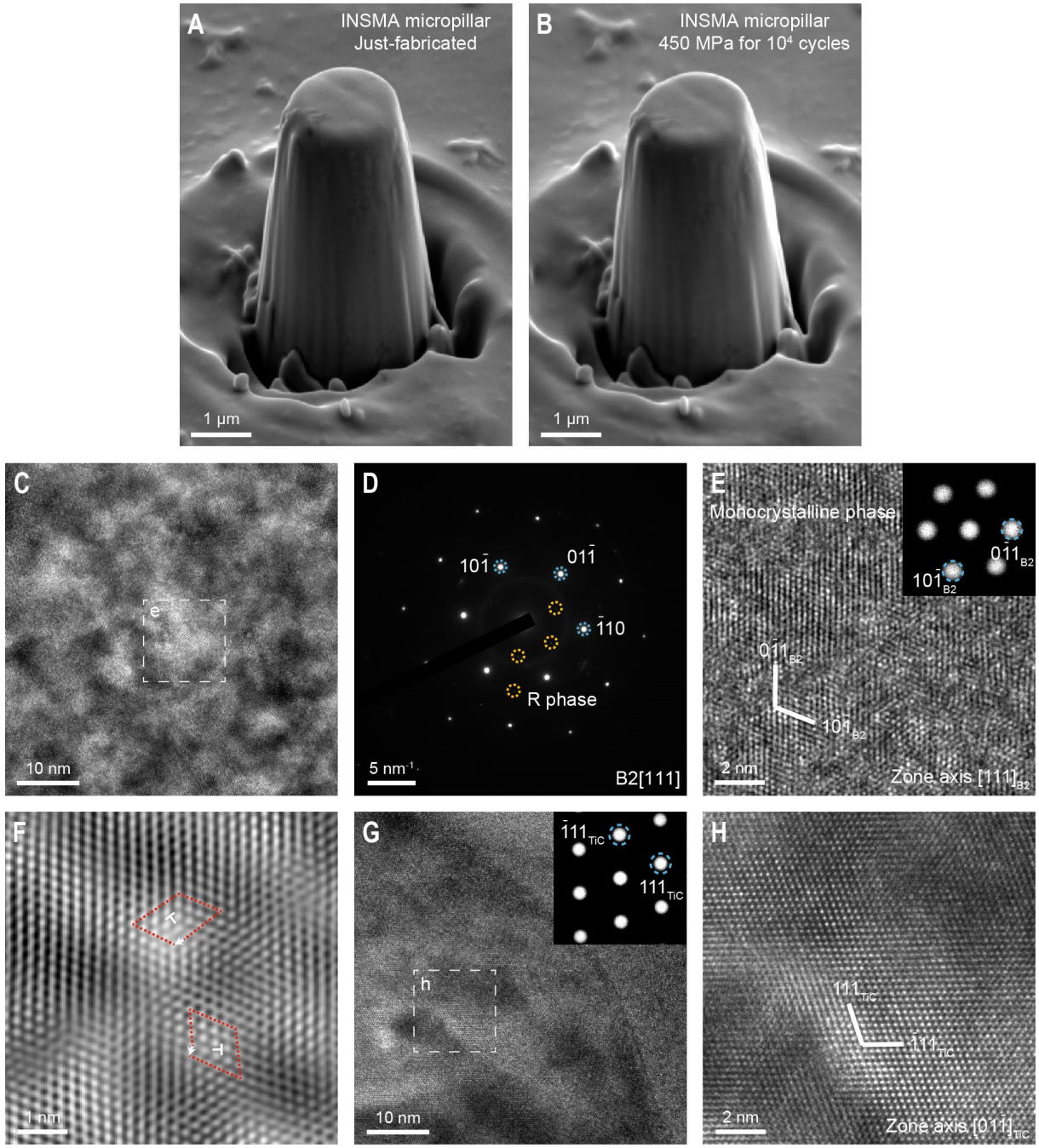

Figure S13. Morphology and nanostructure of the cyclically deformed INSMA micropillar. (**A**) Just-fabricated. (**B**) After 10^4 cycles of compression under the stress of 450 MPa. (**C**) Bright-field TEM image with (**D**) corresponding SAED pattern of the SMA matrix. (**E**) HRTEM image, masked FFT pattern (inset), and (**F**) IFFT image showing the monocrystalline phase contains a few concentrated dislocations. The white arrows indicate the Burger's vector of the dislocations. (**G** and **H**) HRTEM images and masked FFT pattern (inset) of the dual-nanoprecipitate.

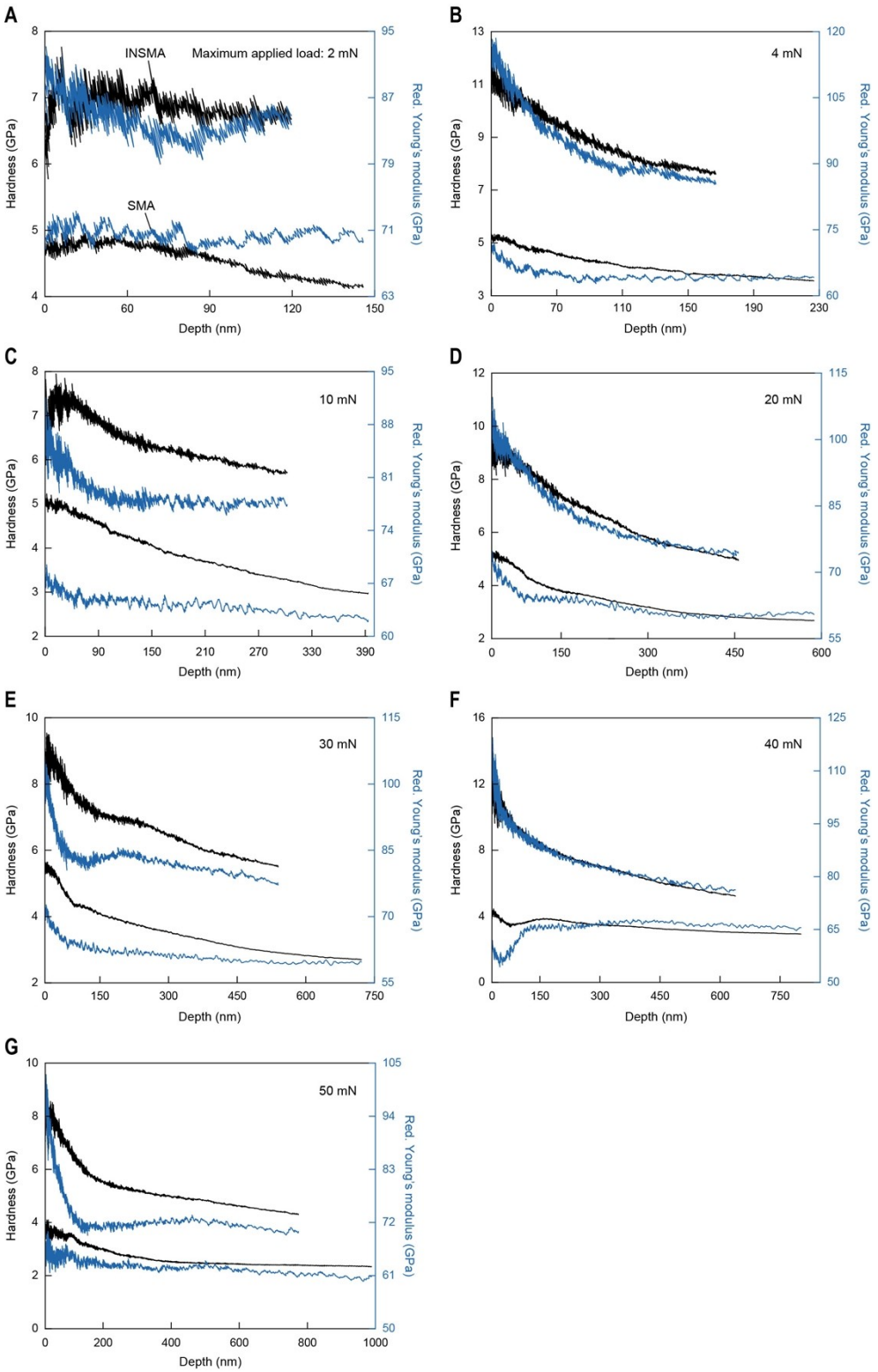

Figure S14. Hardness and reduced Young's modulus as a function of contact depth measured by the continuous stiffness measurement method (CSM).

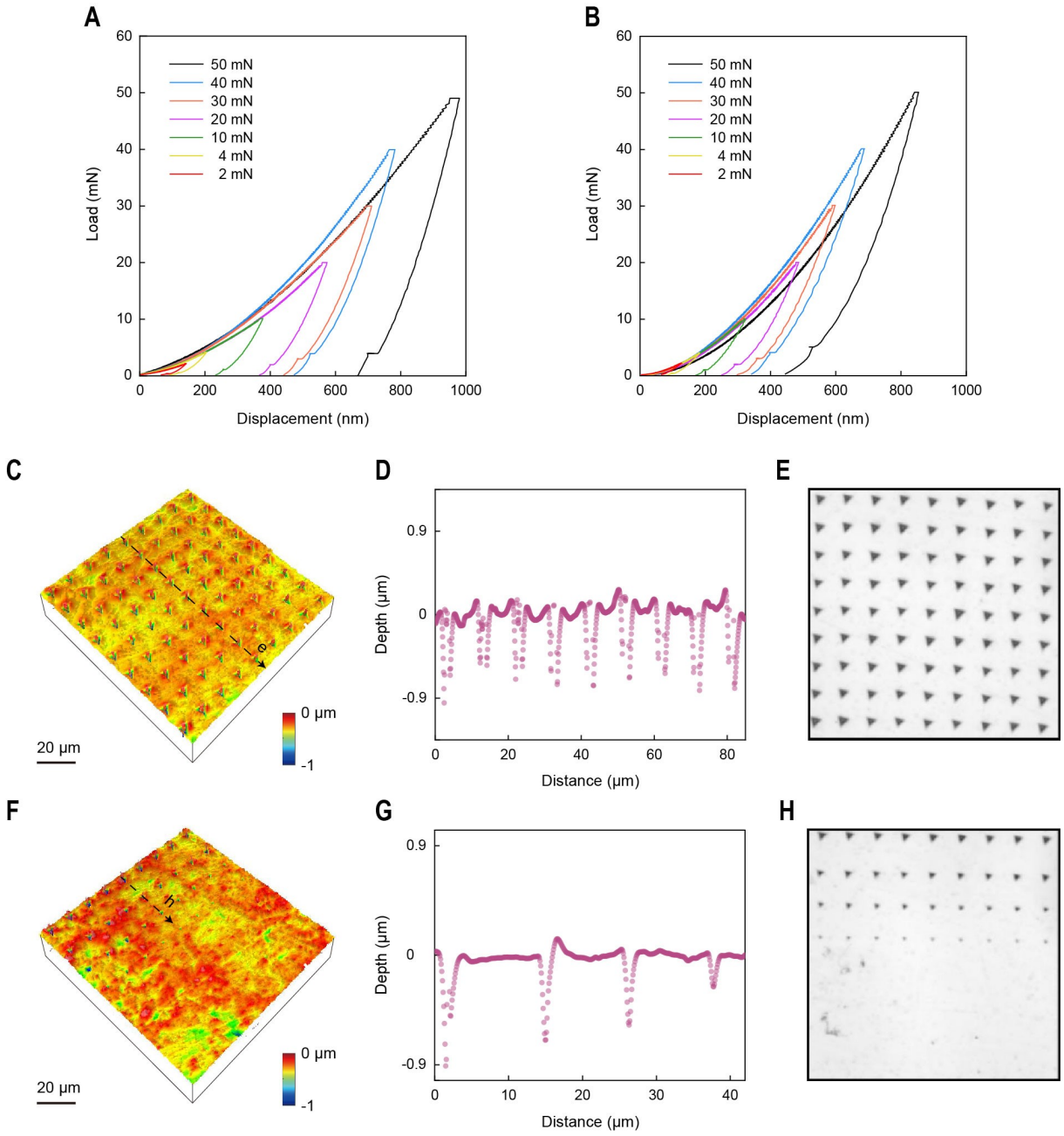

Figure S15. Repeatability and stability evaluation of nanomechanical properties from indentation size effects. (**A** and **B**) Representative indentation load-displacement (*h*-*P*) curves of SMA (A) and INSMA (B) for gradient applied maximum loads. 3D surface topographies, cross-sectional profiles, and optical images of the INSMA sample from the (**C** to **E**) continuous and (**F** to **H**) gradient indentation measurements. These results suggest that the lattice matching strategy by the introduction of dual-nanoprecipitates can improve the nanomechanical properties and machinability of SMA matrix.

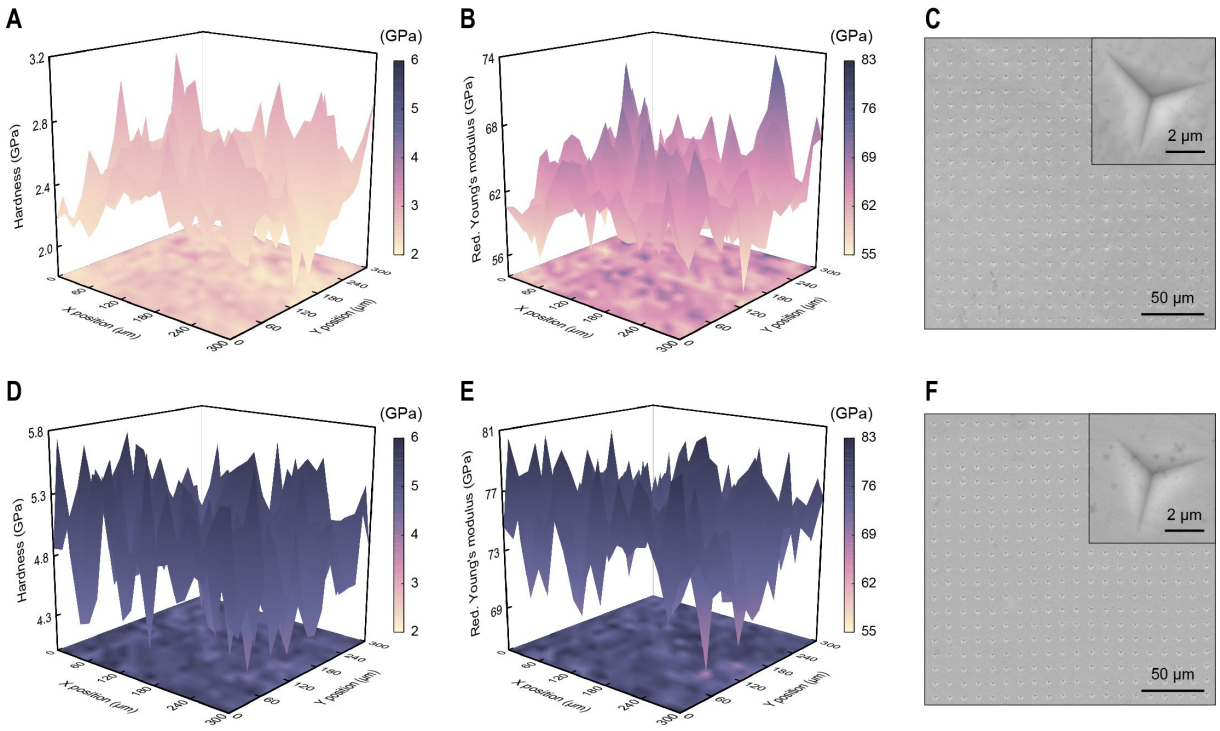

Figure S16. Nanoindentation measurement mappings. Hardness and reduced Young's modulus distributions from (**A** to **C**) SMA and (**D** to **F**) INSMA corresponding to the two micrographs. The 3D histogram showing data from 400 nanoindentation measurements. (**C** and **F**) SEM images of the indentation array after indenter loading, the inset showing an individual indentation morphology at high magnification.

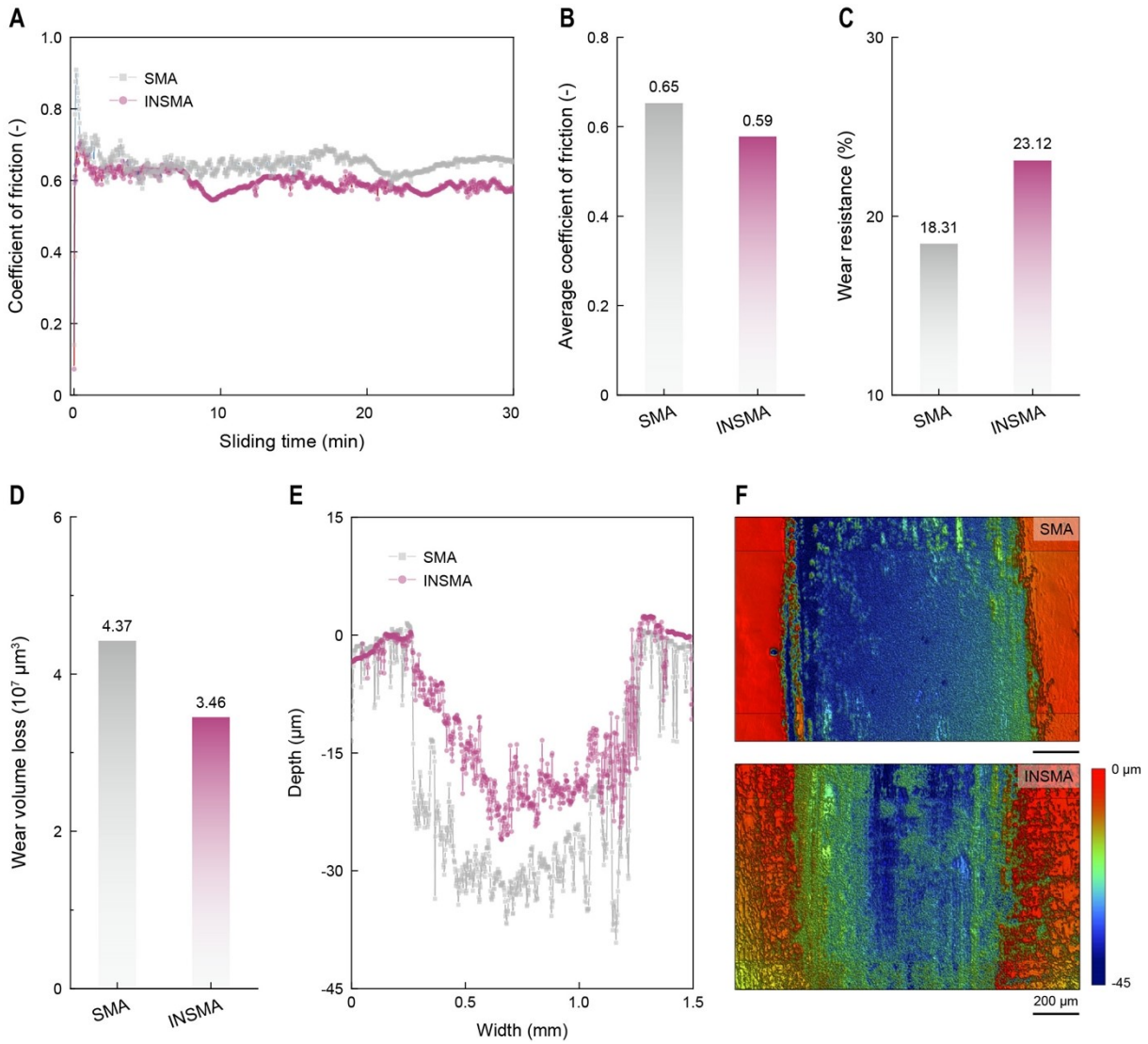

Figure S17. Characterization of tribological properties. (**A**) A plot of coefficient of friction (COF) as a function of sliding time. (**B** to **D**) Average COF, wear resistance, and wear volume loss of LPBF-AM SMA and INSMA. (**E** and **F**) Cross-sectional profiles and 2D contour mappings of the wear tracks.

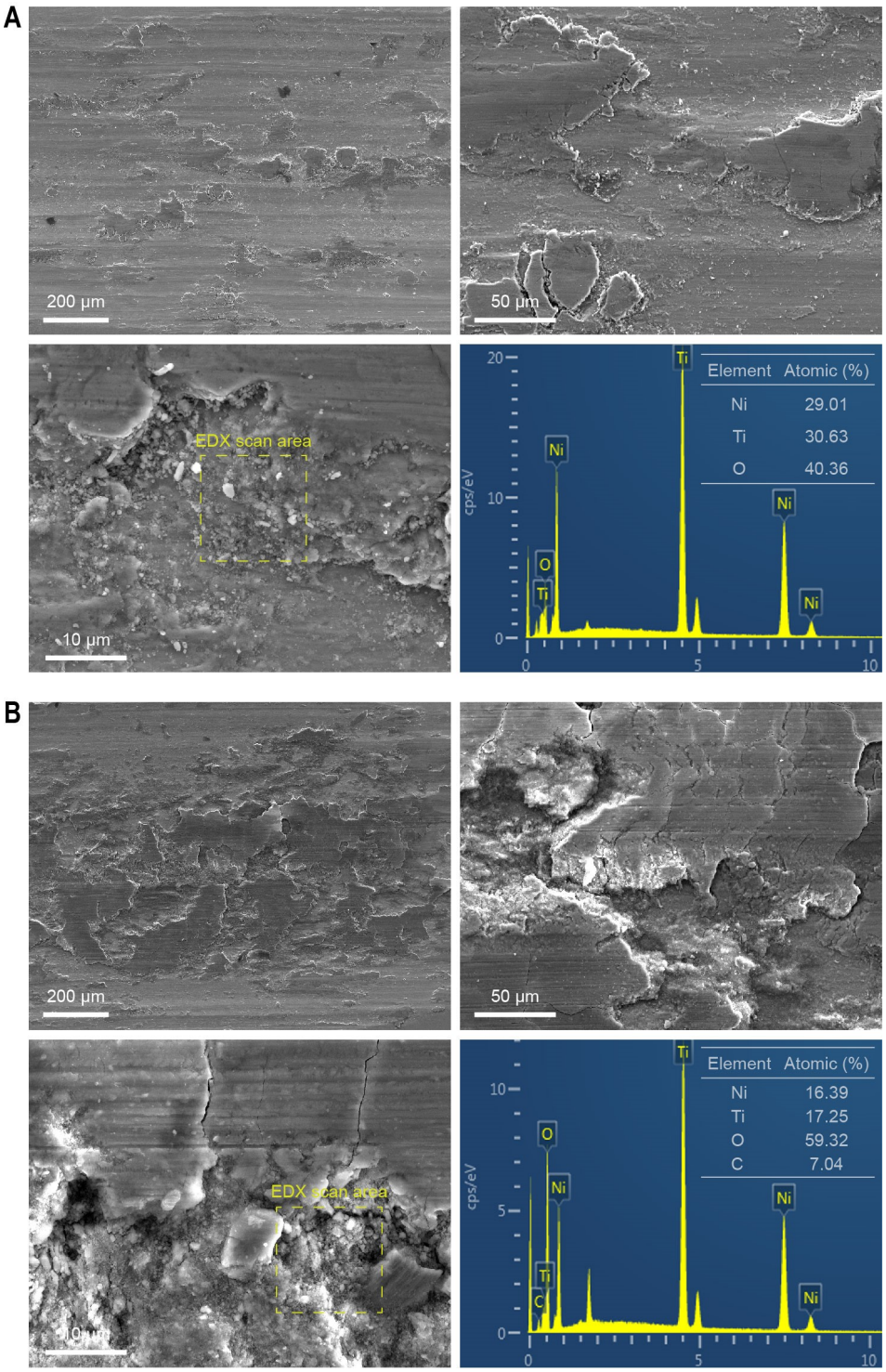

Figure S18. SEM characterizations of worn surface morphologies. Morphological features and elemental composition of wear tracks for (**A**) SMA and (**B**) INSMA samples. SEM-EDX scan areas are marked with dashed boxes.

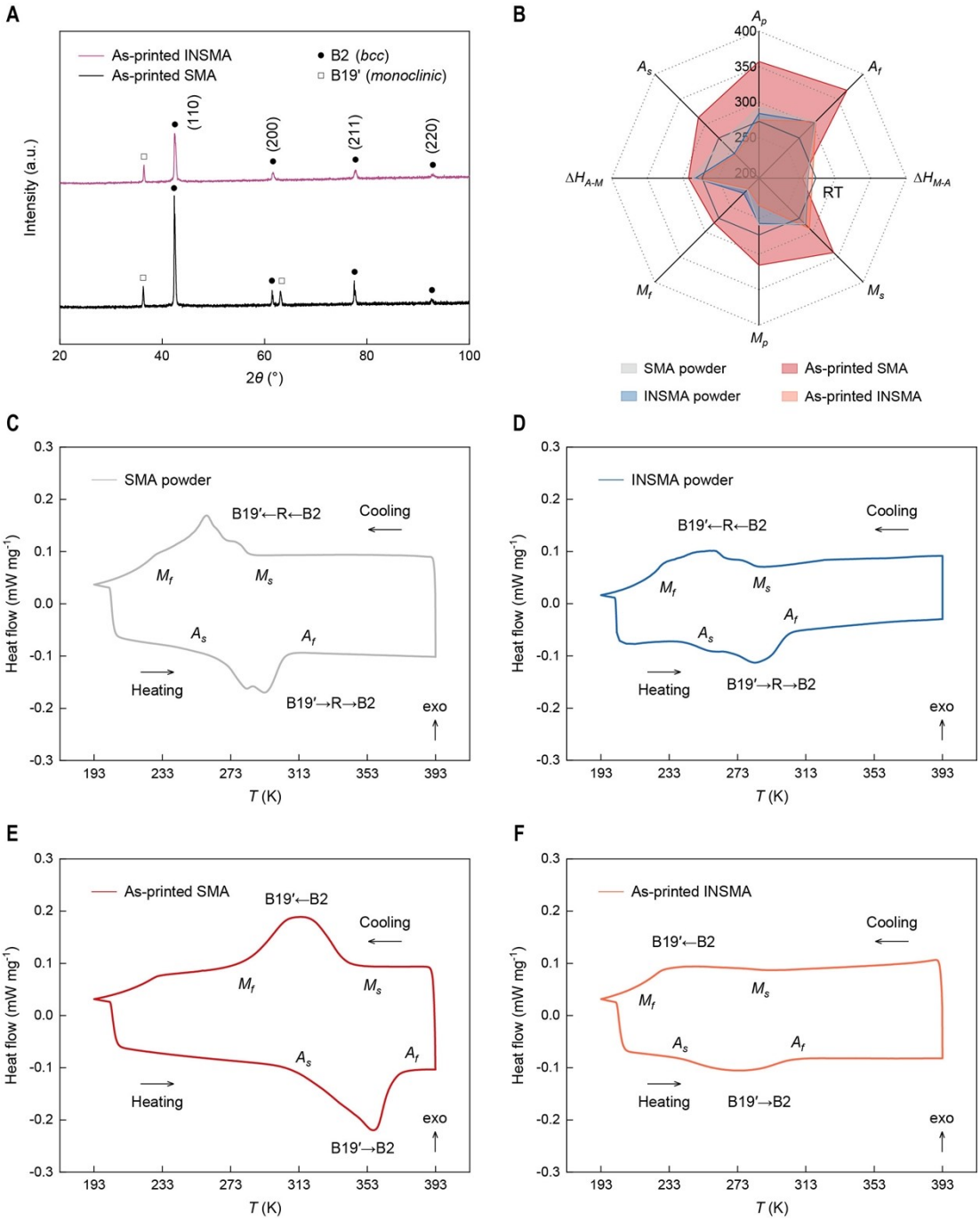

Figure S19. Characterization of phase constitution and phase transformation behavior. (**A**) XRD patterns of LPBF-AM as-printed SMA and INSMA. (**B**) Radar chart of the characteristic temperatures for martensitic transformation extracted from DSC thermograms. (**C** to **F**) DSC thermograms of the powder samples and as-printed samples.

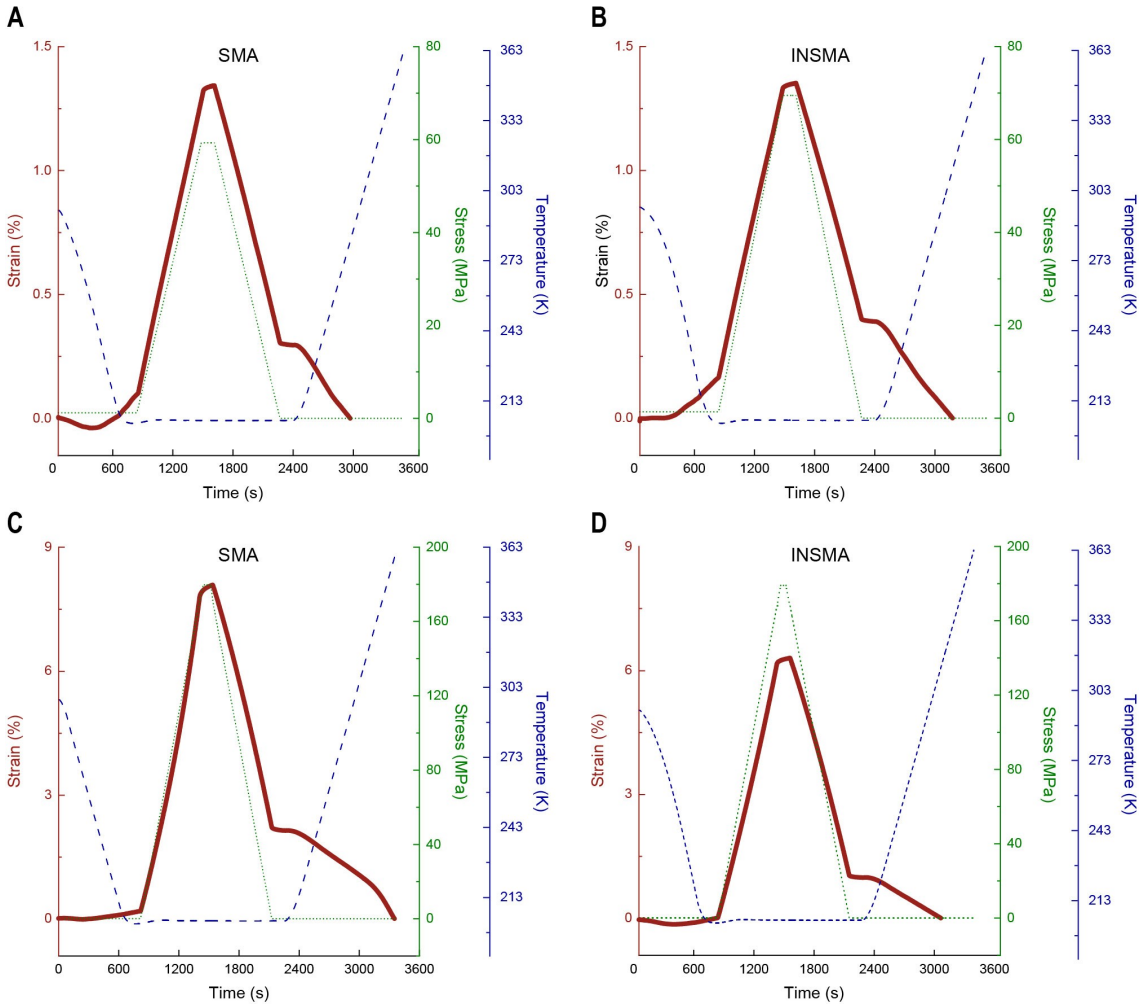

Figure S20. Thermomechanical shape memory curves for (**A** and **C**) SMA and (**B** and **D**) INSMA obtained from dynamic mechanical analysis (DMA) experiments.

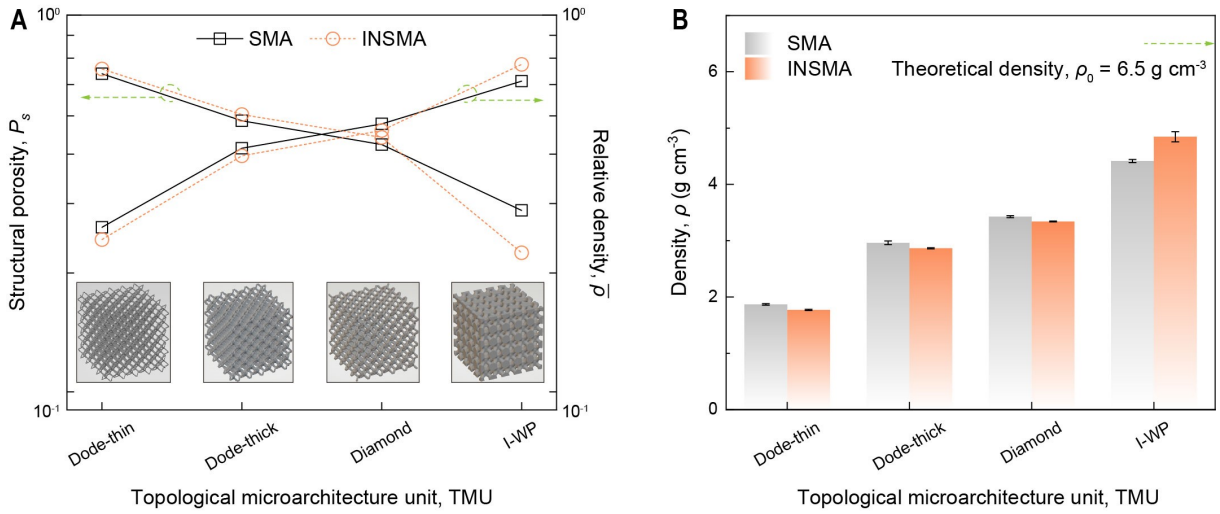

Figure S21. Plots of structural porosity and relative density of various shape-memory mechanical metamaterials (SMMMs). The error bar of each data point in (B) is the SD from the statistical average for three to six experimental samples.

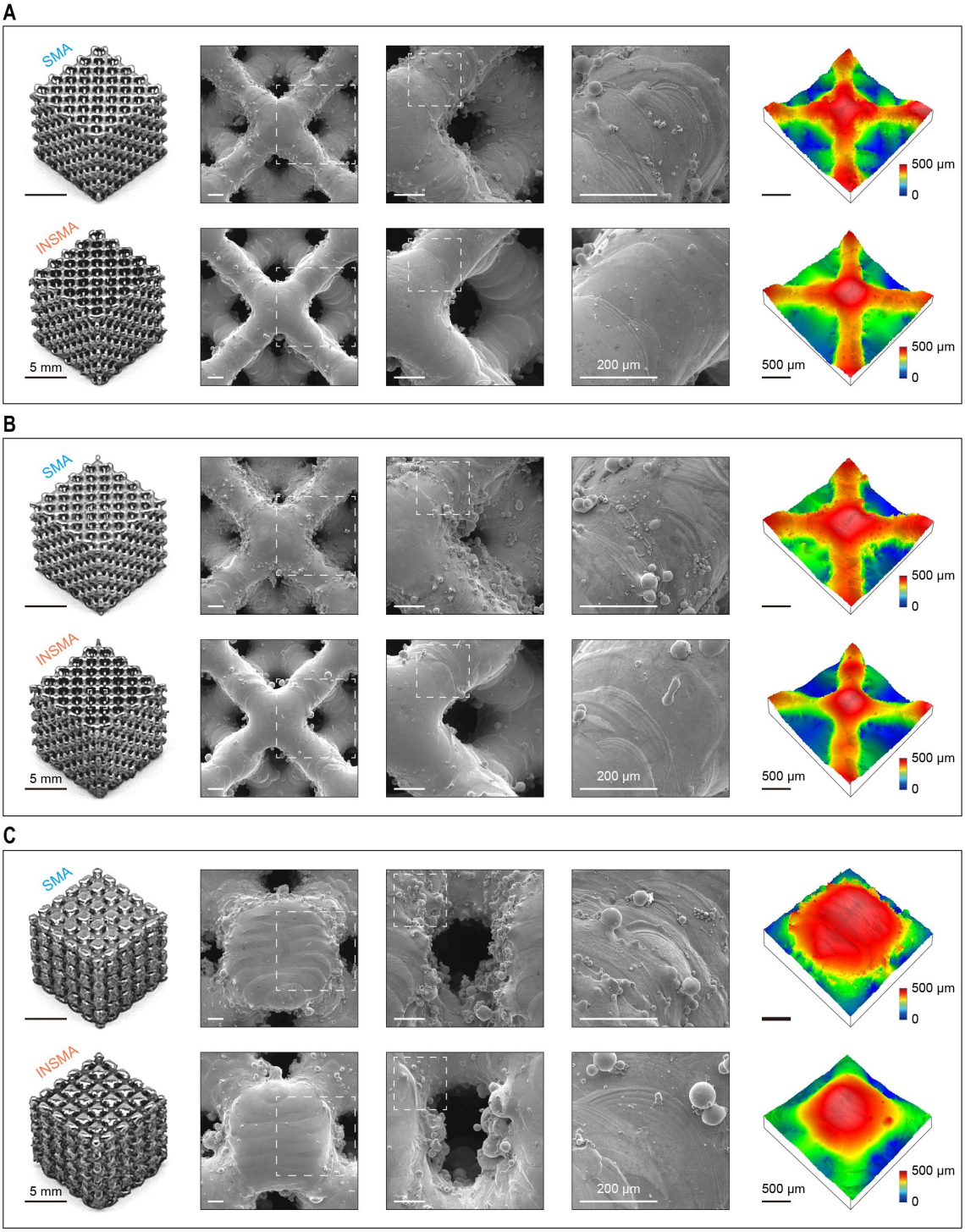

Figure S22. Surface topography of as-built SMMMs with different topological microarchitectures. (**A**) Dode-thick microlattice. (**B**) Diamond microlattice. (**C**) Schoen's I-graph–wrapped package (I-WP) microlattice.

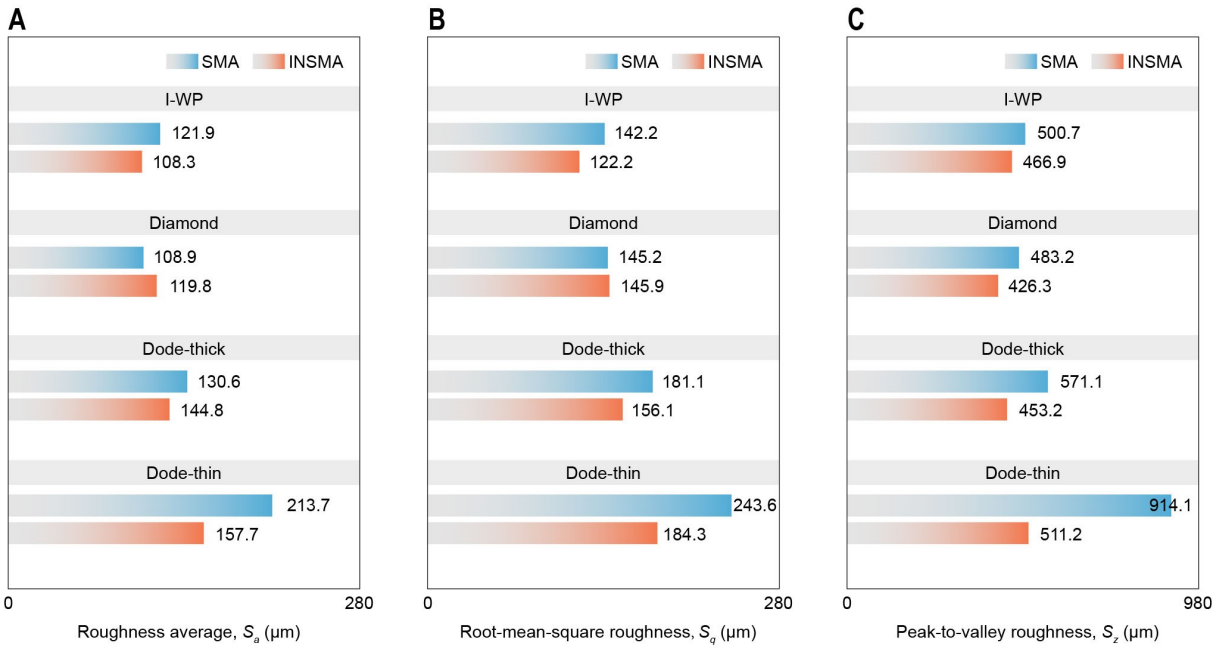

Figure S23. Quantitative results on the dimensional accuracy of as-built SMMMs. (**A** to **C**) The roughness average, root-mean-square roughness and peak-to-valley roughness (average maxima profile height) from 3D surface profile measurements.

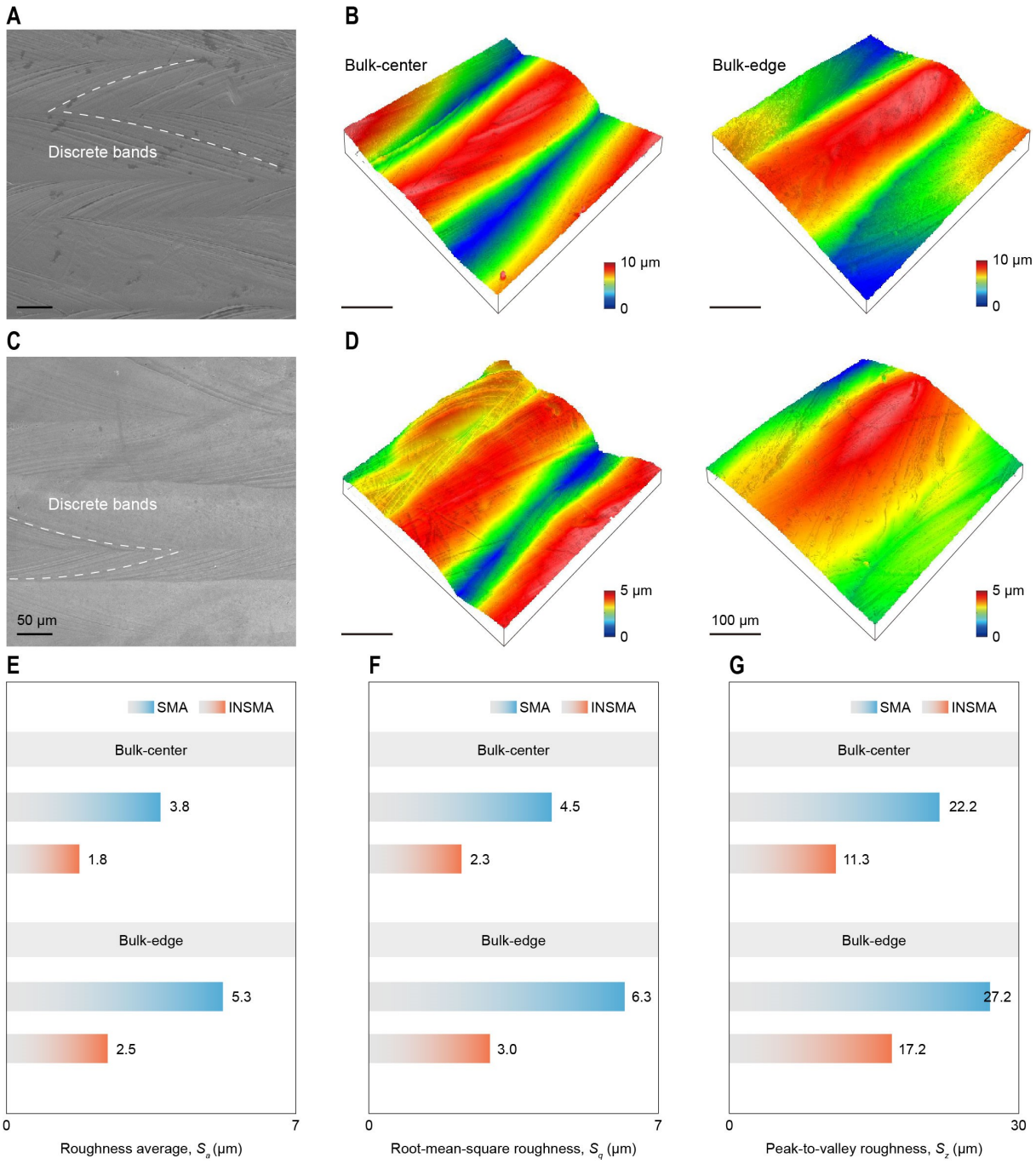

Figure S24. Surface topography of as-built dense bulk materials. SEM images and 3D surface topographies showing the multiple deposited traces of (**A** and **B**) SMA and (**C** and **D**) INSMA samples. (**E** to **G**) Quantitative results from 3D surface profile measurements.

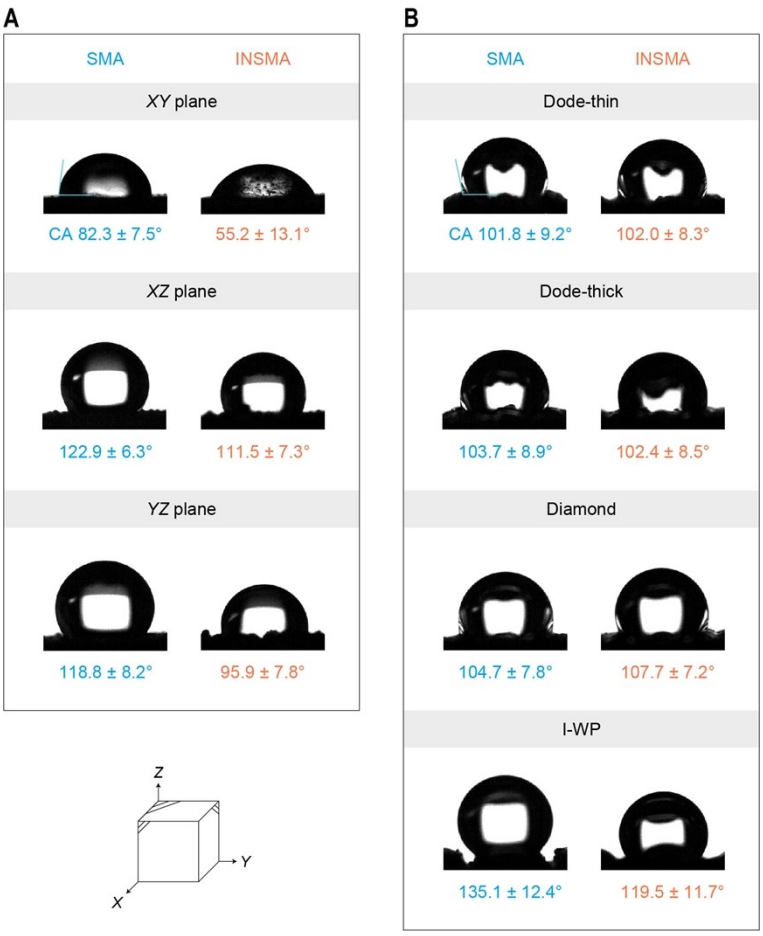

Figure S25. Contact angles of deionized water with the as-printed surfaces in air at room temperature. (**A**) Bulk materials. (**B**) Architected metamaterials.

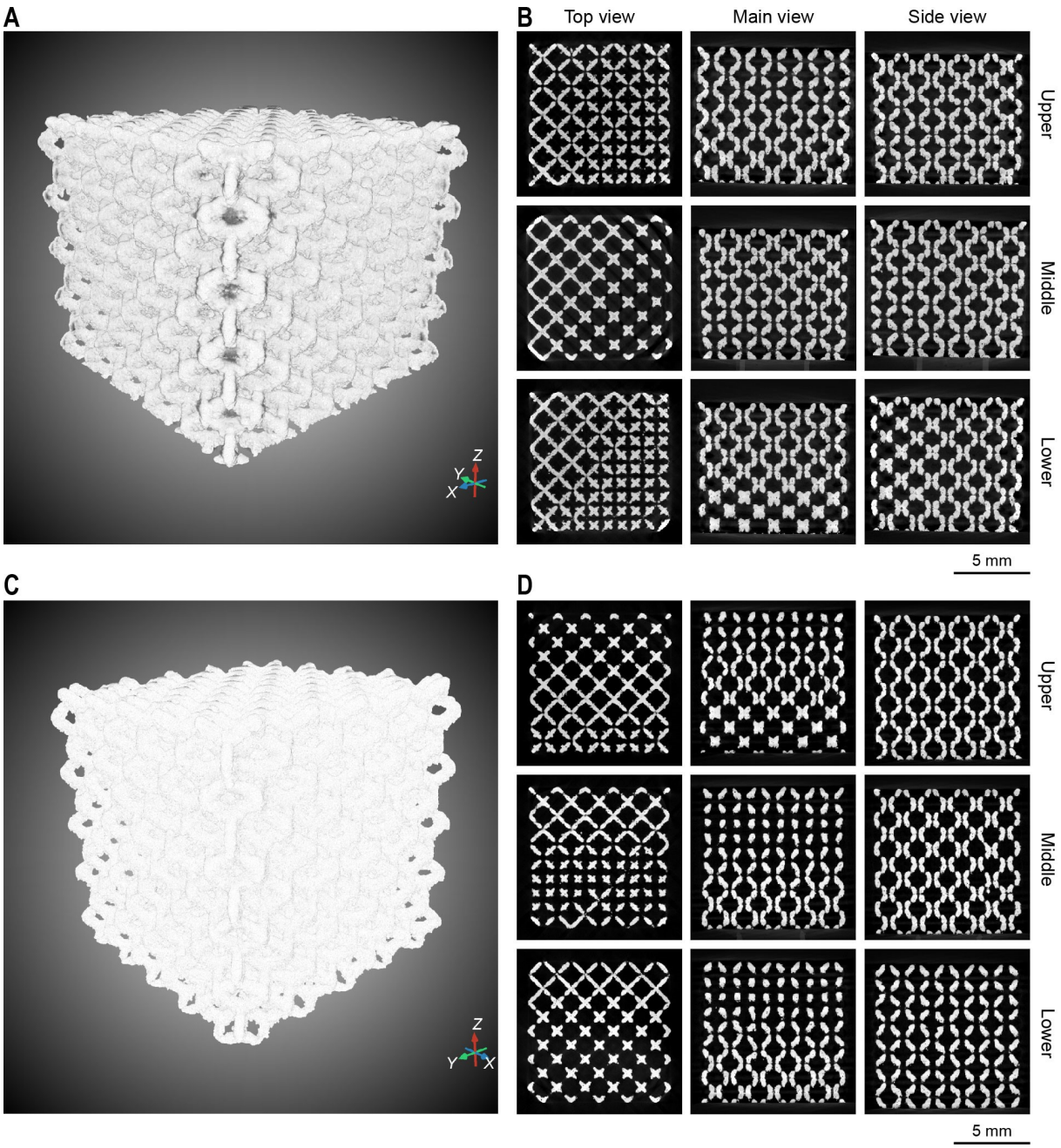

Figure S26. X-ray microfocus computed tomography (micro-CT) characterization of the SMMMs. 3D visualization images of (**A**) SMA and (**C**) INSMA samples with dode-thin microlattices. (**B** and **D**) Corresponding 2D projections of selected upper, middle, and lower positions in the *XY*, *XZ*, and *YZ* planes.

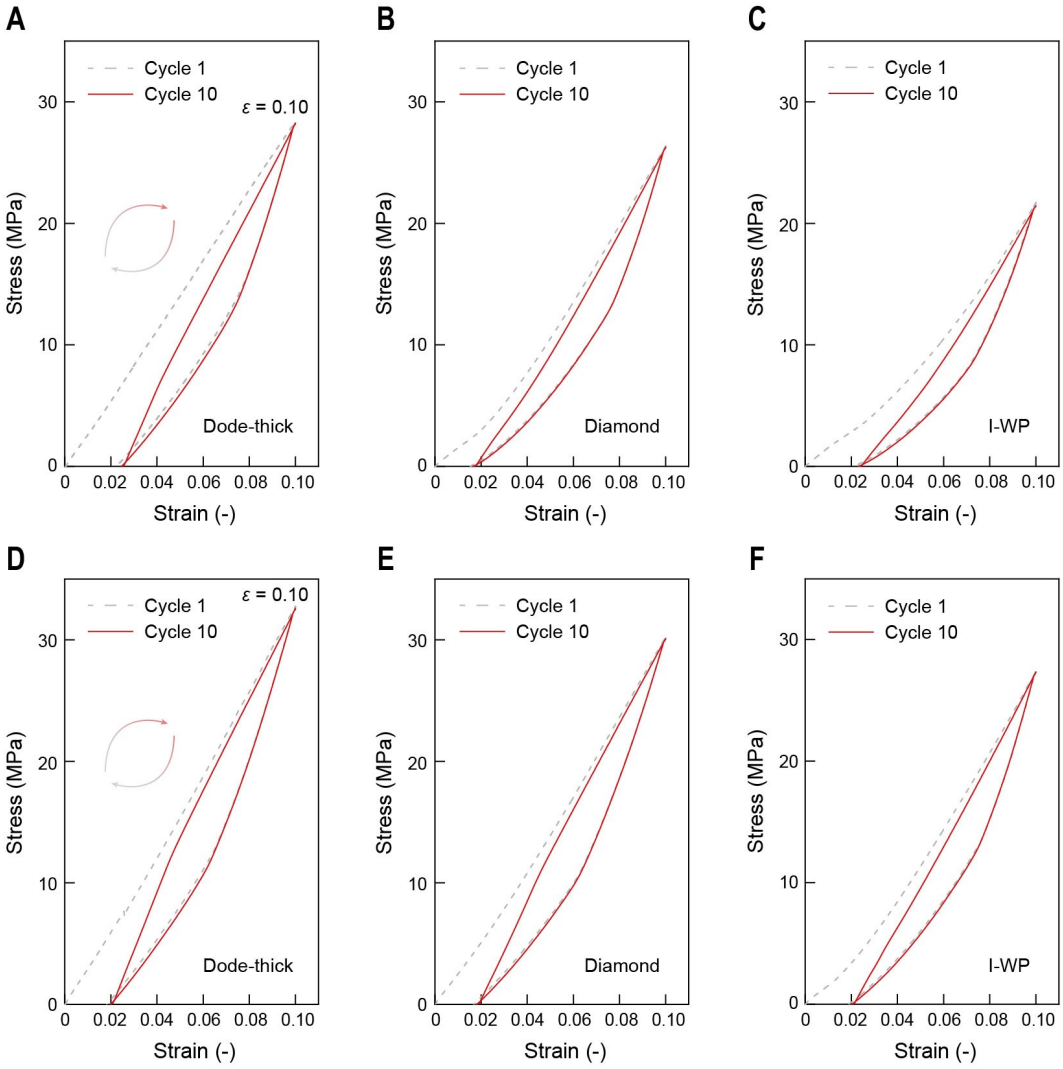

Figure S27. Cyclic stress-strain curves of as-fabricated SMMMs. (**A** to **C**) pristine SMA and (**D** to **F**) INSMA samples were subjected to 10 cycles of compression training under constant strain level of 10%.

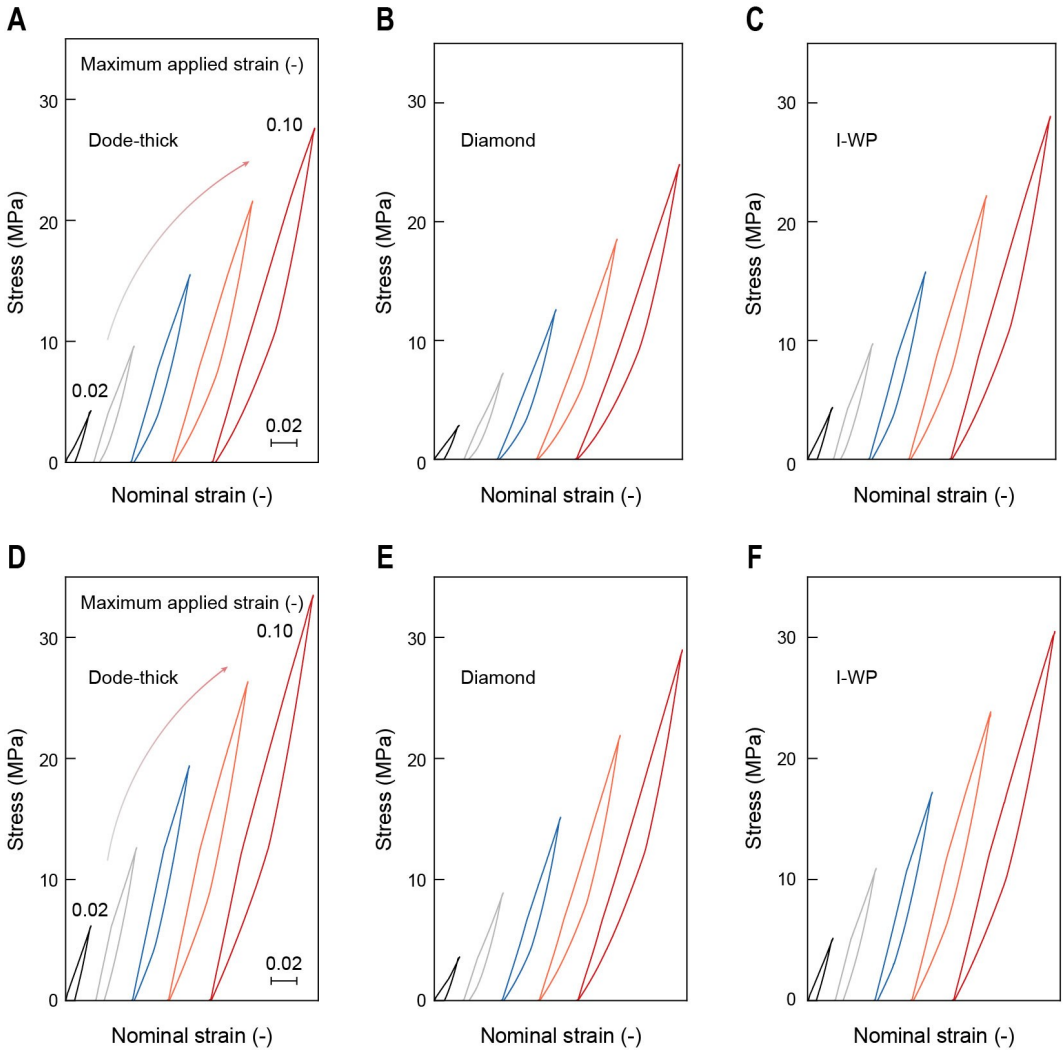

Figure S28. Gradient stress-strain curves of as-fabricated SMMMs. (**A** to **C**) pristine SMA and (**D** to **F**) INSMA samples were subjected to compression training under different maximum applied strain levels ranged from 2% to 10%.

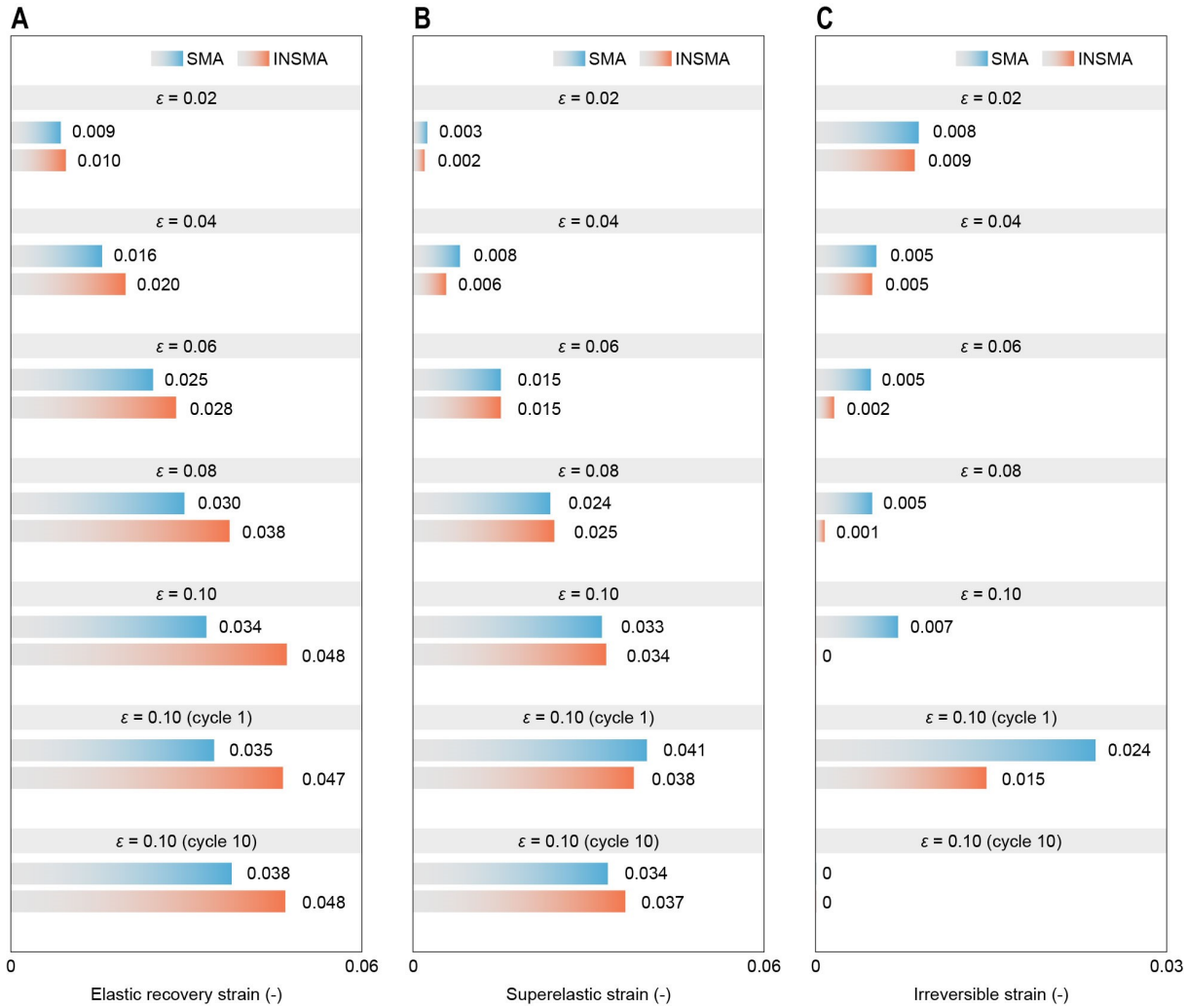

Figure S29. Variations of characteristic strains with loading cycles/gradients during the cyclic/gradient loading-unloading process. Quantitative results of mean elastic recovery strain (**A**) (ε_{el}), superelastic strain (**B**) (ε_{se}), and irreversible strain (**C**) (ε_{ir}) for dode-thin microlattice architected SMMMs.

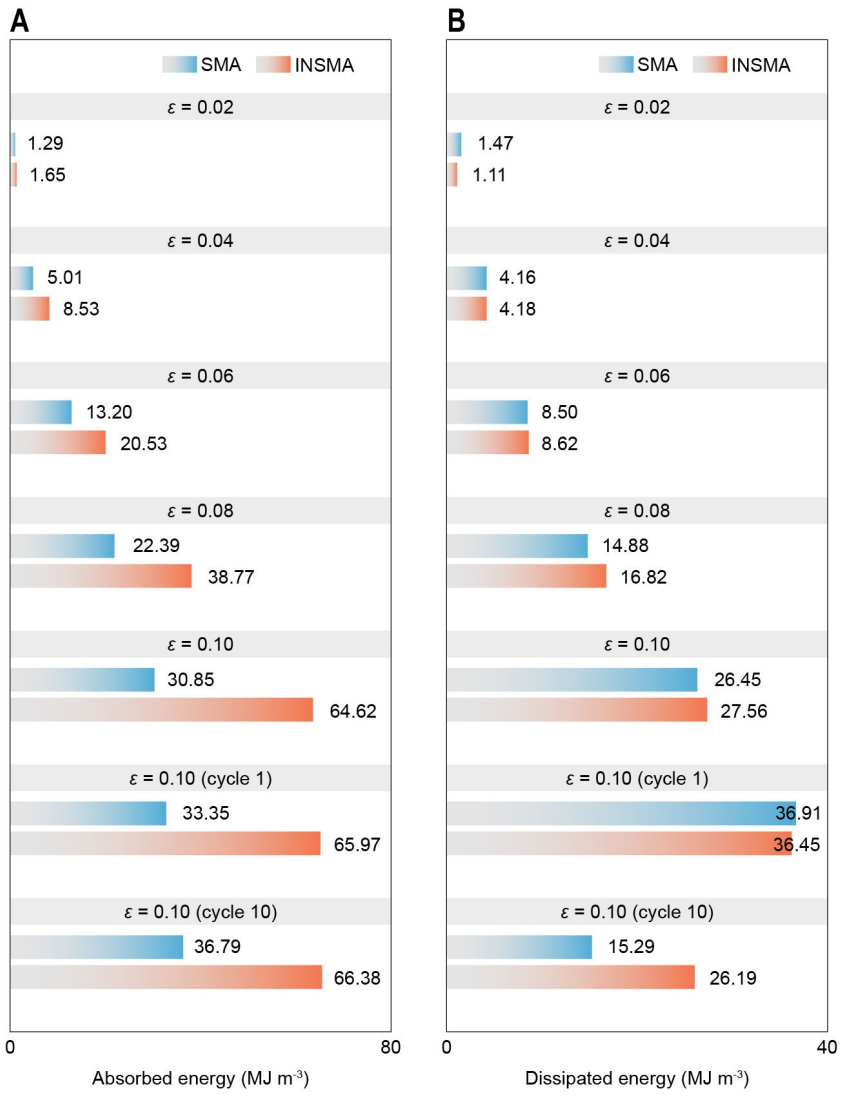

Figure S30. Variations of characteristic energies with loading cycles/gradients during the cyclic/gradient loading-unloading process. Quantitative results of mean absorbed energy (**A**) ($E_{absorbed}$) and dissipated energy (**B**) ($E_{dissipated}$) for dode-thin microlattice architected SMMMs.

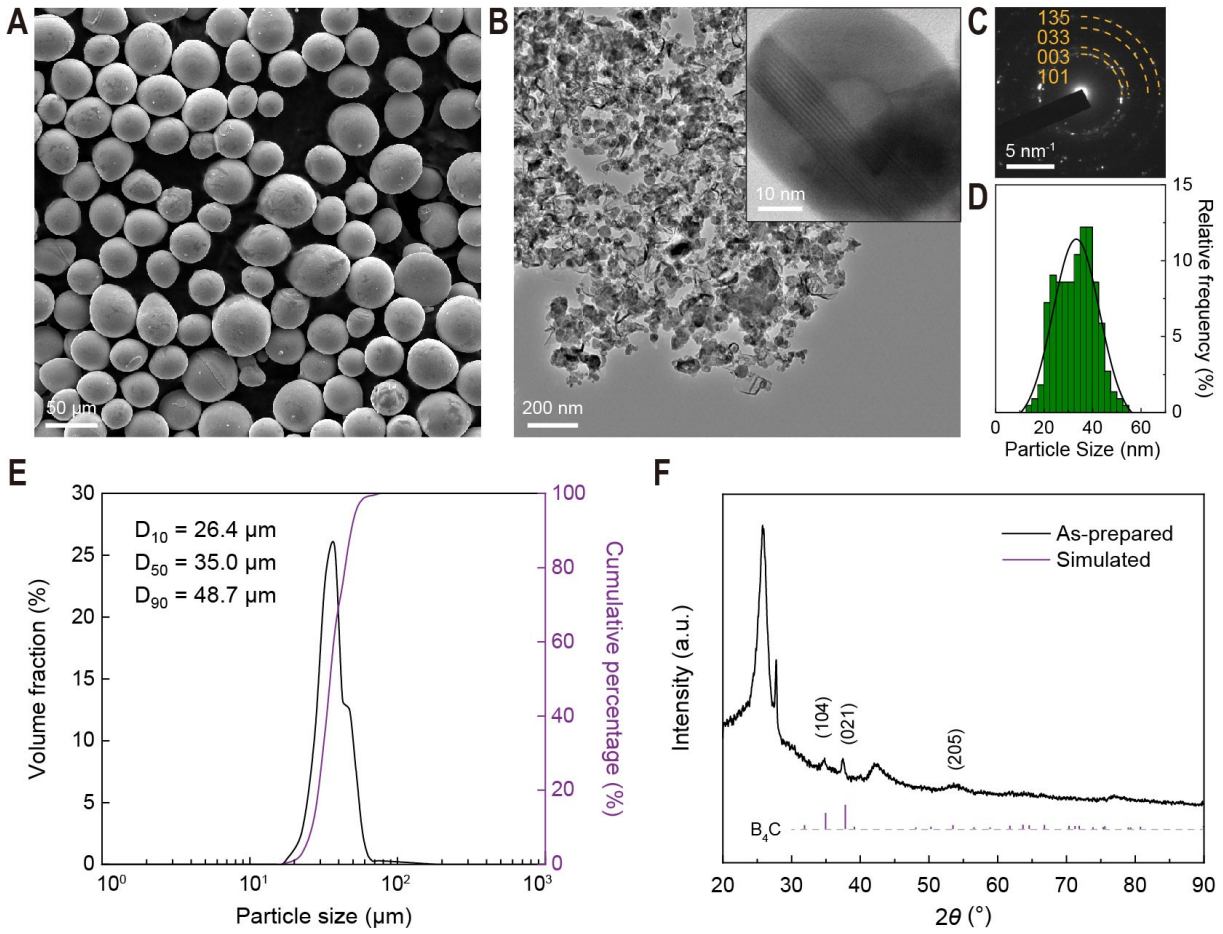

Figure S31. Powder feedstocks. (**A** and **E**) SEM micrograph and particle size distribution curve of the $Ni_{50.8}Ti_{49.2}$ SMA micropowder. (**B** and **C**) TEM images and corresponding selected area electron diffraction (SAED) pattern of the B_4C nanoprecursors (nano-B_4C) as the in-situ reactant. (**D**) The particle size distribution plot of the nano-B_4C measured from the TEM image in (B). (**F**) The PXRD pattern of the nano-B_4C.

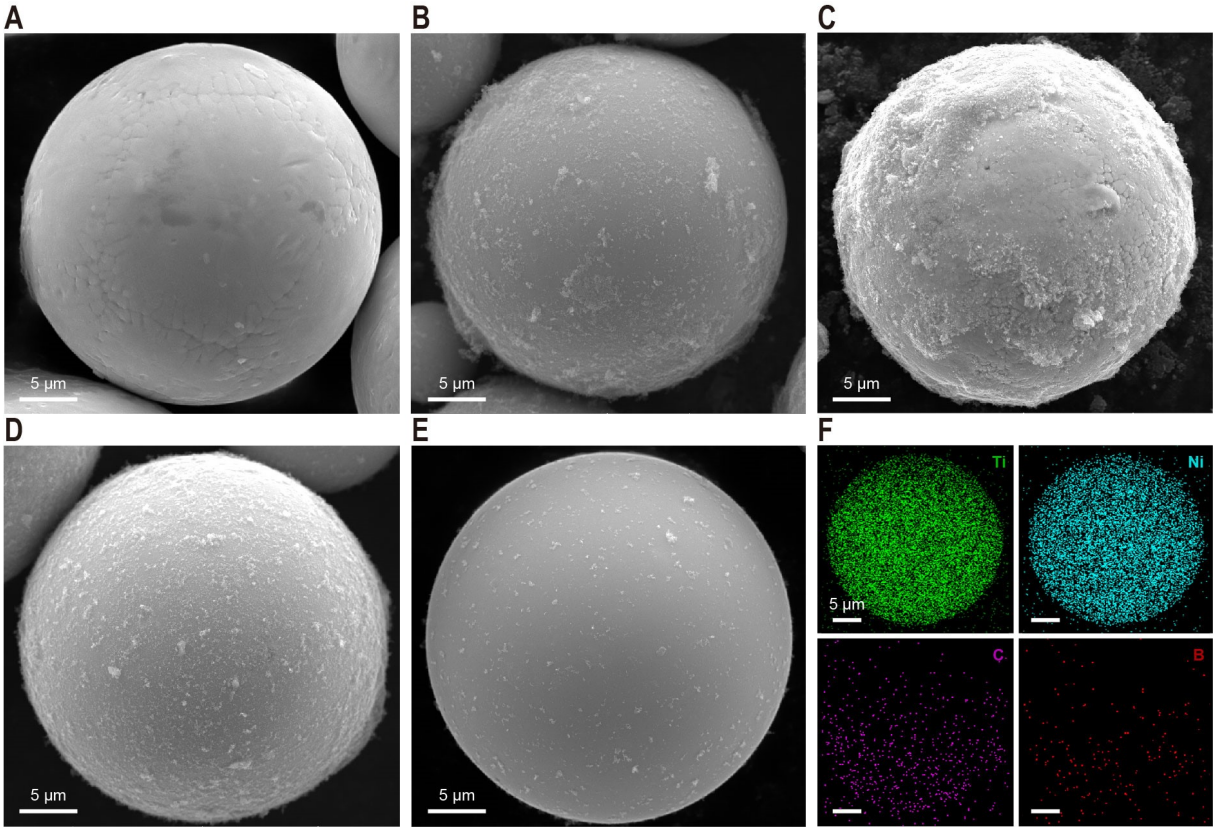

Figure S32. Nanoreactants assembly on additive SMA powders. (**A**) Pristine. (**B**) Directly mechanically mixed. (**C**) Hydrostatically adsorbed. (**D**) Hydrostatic adsorption synergized with low-energy mechanical mixing. (**E**) SMA powder with spherical morphology and refined nanoreactant loading. (**F**) SEM-EDS maps showing the elemental distribution in (E).

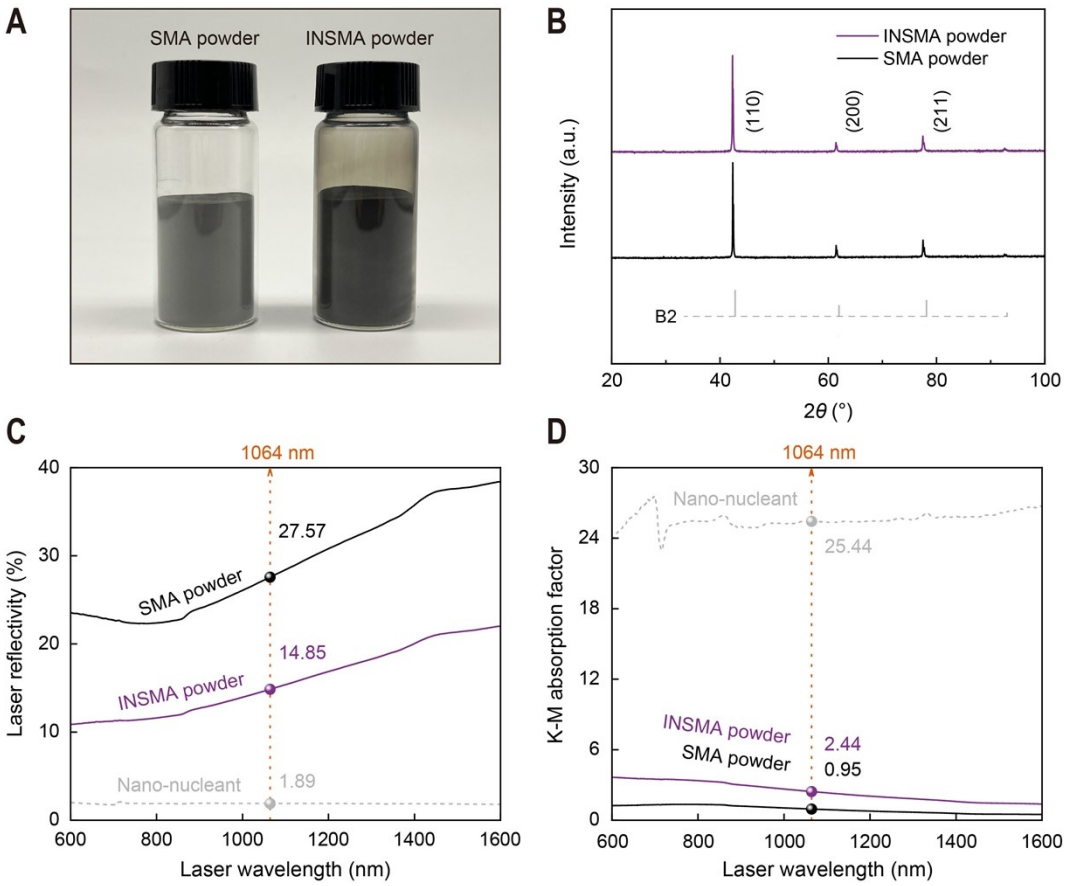

Figure S33. Physical characteristics of the SMA powder functionalized with nano-B_4C. (**A**) The optical image and (**B**) PXRD patterns of the pristine SMA and INSMA powders. (**C**) The laser reflectivity and (**D**) K-M absorption factor of the various powder materials. The laser absorptivity of INSMA powder has been significantly increased by introducing nanoreactants with ultra-low laser reflectivity.

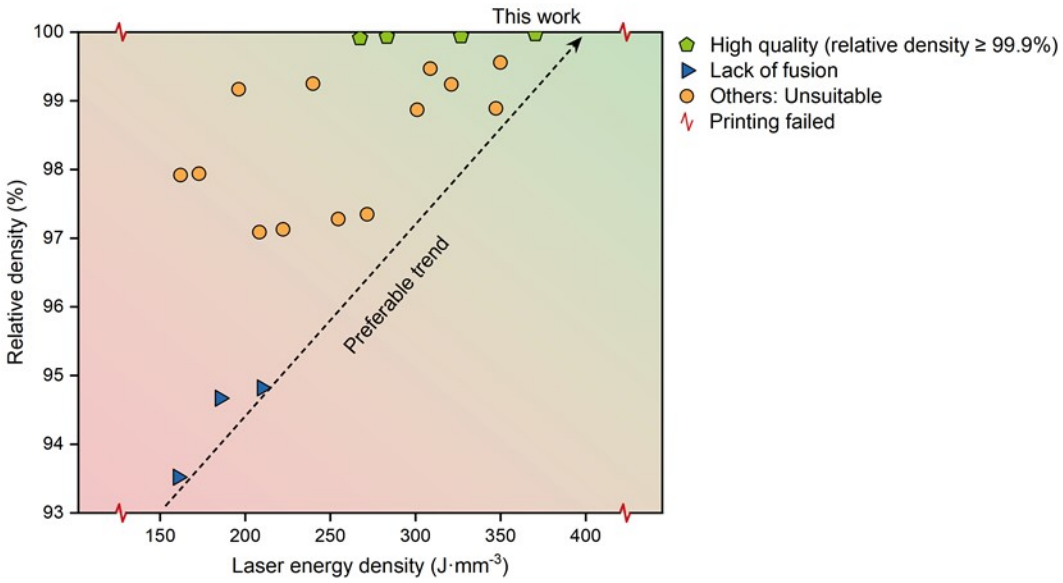

Figure S34. The comparison of relative density ($\bar{\rho}$) and laser energy density (E) obtained from various combinations of laser power (P) and laser scanning speed (v).

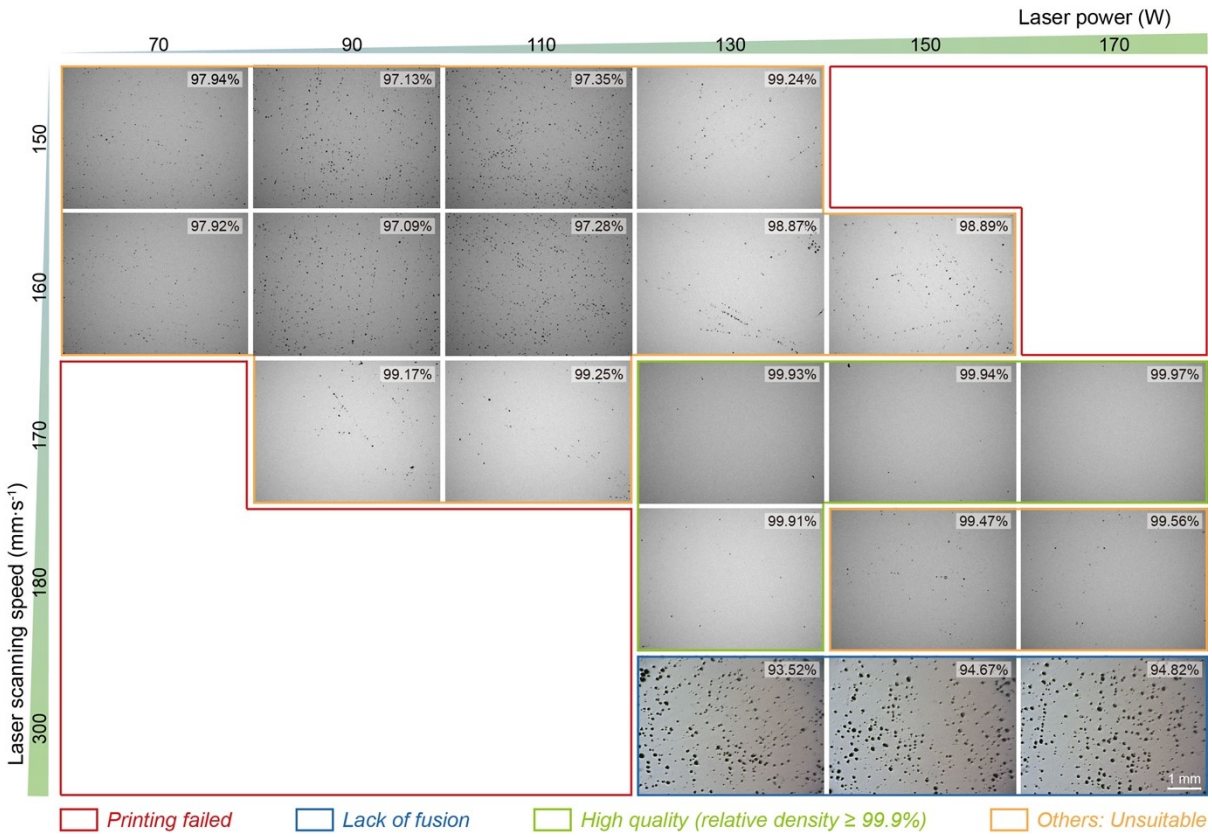

Figure S35. Optical micrographs of the metallographs form the longitudinal section (*YZ* plane) of the INSMA samples printed at different laser powers (P) and laser scanning speeds (v). Inserted in the upper right corner are the corresponding relative density ($\bar{\rho}$) values for each condition.

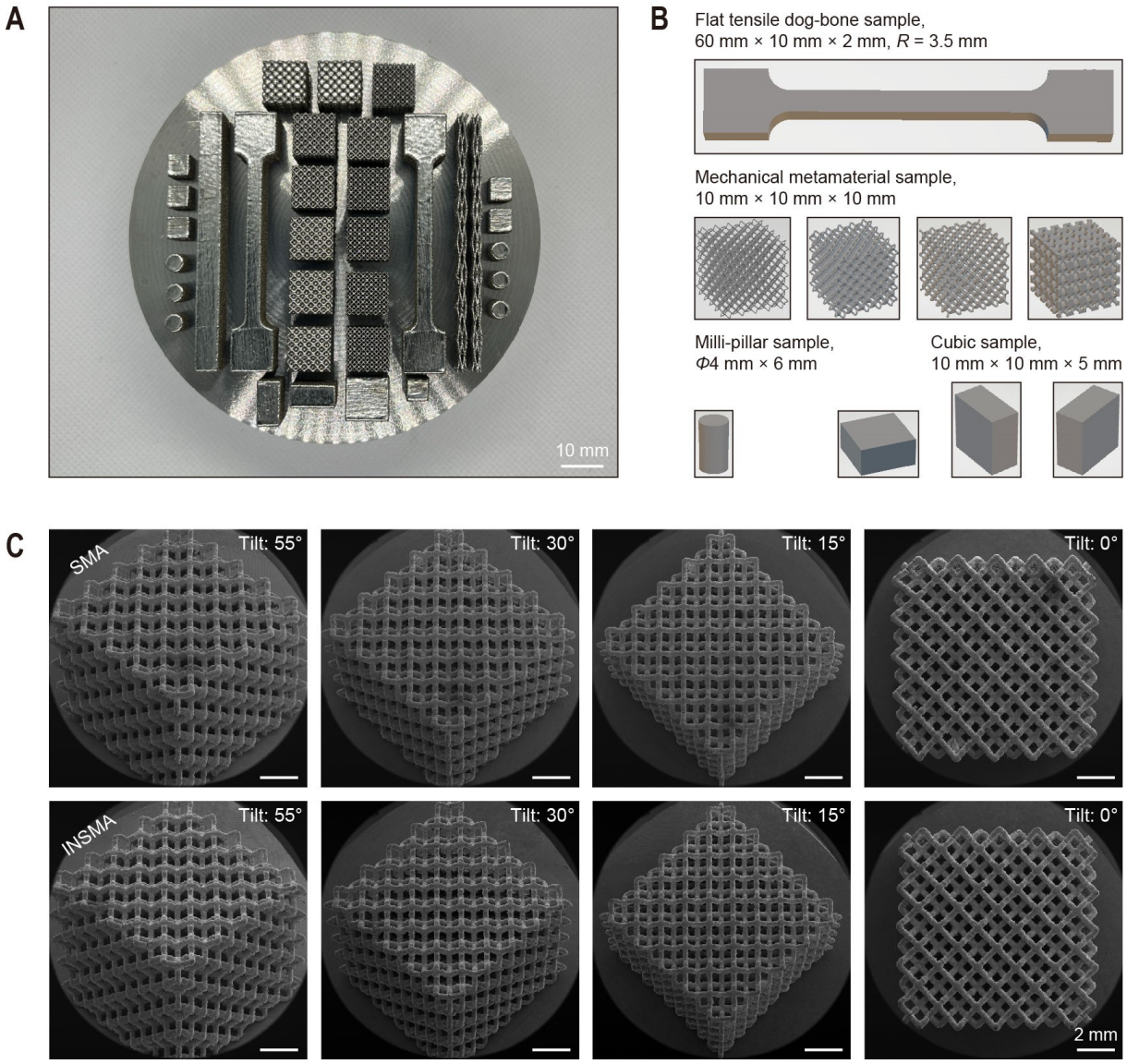

Figure S36. LPBF-AM as-printed INSMA samples for mechanical testing and microstructure characterization. (**A**) The macroscopic image of constructed parts. (**B**) Schematics of geometric dimensions of the flat tensile dog-bone and compression specimens used in this study. (**C**) SEM images of as-printed SMA and INSMA metamaterials at different tilting angles.

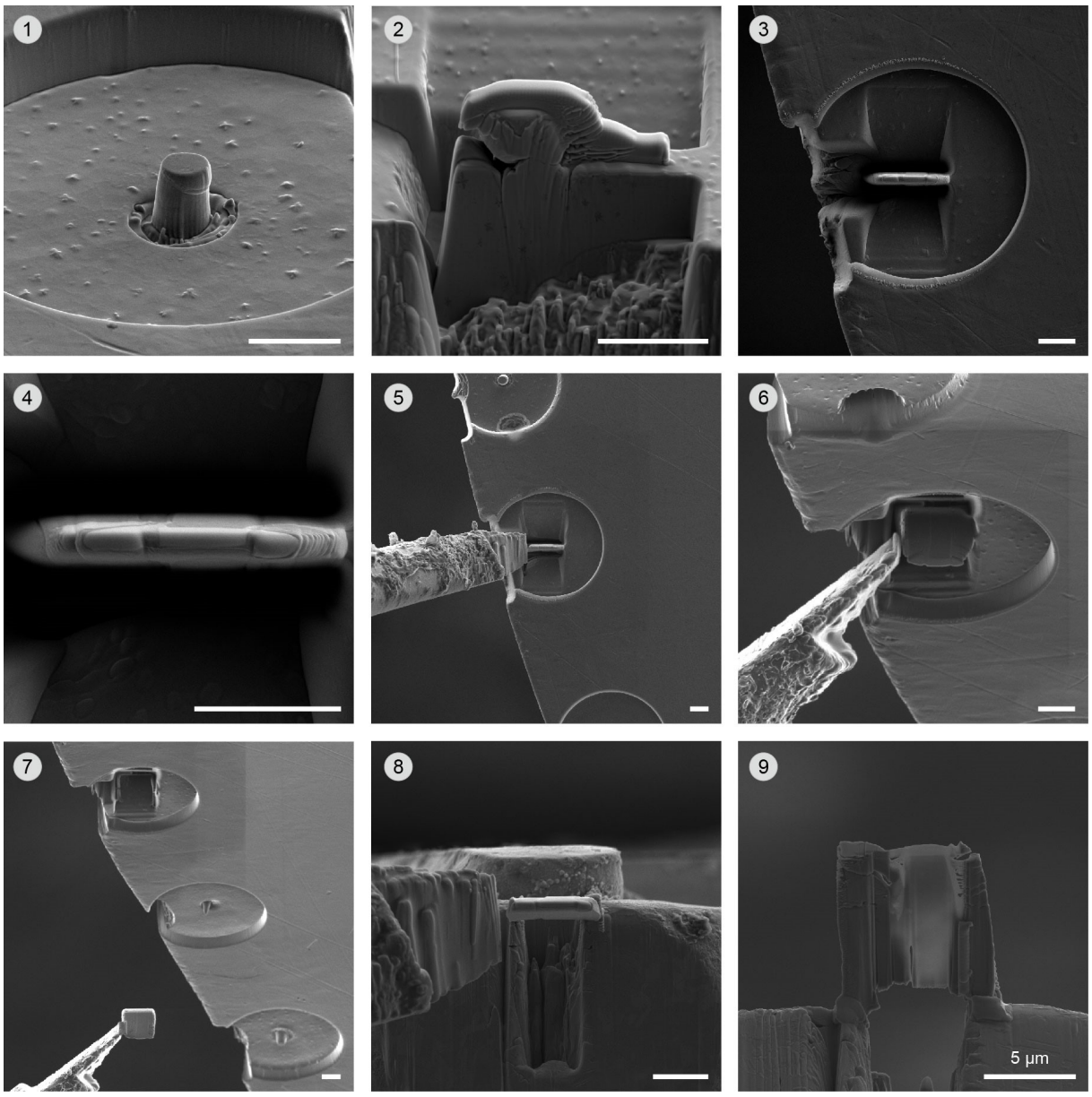

Figure S37. Site-specific FIB sampling procedures for the postmortem microstructure characterization of the micropillar after compression.

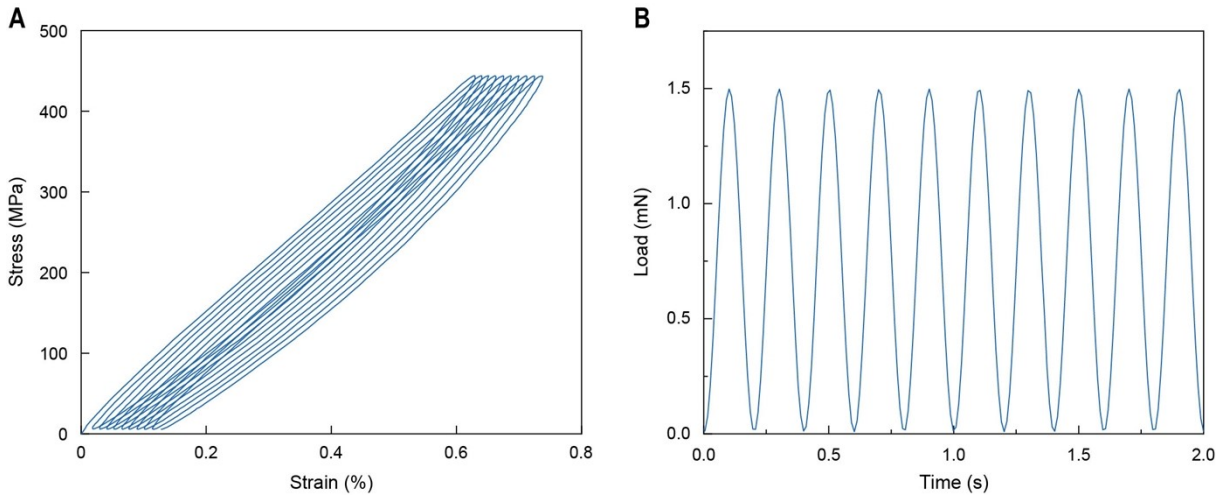

Figure S38. Cyclic loads used for the in-situ microfatigue tests. (**A** and **B**) 5 Hz load applied to obtain accurate load-displacement (*h*-*P*) curves. The chosen frequency is consistent with prior microscale fatigue report (*3*) and ensures valid comparison between pristine SMA and INSMA under identical conditions.

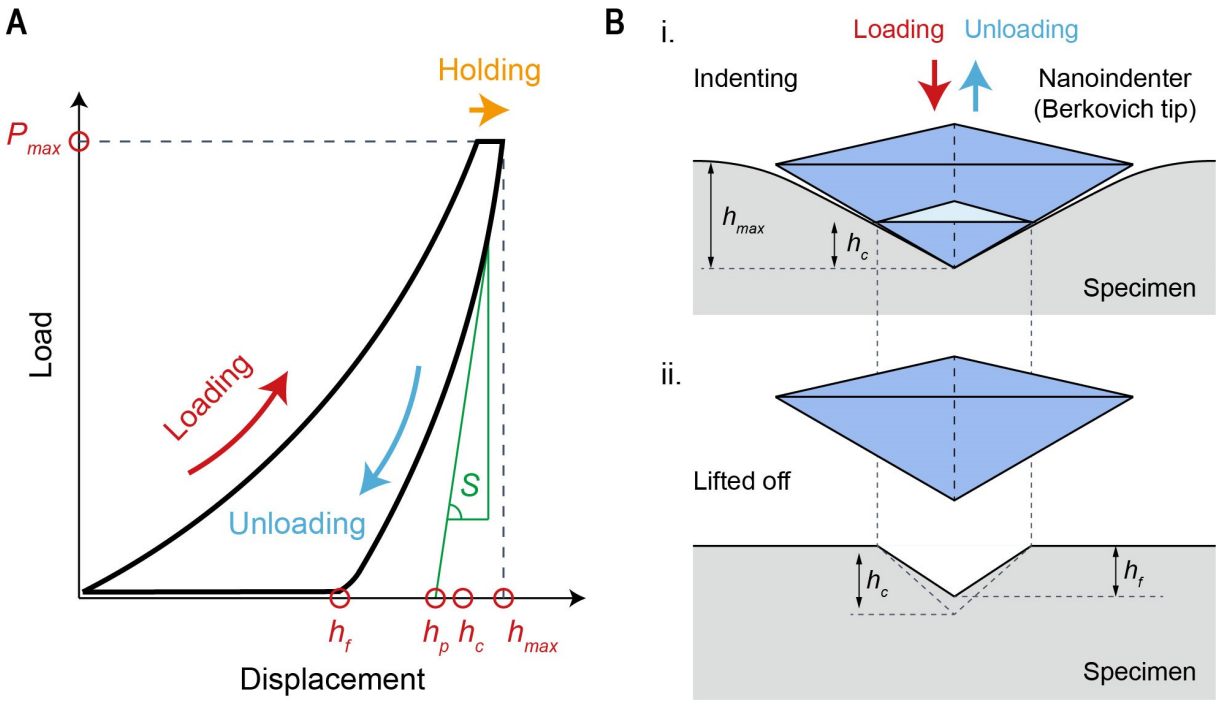

Figure S39. Principles of nanoindentation test.[S12] (**A**) A representative indentation load-displacement (*h*-*P*) curve and (**B**) the corresponding nanoindentation process: (i) Indentation process. (ii) After the indenter is lifted off, the specimen is partially deformed plastically.

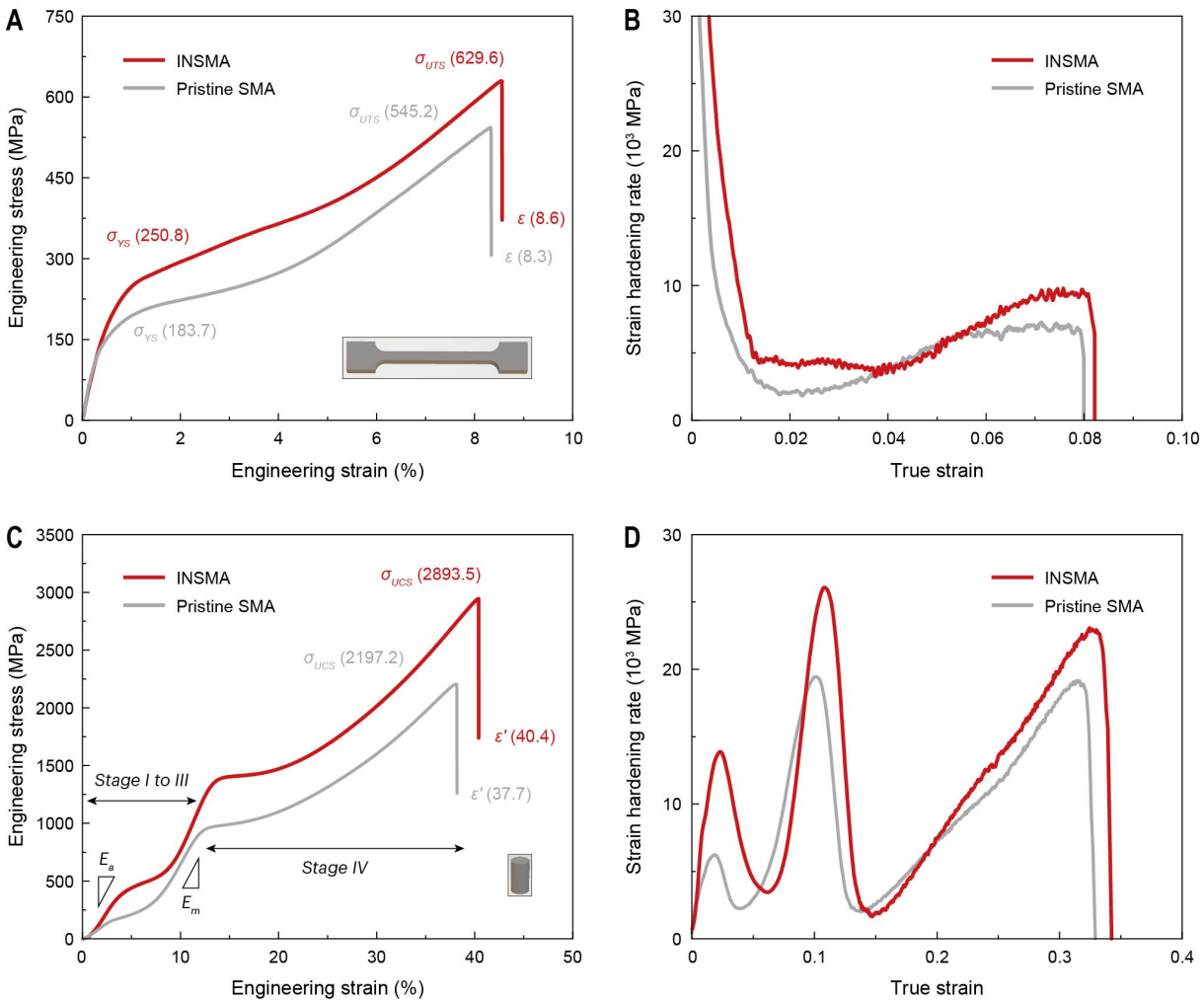

Figure S40. Mechanical properties of the pristine SMA and INSMA macroscopic bulk materials. (**A**) Uniaxial tensile stress-strain curves at ambient temperature. σ_{UTS}, ultimate tensile strength; σ_{YS}, yield strength; ε, elongation-to-failure. Note: σ_{YS} refers to the critical stress (σ_{Ms}) at the start of induced martensitic transformation. (**B**) Strain hardening rate-true strain curves in tension. (**C**) Uniaxial compressive stress-strain curves at ambient temperature. σ_{UCS}, ultimate compressive strength; ε', compressive fracture strain; E_a, Elastic modulus of the B2 austenitic state; E_m, Elastic modulus of the B19' martensitic state. (**D**) Strain hardening rate-true strain curves in compression.

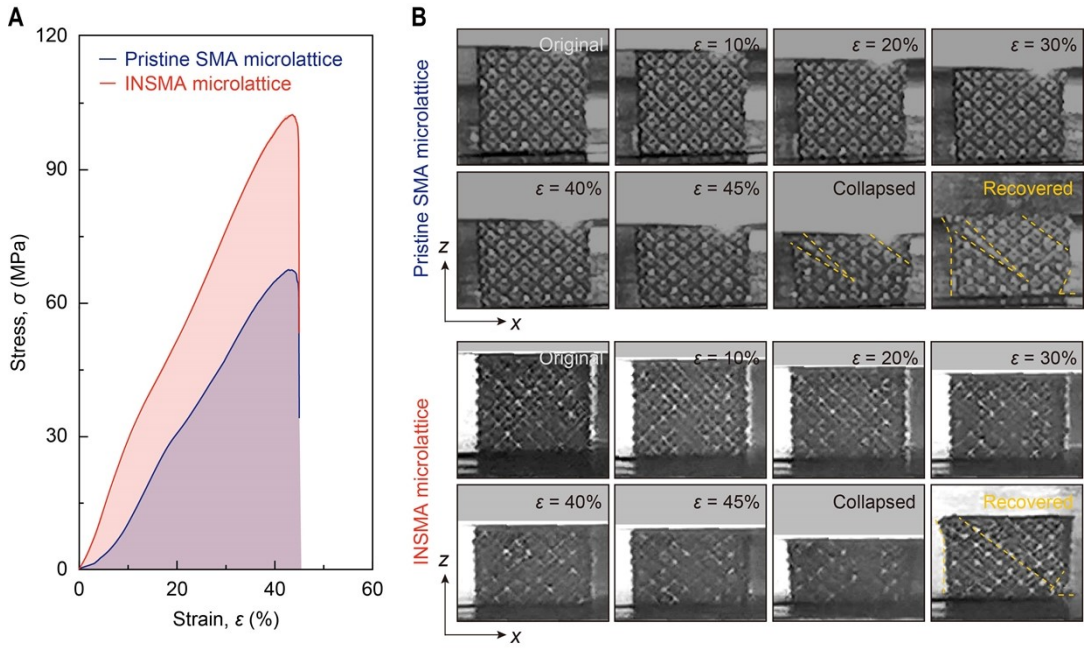

Figure S41. Mechanical properties of microlattice metamaterials. (**A**) Representative uniaxial compressive engineering stress-strain curves at ambient temperature for pristine SMA and INSMA. (**B**) The corresponding deformation images recorded for the two microlattice metamaterials at different strain stages.

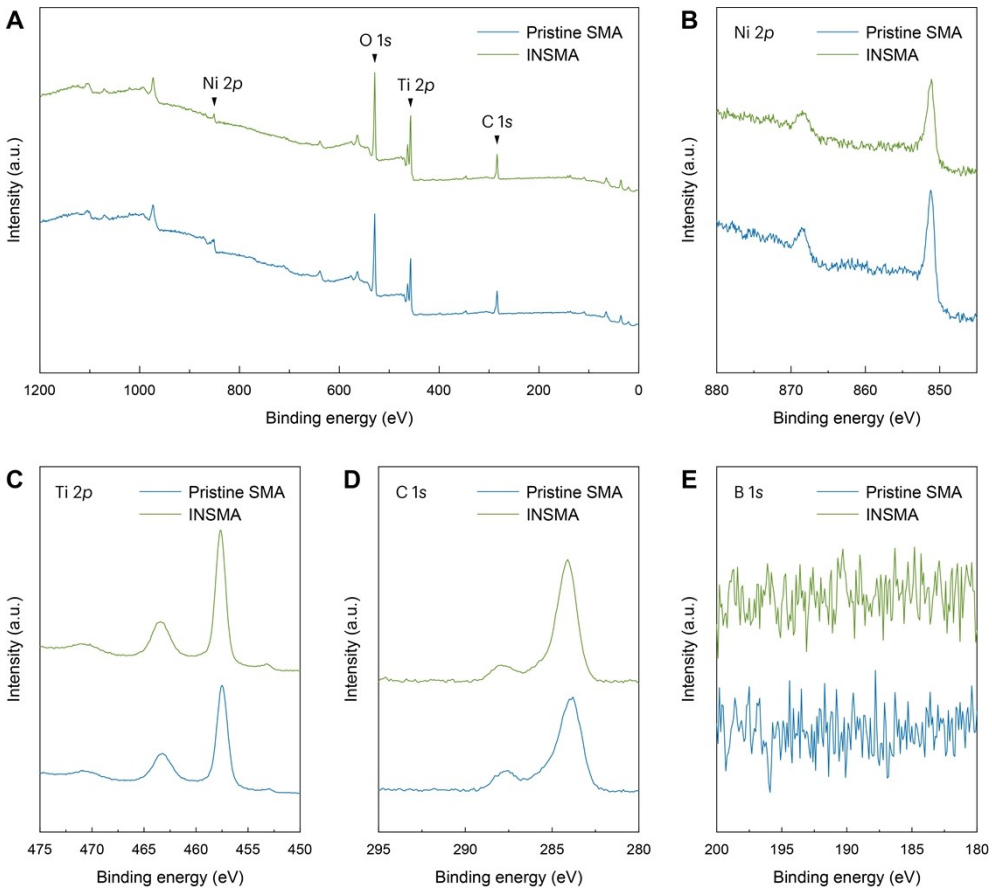

Figure S42. XPS analysis of the surfaces of pristine SMA and INSMA samples. (**A**) Survey XPS spectrum. (**B** to **E**) High-resolution XPS spectra of Ni 2*p*, Ti 2*p*, C 1*s*, and B 1*s*, respectively.

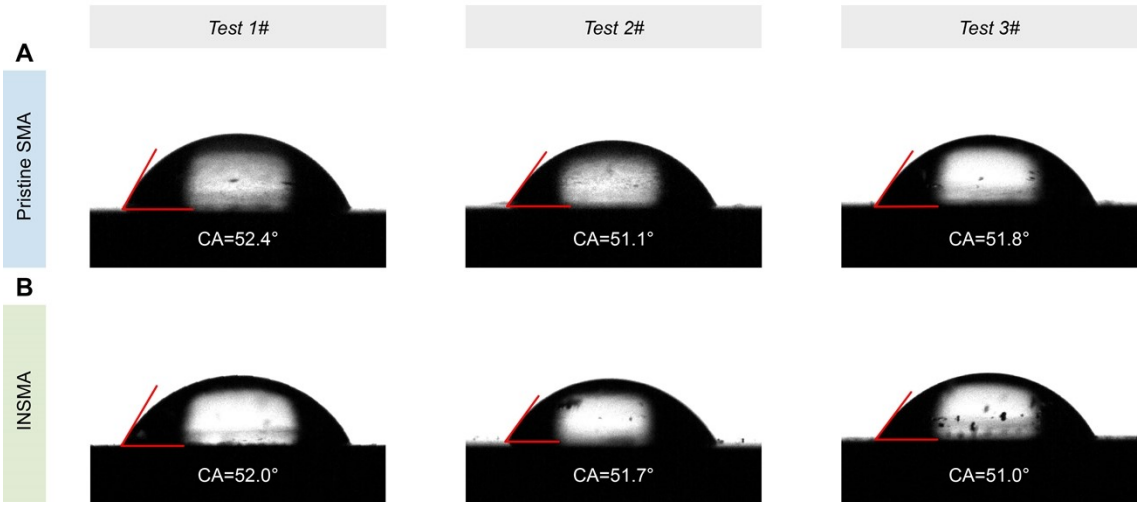

Figure S43. Contact angle measurements of deionized water on polished, smooth surfaces. (**A**) Pristine SMA sample. (**B**) INSMA sample.

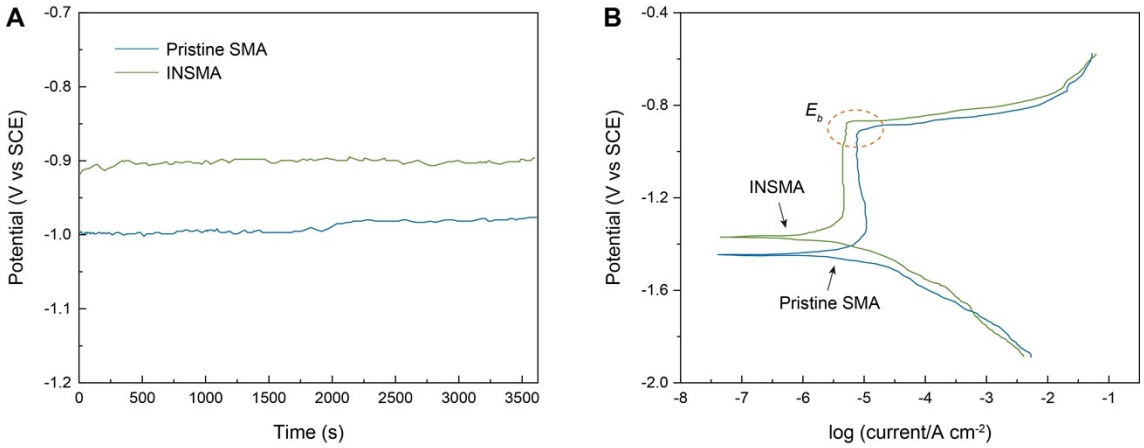

Figure S44. Electrochemical measurement results of as-built pristine SMA and INSMA samples in 3.5 wt.% NaCl solution at room temperature. (**A**) Open circuit potential (OCP) curves and (**B**) potentiodynamic polarization curves.

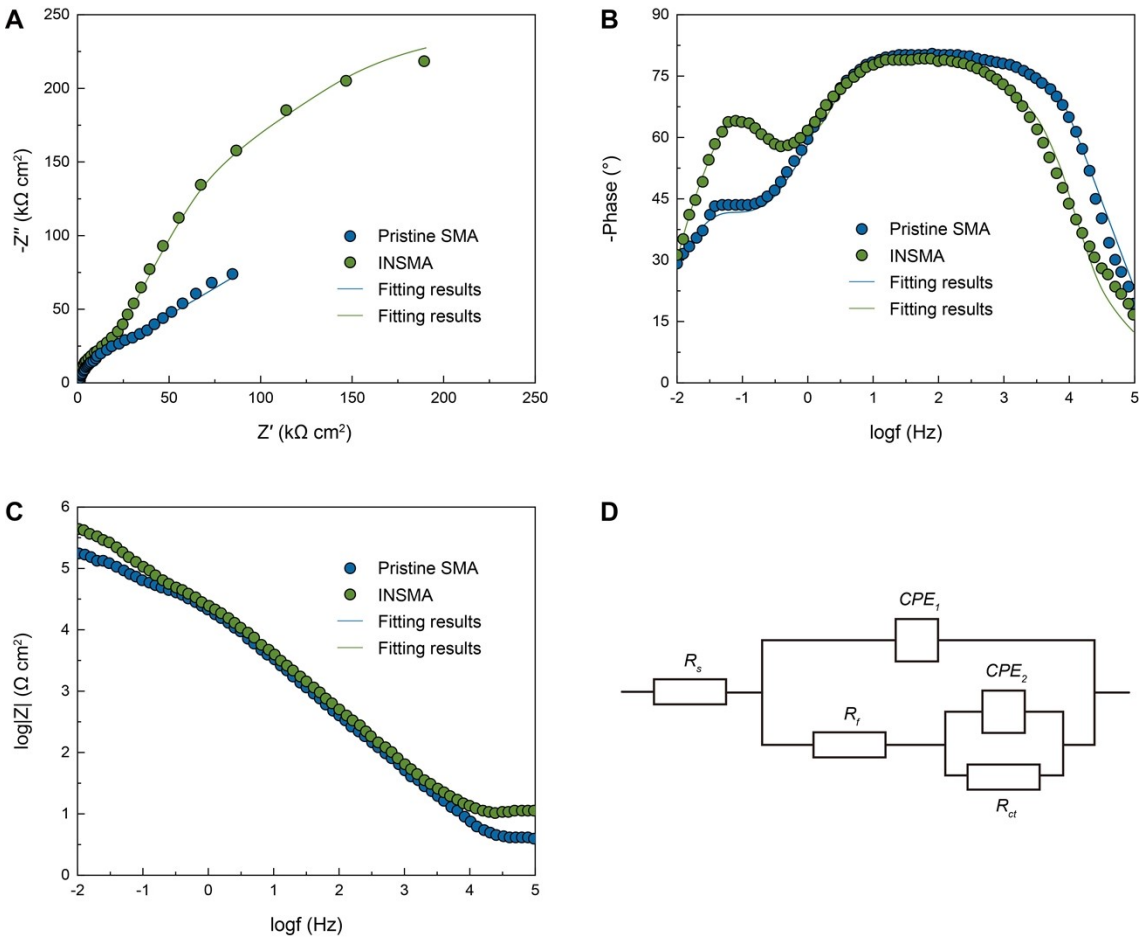

Figure S45. Electrochemical impedance spectroscopy (EIS) results of as-built pristine SMA and INSMA samples in 3.5 wt.% NaCl solution at room temperature. (**A**) Nyquist plots, (**B** and **C**) Bode plots, and (**D**) equivalent circuit model.

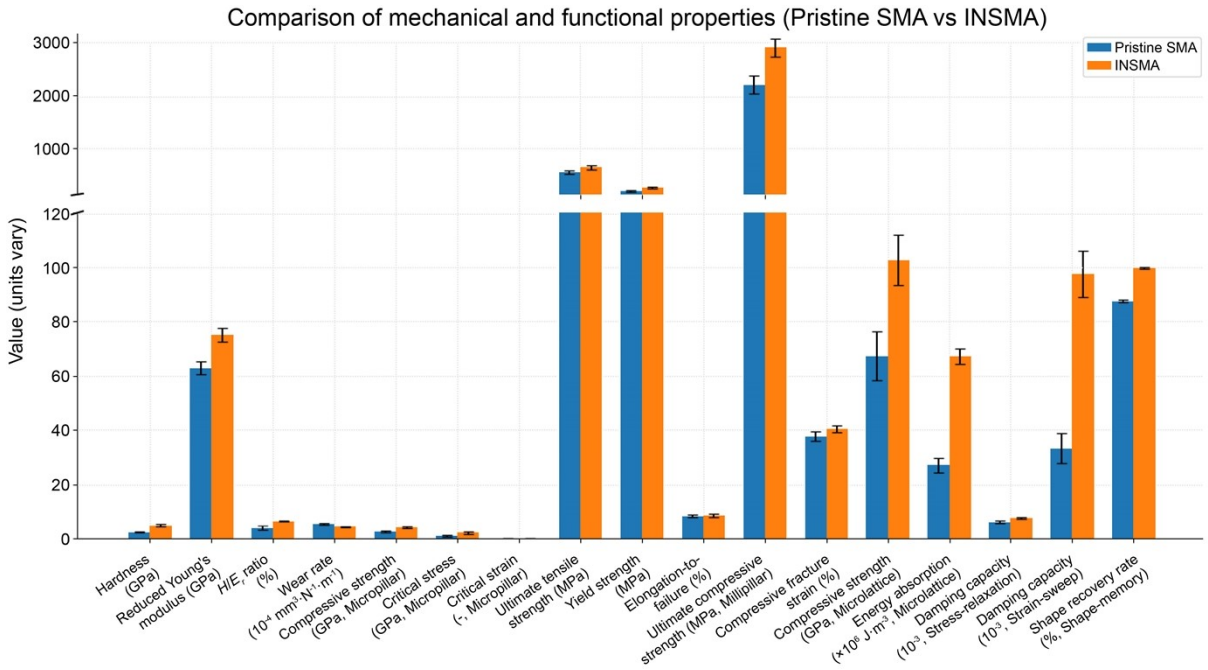

Figure S46. Statistical comparison of the key mechanical and functional properties of pristine SMA and INSMA samples, including hardness, reduced Young's modulus, H/E_r ratio, wear rate, yield strength, compressive and tensile strengths, critical stress and strain, elongation-to-failure, fracture strain, compressive strength of microlattices, energy absorption per unit volume, damping capacity, and shape recovery rate. The bar plots show mean values with error bars representing standard deviations, consistent with the data summarized in Table S10.

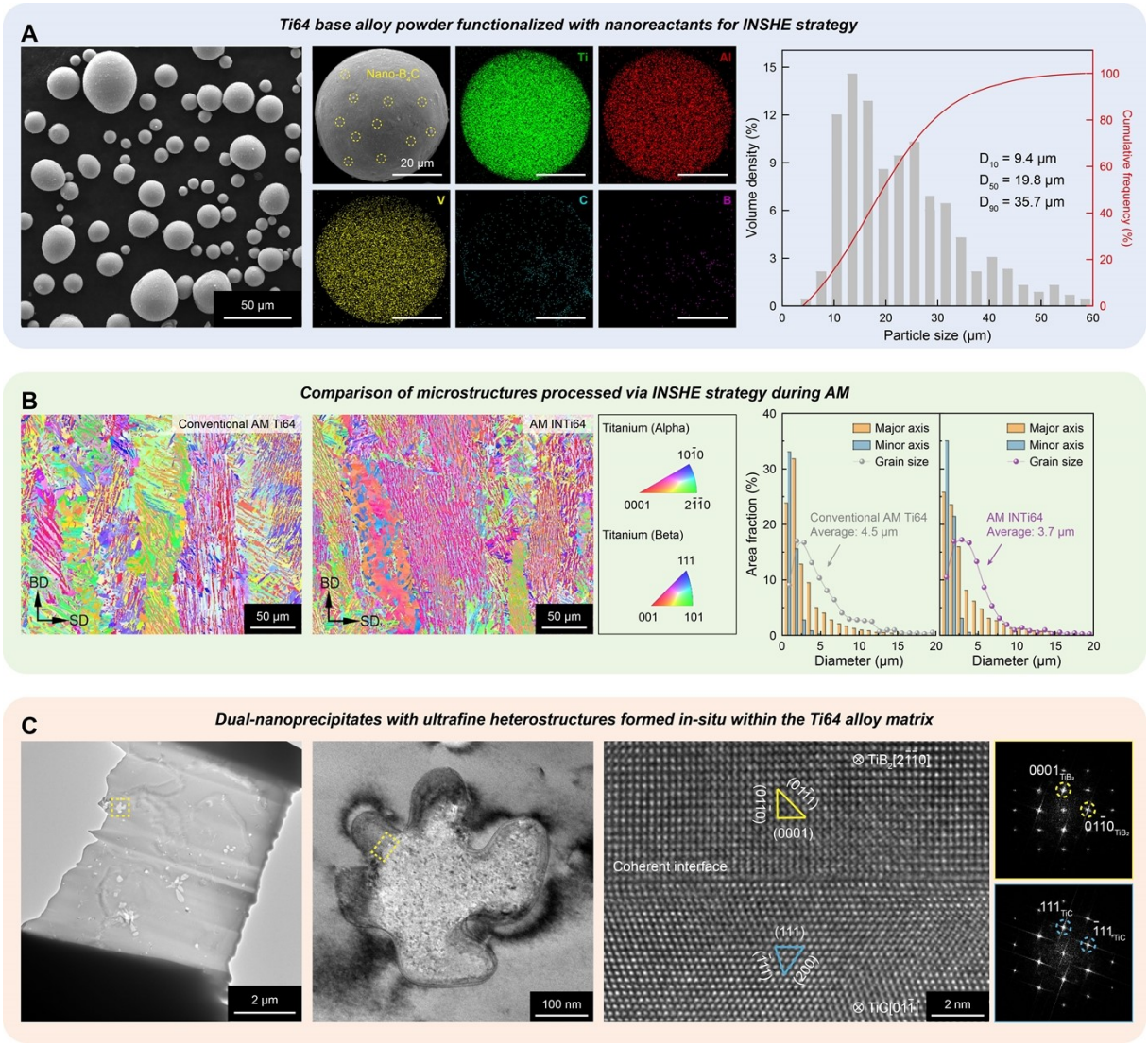

Figure S47. Preliminary demonstration of Ti-6Al-4V (Ti64) alloy processed via INSHE strategy during AM. (**A**) SEM images of Ti64 base alloy powder functionalized with B_4C nanoreactants, together with the corresponding elemental EDS mapping and particle size distribution curve. (**B**) Comparative EBSD IPF maps showing the microstructures of conventionally fabricated AM Ti64 alloy and that processed via the proposed INSHE strategy (AM INTi64), along with statistical analyses based on major axis, minor axis, and grain size distribution. BD and SD denote the build direction and scan direction, respectively. (**C**) TEM characterization of the designed dual-nanoprecipitates formed in-situ within the Ti64 alloy matrix, where HRTEM image and the corresponding FFT patterns confirm the coherent interface and orientation relationship of the ultrafine heterostructures.

Table S1. Theoretical reference values of standard enthalpy change ($\Delta_f H0\ 298$), standard entropy change ($\Delta_f S0\ 298$), and standard Gibbs free energy change ($\Delta_f G0\ 298$) for different substances.

Substances	$\Delta_f H0\ 298$ ($kJ \cdot mol^{-1}$)	$\Delta_f S0\ 298$ ($J \cdot K^{-1} \cdot mol^{-1}$)	$\Delta_f G0\ 298$ ($J \cdot mol^{-1}$)	Ref.
Ni	--	29.874	$-29.874 \cdot T$	S28
Ti	--	30.759	$-30.759 \cdot T$	S28
C	--	5.740	$-5.740 \cdot T$	S28
B	--	5.834	$-5.834 \cdot T$	S28
B_4C	-62.676	27.175	$-62{,}676 - 27.175 \cdot T$	S28
TiC	-184.096	24.229	$-184{,}096 - 24.229 \cdot T$	S28
TiB	-160.247	34.727	$-160{,}247 - 34.727 \cdot T$	S29
TiB_2	-279.491	28.485	$-279{,}491 - 28.485 \cdot T$	S29
Ni_3C	37.656	106.274	$37{,}656 - 106.274 \cdot T$	S29
NiTi	-66.526	53.137	$-66{,}526 - 53.137 \cdot T$	S29
NiB	-100.416	30.125	$-100{,}416 - 30.125 \cdot T$	S29
Ni_4B_3	-311.708	114.642	$-311{,}708 - 114.642 \cdot T$	S29

Table S2. Theoretically calculated values of standard enthalpy change ($\Delta_f H0$ 298), standard entropy change ($\Delta_f S0$ 298), and standard Gibbs free energy change ($\Delta_f G0$ 298) for different reaction systems.

Reaction systems	$\Delta_f H0$ 298 (kJ·mol^{-1})	$\Delta_f S0$ 298 (J·K^{-1}·mol^{-1})	$\Delta_f G0$ 298 (J·mol^{-1})
TiC → Ti + C	184.096	12.270	184,096 - 12.270·T
NiTi → Ni + Ti	66.526	7.496	66,526 - 7.496·T
TiB_2 → TiB + B	119.244	12.076	119,244 - 12.076·T
B_4C → 4B + C	62.676	1.901	62,676 - 1.901·T
3Ni + C → Ni_3C	37.656	10.912	37,656 - 10.912·T
Ti + TiB_2 → 2TiB	-41.003	-10.210	-41,003 + 10.210·T
2TiB + C → TiB_2 + TiC	-143.093	-22.480	-143,093 + 22.480·T
Ni + B → NiB	-100.416	-5.583	-100,416 + 5.583·T
Ti + C → TiC	-184.096	-12.270	-184,096 + 12.270·T
Ti + B → TiB	-160.247	-1.866	-160,247 + 1.866·T
Ti + 2B → TiB_2	-279.491	-13.942	-279,491 + 13.942·T
4Ni + 3B → Ni_4B_3	-311.708	-22.356	-311,708 + 22.356·T
3Ti + B_4C → 2TiB_2 + TiC	-743.078	-38.258	-743,078 + 38.258·T
5Ti + B_4C → 4TiB + TiC	-762.408	-17.833	-762,408 + 17.833·T

Table S3. Phase transformation temperatures (TTs) and enthalpies (latent heat) determined from the DSC thermograms for the powder samples and as-printed samples.

Samples classification	Reverse transformation				Forward transformation			
	A_s (K)	A_p (K)	A_f (K)	$\Delta H_{M\rightarrow A}$ (J/g)	M_s (K)	M_p (K)	M_f (K)	$\Delta H_{A\rightarrow M}$ (J/g)
SMA (powder)	266.3	292.9	305.1	12.3	283.9	259.1	216.4	-13.6
INSMA (powder)	242.1	284.1	303.5	11.4	285.8	256.9	223.3	-9.3
SMA (as-printed)	313.5	357.1	367.9	19.1	341.4	315.6	282.1	-18.7
INSMA (as-printed)	239.4	274.9	306.0	8.1	293.3	231.4	214.2	-7.2

Table S4. The ICP-OES chemical composition of as-received (AR) SMA micropowder.

Elements	Weight ratio (wt. %)	Normalized atomic ratio (at. %)
Ni	55.76	50.79
Ti	44.15	49.21
Fe	0.01	--
C	0.01	--
O	0.06	--
N	0.01	--

Table S5. The flowability indicators of AR SMA micropowder.

Apparent density, AD_H ($g \cdot cm^{-3}$)	Tap density, TD ($g \cdot cm^{-3}$)	Hausner ratio, HR	Flow rate, FR_H [$s \cdot (50\ g)^{-1}$]	Specific surface area, BET ($m^2 \cdot kg^{-1}$)
3.85	4.20	1.09	21.30	70.05

Table S6. The crystallographic information used for the EBSD and TKD analysis.

Phase	Space group	Crystal structure	Lattice parameter	Ref.
B2 austenite	$Pm\bar{3}m$ (221)	BCC	$a = b = c = 2.99$ Å $\alpha = \beta = \gamma = 90°$	S30
B19' martensite	$P2_1/m$ (11)	Monoclinic	$a = 2.89$ Å $b = 3.97$ Å $c = 4.83$ Å $\alpha = 90°$ $\beta = 105.23°$ $\gamma = 90°$	S30
TiC	$Pm\bar{3}m$ (225)	FCC	$a = b = c = 4.33$ Å $\alpha = \beta = \gamma = 90°$	S31
TiB_2	$P6/mmm$ (191)	Hexagonal	$a = 3.03$ Å $b = 3.03$ Å $c = 3.23$ Å $\alpha = 90°$ $\beta = 90°$ $\gamma = 120°$	S32

Table S7. Summary of detailed testing parameters and structural information of the comparative micro-/nanolattices shown in the Ashby plot of Fig. 4F, including strain rate, number of loading cycles, and topology of each structure, as reported in the corresponding references.

Comparative material	Loading protocol		Topological architecture				Reference
	Strain rate	Number of cycles	Unit cell topology	Unit cell size	Whole lattice size	Designed porosity	
INSMA	1×10^{-3} s^{-1}	1 and 10	Dode	2 mm×2 mm×2 mm	10 mm×10 mm×10 mm	75%	This work
CuCrNb	1×10^{-3} s^{-1}	1	BCC Gyroid Octet	2 mm×2 mm×2 mm	10 mm×10 mm×10 mm	78% 77% 80%	Wang *et al.*, *Scr. Mater.*, **239**, 115801, 2024
CuCrZr	3.33×10^{-3} s^{-1}	1	Diamond	① 2.5 mm×2.5 mm×2.5 mm ② 2 mm×2 mm×2 mm ③ 1.7 mm×1.7 mm×1.7 mm	10 mm×10 mm×10 mm	① 80% ② 85% ③ 90%	Ma *et al.*, *Mater. Des.*, **187**, 108406, 2020
Ti-6Al-4V	2×10^{-3} s^{-1}	10	Diamond Cuboctahedron SC	1.5 mm×1.5 mm×1.5 mm	Cylinder: Height of 15 mm, diameter of 10 mm.	60%,70%,80%,90% 65%,70%,80%,85% 60%,70%,80%,90%	Yavari *et al.*, *J. Mech. Behav. Biomed. Mater.*, **43**, 91-100, 2015
Ti-6Al-4V	2×10^{-3} s^{-1}	1	① SC ② Diamond ③ Truncated cube ④ Truncated cuboctahedron ⑤ Rhombic dodecahedron ⑥ Rhombicuboctahedron	1.5 mm×1.5 mm×1.5 mm	Cylinder: Height of 15 mm, diameter of 10 mm.	① 90% ② 80% ③ 75% ④ 70% ⑤ 65% ⑥ 65%	Ahmadi *et al.*, *Materials*, **8**, 1871-1896, 2015
β-type Ti-24Nb-4Zr-8Sn (Ti2448)	1.67×10^{-4} s^{-1}	6	SC Topology optimized Rhombic dodecahedron	3.33 mm×3.33 mm×3.33 mm	10 mm×10 mm×10 mm	80%	Liu *et al.*, *Scr. Mater.*, **153**, 99-103, 2018
AlSi10Mg	8.33×10^{-4}	1 and 7	BCC	2 mm×2	10 mm×10	80%	Lei *et al.*, *Mater.*

	s^{-1}			mm×2 mm	mm×10 mm		*Des.*, **169**, 107685, 2019
AlSi10Mg	2.2×10^{-3} s^{-1}	1	BCC	~4.2 mm×4.2 mm×4.2 mm	Cylinder: Height of 30 mm, diameter of 30 mm.	80%	Suzuki *et al.*, *Adv. Eng. Mater.*, **21**, 1900571, 2019
Al-12Si	1.67×10^{-3} s^{-1}	1	BCC F2BCC	5 mm×5 mm×5 mm	30 mm×30 mm×30 mm	81.5%	Al-Saedi *et al.*, *Mater. Des.*, **144**, 32-44, 2018
Maraging steel	1×10^{-3} s^{-1}	1	IWP Gyroid Diamond Primitive	7 mm×7 mm×7 mm	42 mm×42 mm×42 mm	80% 85% 90% /	Al-Ketan *et al.*, *Addit. Manuf.*, **19**, 167-183, 2018
AISI 4130 grade steel	1×10^{-3} s^{-1}	1	FCC Fluorite FCC+SC	4 mm×4 mm×4 mm	20 mm×20 mm×20 mm	70% 70% 70%,75%,80%,85%,90%	Li *et al.*, *Small*, **17**, 2100336, 2021 Li *et al.*, *Mater. Des.*, **178**, 107881, 2019
316L	1.67×10^{-2} s^{-1}	6	SC BCC FCC	6 mm×6 mm×6 mm	30 mm×30 mm×30 mm	85% 75% 65%	Bonatti *et al.*, *Acta Mater.*, **164**, 301-321, 2019
316L	2×10^{-2} s^{-1}	1	FCC: TPMS-like FCC: Octet-truss FCC: Iso-shell	6 mm×6 mm×6 mm	30 mm×30 mm×30 mm	70%	Bonatti *et al.*, *J. Mech. Phys. Solids*, **122**, 1-26, 2019
SiOC	4.17×10^{-3} s^{-1}	1	BCC Honeycomb Pyramidal	Cylinder: 5.1 µm (length)×0.5 µm (diameter) 9.8 µm×0.5 µm 3.6 µm×1.0 µm	4 mm×4 mm×2 mm	63%-78% 70% 90%	Eckel *et al.*, *Science*, **351**, 58-62, 2016
SiC foam Duocel	4.17×10^{-3} s^{-1}	1	Amorphous	/	4 mm×4 mm×2 mm	75%	
AlSiO ceramic foam	4.17×10^{-3}	1	Amorphous	/	4 mm×4	60%	

	s^{-1}				mm×2 mm		
Ni-B hollows	5×10^{-3} s^{-1}	1	SC BCC FCC Hexagonal Honeycomb	10 μm×10 μm×10 μm	40 μm×40 μm×40 μm	93% 90% 88% 85% 66%	Mieszala *et al.*, *Small*, **13**, 1602514, 2017
Ni-P hollows	1×10^{-2} s^{-1}	6	Octahedral	500 μm×500 μm×500 μm	4 mm×4 mm×1 mm	99.31%-99.99%	Schaedler *et al.*, *Science*, **334**, 962-965, 2011
Au hollows	1×10^{-4} s^{-1}	1	Octahedral	5-20 μm	75 μm×75 μm×75 μm	95%	Montemayor *et al.*, *J. Appl. Mech.*, **82**, 071012, 2015
Oxide ceramics Composite ceramics	2.5×10^{-3} s^{-1} 5×10^{-4} s^{-1}	20	Bow-tie	8 μm×8 μm×8 μm	60 μm×60 μm×40 μm	75%	Deng *et al.*, *Mater. Today*, **21**, 467-474, 2018
Polymeric microlattices Pyrolytic carbon nanolattices	1×10^{-3} s^{-1}	1	Schwarz P I-WP Neovius	300 μm×300 μm×300 μm 6 μm×6 μm×6 μm 1 μm×1 μm×1 μm	1.5 mm×1.5 mm×1.5 mm 30 μm×30 μm×30 μm 5 μm×5 μm×5 μm	60%,70%,80%,90%,95%	Wang *et al.*, *Proc. Natl. Acad. Sci.*, **119**, e2119536119, 2022
Glassy carbon	2×10^{-2} s^{-1}	1	Tetrahedral	Unit cell edge length: 2.02 μm 1.44 μm 970 nm	Honeycomb: Edge length of 5 μm, height of 5 μm.	75%-87%	Schroer *et al.*, *Nat. Mater.*, **15**, 438-443, 2016
$Zr_{54}Ni_{28}Al_{18}$ MEA composite nanolattices	1×10^{-3} s^{-1}	1	Octahedral	7 μm×7 μm×7 μm	~32 μm×32 μm×36 μm	96%-99.6%	Liontas *et al.*, *Acta Mater.*, **133**, 393-407, 2017
$Al_{19.5}Cr_{19.9}Fe_{15.1}Co_{23.7}Ni_{21.9}$ HEA composite nanolattices	1×10^{-3} s^{-1}	6	Octet-truss	8-15 μm	100 μm×100 μm×100 μm	77%	Zhang *et al.*, *Nano Lett.*, **18**, 4247-4256, 2018
$CoCrNiFeAl_{0.3}$ HEA composite nanolattices	1×10^{-3} s^{-1}	1 and 3	BCC	2.5 μm×2.5 μm×1.25 μm	20 μm×20 μm×10 μm	80%	Gao *et al.*, *Adv. Eng. Mater.*, **20**, 1700625, 2018

Note: SC, simple cubic; BCC, body-centered cubic; FCC, face-centered cubic; F2BCC, two face-centered cubic combined in a BCC way; Iso, isotropic; TPMS,

triply periodic minimal surface; I-WP, Schoen’s I-graph–wrapped package.

Table S8. Fitting results of polarization curves for as-built pristine SMA and INSMA samples in 3.5 wt.% NaCl solution. I_{corr}, corrosion current density; R_p, polarization resistance; E_{corr}, corrosion potential; E_b, breakdown potential.

Samples classification	I_{corr} (μA·cm^{-2})	R_p (Ω·cm^2)	E_{corr} (mV)	E_b (mV)	/
INSMA	2.509	2.998×10^4	-1374.85	-885.13	Average
	0.822	2.849×10^3	21.67	10.02	Std-Dev
Pristine SMA	4.679	1.986×10^4	-1445.79	-922.54	Average
	1.115	2.951×10^3	10.65	25.23	Std-Dev

Table S9. Fitting results of EIS measurements for as-built pristine SMA and INSMA samples in 3.5 wt.% NaCl solution. R_s, solution resistance; R_f, film resistance on the surface; CPE_1, film capacitance; R_{ct}, charge transfer resistance; CPE_2, double layer capacitance.

Samples classification	R_s ($\Omega \cdot cm^2$)	R_f ($k\Omega \cdot cm^2$)	CPE_1 ($F \cdot cm^{-2}$)	n_1	R_{ct} ($k\Omega \cdot cm^2$)	CPE_2 ($F \cdot cm^{-2}$)	n_2	/
INSMA	8.75	65.54	6.67×10^{-6}	0.87	475.56	1.07×10^{-5}	0.96	Average
	0.25	3.72	7.90×10^{-8}	0.01	17.50	3.55×10^{-7}	0.02	Std-Dev
Pristine SMA	2.96	51.58	7.48×10^{-6}	0.95	248.55	2.89×10^{-5}	0.77	Average
	0.32	1.59	2.33×10^{-7}	0.01	20.64	1.05×10^{-6}	0.02	Std-Dev

Table S10. Statistical summary of the key mechanical and functional properties of pristine SMA and INSMA samples. The table lists the mean values and standard deviations for hardness, yield strength, compressive strength, energy absorption per unit volume, damping capacity, shape recovery rate, and other related metrics, derived from multiple independent tests ($n \geq 3$, and up to 10 in selected cases). These results confirm the reproducibility of the measured properties and provide a robust statistical basis for comparison.

Property	Pristine SMA	INSMA	Note
Hardness, H (GPa)	2.43 ± 0.19	4.94 ± 0.33	Nanoindentation
Reduced Young's modulus, E_r (GPa)	62.79 ± 2.38	75.06 ± 2.53	Nanoindentation
H/E_r ratio (%)	3.9 ± 0.8	6.5 ± 0.2	Nanoindentation
Wear rate, W (10^{-4} $mm^3 \cdot N^{-1} \cdot m^{-1}$)	5.46 ± 0.34	4.33 ± 0.22	/
Compressive strength, σ_{max} (GPa)	2.6 ± 0.2	4.1 ± 0.3	Micropillar
Critical stress†, σ_s (GPa)	0.96 ± 0.24	2.15 ± 0.45	Micropillar
Critical strain†, ε_s (-)	0.06 ± 0.02	0.12 ± 0.04	Micropillar
Ultimate tensile strength, σ_{UTS}, (MPa)	545.2 ± 31.6	629.6 ± 37.5	Bulk
Yield strength‡, σ_{YS}, (MPa)	183.7 ± 15.9	250.8 ± 13.3	Bulk
Elongation-to-failure, ε (%)	8.3 ± 0.5	8.6 ± 0.6	Bulk
Ultimate compressive strength, σ_{UCS}, (MPa)	2197.2 ± 167.1	2893.5 ± 175.4	Millipillar
Compressive fracture strain, ε' (%)	37.7 ± 1.8	40.4 ± 1.2	Millipillar
Compressive strength, σ_{max} (GPa)	67.3 ± 8.9	102.5 ± 9.3	Microlattice
Energy absorption per unit volume, u ($J \cdot m^{-3}$)	2.71×10^7 ± 2.67×10^6	6.73×10^7 ± 2.82×10^6	Microlattice
Damping capacity, tan δ (10^{-3})	6.2 ± 0.4	7.6 ± 0.2	Stress-relaxation mode
Damping capacity, tan δ (10^{-3})	33.3 ± 5.4	97.4 ± 8.5	Strain-sweep mode
Shape recovery rate, R_r (%)	87.5 ± 0.6	99.6 ± 0.3	Shape-memory mode

Note: †The critical stress and strain are defined as the stress and strain values corresponding to the onset of pronounced slip during the initial strain burst. ‡The yield strength refers to the stress required to initiate the martensitic transformation.

Movie S1. In-situ micropillar compression test of plastic stress-strain response of the INSMA sample.

Movie S2. In-situ micropillar compression test of plastic stress-strain response of the pristine SMA sample.

Movie S3. In-situ micropillar compression test of critical stress-strain response related to slip banding of the INSMA sample.

Movie S4. In-situ micropillar compression test of critical stress-strain response related to slip banding of the pristine SMA sample.

Movie S5. In-situ micropillar compression test of cyclic stress-strain response of the INSMA sample subjected to a stress of 450 MPa with a frequency of 5 Hz.

Movie S6. Micro-CT 3D reconstruction and visualization of internal quality for SMMM samples.

Supplementary References

S1. J. Liu, H. Yu, P. Karamched, J. Hu, G. He, D. Goran, G. M. Hughes, A. J. Wilkinson, S. L.-Perez, C. R.M. Grovenor, Mechanism of the α-Zr to hexagonal-ZrO transformation and its impact on the corrosion performance of nuclear Zr alloys. *Acta Mater.* **179**, 328-341 (2019). doi:10.1016/j.actamat.2019.08.051

S2. J. Liu, S. Lozano-Perez, A. J. Wilkinson, C. R. M. Grovenor, On the depth resolution of transmission Kikuchi diffraction (TKD) analysis. *Ultramicroscopy* **205**, 5-12 (2019). doi:10.1016/j.ultramic.2019.06.003

S3. P. Hua, M. Xia, Y. Onuki, Q. Sun, Nanocomposite NiTi shape memory alloy with high strength and fatigue resistance. *Nat. Nanotechnol.* **16**, 409-413 (2021). doi:10.1038/s41565-020-00837-5

S4. C. Dan, Y. Cui, Y. Wu, *et al.*, Achieving ultrahigh fatigue resistance in AlSi10Mg alloy by additive manufacturing. *Nat. Mater.* **22**, 1182-1188 (2023). doi:10.1038/s41563-023-01651-9

S5. P. Sudharshan Phani, W. C. Oliver, A critical assessment of the effect of indentation spacing on the measurement of hardness and modulus using instrumented indentation testing. *Mater. Des.* **164**, 107563 (2019). doi:10.1016/j.matdes.2018.107563

S6. T.-C. Lin, C. Cao, M. Sokoluk, L. Jiang, X. Wang, J. M. Schoenung, E. J. Lavernia, X. Li, Aluminum with dispersed nanoparticles by laser additive manufacturing. *Nat. Commun.* **10**, 4124 (2019). doi:10.1038/s41467-019-12047-2

S7. M. Thomas, G. J. Baxter, I. Todd, Normalised model-based processing diagrams for additive layer manufacture of engineering alloys. *Acta Mater.* **108**, 26-35 (2016). doi:10.1016/j.actamat.2016.02.025

S8. J. Ren, Y. Zhang, D. Zhao, Y. Chen, S. Guan, Y. Liu, L. Liu, S. Peng, F. Kong, J. D. Poplawsky, G. Gao, T. Voisin, K. An, Y. M. Wang, K. Y. Xie, T. Zhu, W. Chen, Strong yet ductile nanolamellar high-entropy alloys by additive manufacturing. *Nature* **608**, 62-68 (2022). doi:10.1038/s41586-022-04914-8

S9. G. Li, Y. Huang, X. Li, C. Guo, Q. Zhu, J. Lu, Laser powder bed fusion of nano-titania modified 2219 aluminium alloy with superior mechanical properties at both room and elevated temperatures: The significant impact of solute. *Addit. Manuf.* **60**, 103296 (2022). doi:10.1016/j.addma.2022.103296

S10. X. P. Li, G. Ji, Z. Chen, A. Addad, Y. Wu, H.W. Wang, J. Vleugels, J. Van Humbeeck, J.P. Kruth, Selective laser melting of nano-TiB_2 decorated AlSi10Mg alloy with high fracture strength and ductility. *Acta Mater.* **129**, 183-193 (2017). doi:10.1016/j.actamat.2017.02.062

S11. A. C. Fischer-Cripps, D. W. Nicholson, Nanoindentation. Mechanical engineering series. *Appl. Mech. Rev.* **57**, B12-B12 (2004). doi:10.1115/1.1704625

S12. Y. Nagaoka, M. Suda, I. Yoon, N. Chen, H. Yang, Y. Liu, B. A. Anzures, S. W. Parman, Z. Wang, M. Grünwald, H. M. Yamamoto, O. Chen, Bulk Grain-Boundary Materials from Nanocrystals. *Chem* **7**, 509-525 (2021). doi:10.1016/j.chempr.2020.12.026

S13. B. N. Sahoo, S. K. Panigrahi, Synthesis, characterization and mechanical properties of in-situ (TiC-TiB_2) reinforced magnesium matrix composite. *Mater. Des.* **109**, 300-313 (2016). doi:10.1016/j.matdes.2016.07.024

S14. X. Wang, S. Li, Y. Han, G. Huang, J. Mao, W. Lu, Roles of reinforcements in twin nucleation and nano-α precipitation in the hybrid TiB/TiC-reinforced titanium matrix composites during high-temperature fatigue. *Scr. Mater.* **196**, 113758 (2021). doi:10.1016/j.scriptamat.2021.113758

S15. L. Liu, S. Li, D. Peng, D. Hui, X. Zhang, B. Li, T. Liang, P. Shi, A. Bahador, J. Umeda, K. Kondoh, S. Li, L. Gao, Z. Wang, G. Li, S. Zhang, R. Wang, W. Chen, Loss-free tensile ductility of dual-structure titanium composites via an interdiffusion and self-organization strategy. *Proc. Natl. Acad. Sci. U.S.A.* **120**, e2302234120 (2023). doi:10.1073/pnas.2302234120

S16. S. Wei, L. Huang, X. Li, Y. Jiao, W. Ren, L. Geng, Network-Strengthened Ti-6Al-4V/(TiC+TiB) Composites: Powder Metallurgy Processing and Enhanced Tensile Properties at Elevated Temperatures. *Metall. Mater. Trans. A* **50**, 3629-3645 (2019). doi:10.1007/s11661-019-05244-7

S17. S. Li, H. Hassanin, M.M. Attallah, N.J.E. Adkins, K. Essa, The development of TiNi-based negative Poisson's ratio structure using selective laser melting. *Acta Mater* **105**, 75-83 (2016). doi:10.1016/j.actamat.2015.12.017.

S18. C. Tan, J. Zou, S. Li, P. Jamshidi, A. Abena, A. Forsey, R.J. Moat, K. Essa, M. Wang, K. Zhou, M.M. Attallah, Additive manufacturing of bio-inspired multi-scale hierarchically strengthened lattice structures. *Int. J. Mach. Tool Manufact.* **167**, 103764 (2021). doi:10.1016/j.ijmachtools.2021.103764.

S19. R. Xi, H. Jiang, G. Li, S. Kustov, Z. Zhang, H. Wei, Z. Liu, G. Zhao, J.V. Humbeeck, X. Wang, In-situ alloying of NiTiNb ternary shape memory alloys via laser powder bed fusion using pre-alloyed NiTi and elemental Nb powders: Microstructure, phase transformation behavior and functional properties. *Addit. Manuf.* **79**, 103933 (2024). doi:10.1016/j.addma.2023.103933

S20. C. Ma, Q. Ge, L. Yuan, D. Gu, D. Dai, R. Setchi, M. Wu, Y. Liu, D. Li, S. Ma, X. Peng, Z. Fang, The development of laser powder bed fused nano-TiC/NiTi superelastic composites with hierarchically heterogeneous microstructure and considerable tensile recoverable strain. *Compos. Part B Eng.* **250**, 110457 (2023). doi:10.1016/j.compositesb.2022.110457

S21. J. Yi, L. Wan, T. Shu, X. Zhang, F. Liu, G. J. Cheng, Unleashing multi-scale mechanical enhancement in NiTi shape memory alloy via annular intra-laser deposition with homogenized Ti_2Ni nanoprecipitates. *Acta Mater.* **262**, 119418 (2024). doi:10.1016/j.actamat.2023.119418

S22. R.N. Wenzel, Resistance of solid surfaces to wetting by water. *Ind. Eng. Chem.* **28**, 988-994 (1936). doi:10.1021/ie50320a024

S23. A. Samanta, Q. Wang, S.K. Shaw, H. Ding, Roles of chemistry modification for laser textured metal alloys to achieve extreme surface wetting behaviors. *Mater. Des.* **192**, 108744 (2020). doi:10.1016/j.matdes.2020.108744

S24. F. Xiao, T. Fukuda, X. Jin, J. Liu, T. Kakeshita, Elastocaloric effect associated with different types of martensitic transformations: typical first-order and weak first-order ones. *Phys. Status Solidi B* **255**, 1700246 (2018). doi:10.1002/pssb.201700246

S25. C. Li, Q. Pan, Y. Shi, *et al.*, Influence of aging temperature on corrosion behavior of Al-Zn-Mg-Sc-Zr alloy. *Mater. Des.* **55**, 551-559 (2014). doi:10.1016/j.matdes.2013.10.018

S26. R.I. Revilla, B. Wouters, F. Andreatta, *et al.*, EIS comparative study and critical Equivalent Electrical Circuit (EEC) analysis of the native oxide layer of additive manufactured and wrought 316L stainless steel. *Corros. Sci.* **167**, 108480 (2020). doi:10.1016/j.corsci.2020.108480

S27. B. Hirschorn, M.E. Orazem, B. Tribollet, *et al.*, Determination of effective capacitance and film thickness from constant-phase-element parameters. *Electrochim. Acta* **55**, 6218-6227 (2010). doi:10.1016/j.electacta.2009.10.065

S28. I. Barin, G. Platzki, *Thermochemical data of pure substances* (Wiley Online Library, 1989).

doi:10.1002/9783527619825

S29. D. Ye, *Thermodynamics date handbook of practical inorganic matter* (Metallurgical Industry Press Beijing, 1981).

S30. K. Otsuka, X. Ren, Physical metallurgy of Ti–Ni-based shape memory alloys. *Prog. Mater Sci.* **50**, 511-678 (2005). doi:10.1016/j.pmatsci.2004.10.001

S31. M. Sokoluk, C. Cao, S. Pan, X. Li, Nanoparticle-enabled phase control for arc welding of unweldable aluminum alloy 7075. *Nat. Commun.* **10**, 98 (2019). doi:10.1038/s41467-018-07989-y

S32. Y. Ma, A. Ahmed, G. Ji, M. Zhang, L. Williams, Z. Chen, V. Ji, Atomic-scale investigation of the interface precipitation in a TiB2 nanoparticles reinforced Al–Zn–Mg–Cu matrix composite. *Acta Mater.* **185**, 287-299 (2020). doi:10.1016/j.actamat.2019.11.068